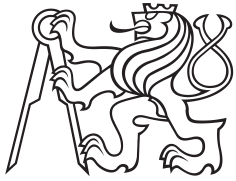


Master Thesis



Czech
Technical
University
in Prague

F3

Faculty of Electrical Engineering
Department of Control Engineering

Vehicle active suspension control system

Jiří Minarik

Supervisor: Ing. Petr Liškař

Supervisor–specialist: doc. Ing. Tomáš Haniš, Ph.D.

Field of study: Cybernetics and Robotics

Subfield: Systems and Control

January 2022

I. Personal and study details

Student's name: **Minarik Jiří** Personal ID number: **466174**
Faculty / Institute: **Faculty of Electrical Engineering**
Department / Institute: **Department of Control Engineering**
Study program: **Cybernetics and Robotics**
Branch of study: **Systems and Control**

II. Master's thesis details

Master's thesis title in English:

Vehicle active suspension control system

Master's thesis title in Czech:

Řídicí systém pro aktivní podvozek vozidla

Guidelines:

The aim of the thesis is to develop an active camber mechatronic system that enhancing safety as well as performance of a vehicle. The active camber system shall be suitable for real environments and practical application. The thesis will address following points:

- 1) Analyze camber kinematics and its influence on vehicle dynamics
- 2) Analyze mechatronic system of camber actuation
- 3) Develop chassis control algorithm for camber active system to enhance performance of a vehicle
- 4) Validate developed algorithms

Bibliography / sources:

- [1] Dieter Schramm, Manfred Hiller, Roberto Bardini – Vehicle Dynamics – Duisburg 2014
- [2] Hans B. Pacejka - Tire and Vehicle Dynamics – The Netherlands 2012
- [3] Shad M. Laws - An Active Camber Concept for Extreme Maneuverability: Mechatronic Suspension Design, Tire Modeling, and Prototype Development – USA, California: Stanford, 2010
- [4] Daan Roethof - Influence of Active Camber Control on Steering Feel – Netherlands: Delft, 2016
- [5] Ankith Suresh Athrey - Design and Analysis of an Electric Over-Actuated Vehicle Suspension, Sweden, Stockholm: KTH, 2020
- [6] Shiruo Li - Camber effect study on combined tire forces, Sweden, Stockholm: KTH, 2013

Name and workplace of master's thesis supervisor:

Ing. Petr Liškář, Department of Automotive, Combustion Engine and Railway Engineering, FME

Name and workplace of second master's thesis supervisor or consultant:

doc. Ing. Tomáš Haniš, Ph.D., Department of Control Engineering, FEE

Date of master's thesis assignment: **10.09.2021** Deadline for master's thesis submission: **04.01.2022**

Assignment valid until:

by the end of winter semester 2022/2023

Ing. Petr Liškář
Supervisor's signature

prof. Ing. Michael Šebek, DrSc.
Head of department's signature

prof. Mgr. Petr Páta, Ph.D.
Dean's signature

III. Assignment receipt

The student acknowledges that the master's thesis is an individual work. The student must produce his thesis without the assistance of others, with the exception of provided consultations. Within the master's thesis, the author must state the names of consultants and include a list of references.

Date of assignment receipt

Student's signature

Acknowledgements

I would like to thank my supervisor, Ing. Petr Liškař, and Ing. Tomáš Haniš, Ph.D. I am incredibly thankful for sharing their expertise, and valuable guidance extended to me. I am sincerely grateful for the opportunity to work on such complex project.

I also thank my mother for the words of encouragement, support, and attention and to everybody who directly or indirectly, have lent me their help.

Declaration

I hereby declare that I have completed this thesis with the topic "Vehicle active suspension control system" independently and that I have included a full list of used references. I have no objection to the usage of this work in compliance with the act 60 Zákon č. 121/2000 Sb. (copyright law).

In Prague, 1. January 2022

Abstract

Safety systems like ESP and ABS are limited by the saturation of the forces in the contact patch. The Active Camber Control can actively change the saturation and thus provide higher safety and performance rankings. This thesis provides a comprehensive study of the requirements of such a camber actuator. Furthermore, a framework that uses commercially available measurement devices is established and used to develop suspension and vehicle dynamics controllers that operate without driver intervention. The result is a vehicle with higher maximal lateral acceleration, cornering stability and efficiency, and disturbance rejection that holds across the whole range of the different load variations, CG locations, and other boundary conditions defined in this thesis.

Keywords: Active Camber Control, active safety, robustness, boundary conditions, over-actuation, LQR, camber actuator, model matching, single track, twin track, suspension, McPherson, double wishbone

Supervisor: Ing. Petr Liškař
TP2 s.r.o.,
Pelzova 1514,
Praha 5, 156 00

Abstrakt

Bezpečnostní systémy jako ESP a ABS jsou omezeny saturací sil v kontaktní ploše pneumatik. Active Camber Control může aktivně měnit saturaci a tím poskytovat vyšší hodnocení v bezpečnosti a výkonu auta. Tato práce poskytuje komplexní studii požadavků na takový camber aktuátor. Kromě toho je vytvořen rámec, který využívá komerčně dostupná měřicí zařízení a je využit k odvození regulátorů nápravy a dynamiky vozidla, které fungují bez zásahu řidiče. Výsledkem je vozidlo s vyšším maximálním příčným zrychlením, stabilitou a účinností v zatáčkách a potlačení rušení, které platí v celém rozsahu různých variací zatížení, umístění těžiště a dalších okrajových podmínek definovaných v této práci.

Klíčová slova: Aktivní řízení odklonu kola, aktivní bezpečnost, robustnost, okrajové podmínky, přebuzení auta, LQR, aktuátor odklonu kola, přizpůsobení modelu, jednostopý model, dvoustopý model, náprava, MacPherson, lichoběžníková náprava

Překlad názvu: Řídící systém pro aktivní podvozek auta

Contents

1	Introduction	1
1.1	Motivation	1
1.2	Suspension types	2
1.2.1	Double wishbone	2
1.2.2	McPherson	2
1.3	Suspension terms	4
1.3.1	Steering axis	4
1.3.2	KPI and scrub radius	4
1.3.3	Camber angle	5
1.3.4	Caster angle	5
1.4	State-of-the-art	6
1.5	Toolboxes	11
1.5.1	Simscape model of suspension	11
1.5.2	Twin track	12
1.5.3	Single track mathematical model	14
2	Problem definition	19
2.1	Camber definition	19
2.2	Camber development	20
2.2.1	Camber due to body roll	21
2.2.2	Camber due to KPI	21
2.2.3	Camber due to Caster	21
2.3	Brush Model - Contact patch development	23
2.4	Camber in Pacejka	26
2.5	Friction circle development with camber	30
2.6	Linearization of Pacejka Magic Formula	32
2.6.1	Linearization of slip angle	32
2.6.2	Linearization of camber angle	33
2.7	Camber benefits	34
2.7.1	Cornering losses	34
2.7.2	Camber for faster lateral force generation	35
2.7.3	Line Of Peaks problem	36
2.7.4	Usage diversity of camber angle	37
2.8	Active Camber Control system design	38
2.8.1	Controlled variables	39
2.8.2	Measured variables	39
2.8.3	Parameters and control requirements	40
2.9	Active camber actuation point	43
2.10	Actuator requirements	44
2.10.1	Body roll due to road bumps	44
2.10.2	Body pitch due to road bumps	45
2.10.3	Longitudinal and Lateral force development	45
2.10.4	Slew rate identification	46
2.11	Approach to the problem solution	48
3	Mechatronic system control implementation	49
3.1	Camber actuation	49
3.1.1	Actuator range	50
3.1.2	Actuator response time	53
3.1.3	Acting forces	54
3.1.4	Minimization of static force	58
3.1.5	Resultant actuator specifications	59
3.2	Low-level controller	61
3.2.1	McPherson geometry model	61
3.2.2	Forward kinematics	62
3.2.3	Control law: nonlinear mapping	63
3.2.4	Roll estimation	65
3.2.5	Unknown θ angle	72
3.3	Compensation of the KPI and caster influence on camber	77
4	Active Camber Control	79
4.1	Design	79
4.2	Reference signals	80
4.2.1	Handling limits for the vehicle	83

4.2.2 Handling characteristic of the vehicle	83	E Derivation of the KPI and caster influence on camber angle	137
4.3 Controller structure	86	F Velocity dependent LQR	141
4.3.1 LQR with sideslip angle	88	G Double wishbone suspension	143
4.3.2 LQR with accelerometer	90	G.1 Simscape model	143
4.4 Twin track model with the ACC	95	G.1.1 Double wishbone geometry model	143
4.4.1 Model matching	95	G.1.2 Forward kinematics	144
4.4.2 Maximal lateral acceleration .	97	G.1.3 Control law: nonlinear mapping	146
4.4.3 Cornering resistance and energy-saving	99	H Bibliography	148
5 Validation	100		
5.1 Robustness testing	100		
5.1.1 Low-level controller	102		
5.1.2 High-level controller	104		
5.2 Low-level reference testing	110		
5.2.1 Load variation effects	113		
5.3 High-level reference testing	114		
5.3.1 External disturbance	115		
5.3.2 Step response	117		
5.3.3 Steering disturbance	119		
5.3.4 Camber angle disturbance . .	121		
6 Conclusion	123		
6.1 Future work	125		
A Nomenclature	126		
B Calculation of the installation ratio IR	130		
C Derivation of McPherson suspension parameters	131		
D Derivation of the McPherson geometry model for the left side	134		
D.1 Forward kinematics	134		
D.2 Control law: Nonlinear mapping	135		
D.3 Unknown θ angle	136		

Figures

<p>1.2 The back view of the McPherson suspension with highlighted parts. The picture from: [1] 3</p> <p>1.3 Suspension diagrams with SA highlighted in dashed green line. 4</p> <p>1.4 Suspension diagrams with defined King-pin inclination (KPI), scrub radius and camber angle. 5</p> <p>1.5 Side-view of the suspension diagrams with defined caster angle for the front wheels. The displayed caster is positive. 6</p> <p>1.6 Friction circle development for different camber angles. The friction circle gets stretched to the left in F_y while squished in longitudinal force F_x. From: [2] 7</p> <p>1.7 Overview of published suspensions. From: [3] 9</p> <p>1.8 Comparison of different camber actuation architectures. From: [3] 10</p> <p>1.9 The used Simscape model of the McPherson suspension based on the Mathworks example [4]. The rail was added and the suspension parts approximated with cylindrical bodies. The d_L and d_R is the actuator stroke length on the rail line. The φ is the body roll. The L_{sL} and L_{sR} are the left and right McPherson strut lengths respectively and the h_L and h_R the piston heights. 12</p> <p>1.10 The Z-down coordinate system of the twin track vehicle with color fitting for each axis. 12</p> <p>1.11 New inputs/outputs of the twin track model. The τ_{ENG} and τ_{BRK} define the motor and braking torque that is employed at each wheel. 14</p>	<p>1.12 The Z-up coordinate system of the single track vehicle with color fitting for each axis. 15</p> <p>1.13 The single track diagram. The left and right wheels are moved to the center of each axle. 15</p> <p>2.1 The wheel with positive camber angle γ and the lateral blue camber thrust force F_t. 20</p> <p>2.2 The camber gain development based on the wheel travel between the McPherson and double wishbone suspension. The blue line depicts the McPherson and the red line the double wishbone. From: [5] 21</p> <p>2.3 The overview of the induced camber from different sources. The top figure shows the desired wheel inclination and the F_y denotes the lateral force of the vehicle in the maneuver, not the camber thrust. The other figures depict the induced camber in the maneuver. Note that the wheels are steered but it is not shown in the diagrams for the simplicity. 22</p> <p>2.4 The friction circle that defined the maximal longitudinal and lateral forces. The vector sum of F_x and F_y is limited by the μF_z value. 23</p>
--	--

2.5	On the far left is the real-world normal load distribution throughout the contact patch with blue rolling resistance opposing the motion. In the middle is the parabolic distribution used for the Brush model analysis. On the right side are the adhesion and sliding limits in the accordance to the parabolic distribution. From: [6]	24
2.6	The typical behavior of the tire going forward and at a slip angle. The slip angle is create as a reaction to the change in direction and diminishes when the new direction is established.	24
2.7	The top figure is the Brush Model of the tire for the slip angle with depicted side force F_y . On the bottom is the lateral force development cycle for increasing slip angle. The adhesion peak travels from the back to the front as it fills the sliding region. From: [6]	25
2.8	The top figure is the Brush Model of the tire for the camber angle with depicted side force F_y . On the bottom is the lateral force development cycle for increasing camber angle. The adhesion peak is reached at the same time through-out the contact patch. From: [6]	26
2.9	The lateral force of the Magic Formula in (2.1) across different tire slip angles.	27
2.10	The dependency of loss factor of different states of rubber on the temperature. The amount of stress (energy), it can withstand, is directly related to the friction coefficient in tires. From: [7]	28
2.11	The lateral force of the Magic Formula across different camber angles. The peak force value does not change. On the other hand, the force can be generated with no slip angle. The camber thrust diminishes at the force peak. The bottom figure shows only the force gained from the camber thrust.	29
2.12	Friction circle estimation as an ellipse from the complex Pacejka Magic Formula model from Matlab. The points with the highest euclidean norm are used for the estimation.	30
2.13	The comparison of the friction circles with different camber angles. The shifting of the friction circle is marked by an arrow.	31
2.14	The lateral and longitudinal force peak movement zoomed from Figure [2.13]. The gain in the lateral force is almost 4x higher than the loss in the longitudinal force.	31
2.15	The linearization of the Pacejka Magic Formula from the gradient of the curve around zero. The value of the slope at zero slip angle is the cornering stiffness.	33

2.16 The linearization of the Pacejka Magic Formula for the camber thrust. The average of all the camber thrust values at 0 slip angle is the cambering stiffness. The estimation of the camber thrust by cambering stiffness is depicted as the dashed lines for the particular camber angles.	34	2.21 The input and output diagram of the CTU demonstrator vehicle. The side slip angle β is estimated. The $[\delta_{ref}]$ marks the vector of 4 referenced steering angles from the driver or other control system. The vehicle picture from: [8].	39
2.17 The single track model with depicted cornering resistance forces F_{cf} and F_{cr}	35	2.22 The diagram defining the η angle for the McPherson suspension. It is the angle between the wheelbase and the lower control arm.	40
2.18 In the top figure is the lateral force response for the steering input. The peak is reached around 2 seconds so upto 1 second can be the curve considered linear. In the bottom is comparison of the force response between the conventional and the cambered wheel that uses $\Delta\gamma = 30^\circ/s$. The camber is saturated at $\gamma_{max} = 15^\circ$	36	2.23 Step response of the linearized system from the piston position to the body roll in [1.9].	45
2.19 The lateral force peak moves differently for given normal loads and camber angles. The camber angle moves peak almost horizontally while the normal load moves it diagonally. The arrows show the change for increasing γ and F_z values. The camber is changed from -15° to 15° and normal load from 80% to 120%. The green points show the peak movement for other than the nominal F_z and their curves are not shown for the simplicity.	37	2.24 The slew rate to low-pass filter relation.	47
2.20 Two different camber configurations. The left figure generates side force F_y while the right figure creates the yaw rate torque M_z	38	3.1 The camber gain from the roll angle in the Simscape suspension model with m_{axle} mass. The model was subjected to ramp of the side force $F_y = m_{axle} g$ for different mass variations.	51
		3.2 The calculation of the camber to rail ratio. The data are measured from the actuator stroke length defined as the extension of the prismatic joint to the camber angle of the wheel in the Simscape model of suspension	53
		3.3 The model of the actuator with input d_{act} and output distance d to the prismatic joint in the Simscape. The $\tau = 1/29 \text{ s} \approx 0.035 \text{ s}$ while the saturation is from 0 – 24 cm and the rate limiter $\pm 35.4 \text{ cm/s}$. The picture of the prismatic joint from: [9]. . . .	54
		3.4 The normal and lateral force development through the McPherson suspension for the right wheel. . . .	54

3.5 The normal and the lateral force development through the suspension with negative camber for the left turn.	56	3.15 The roll angle estimation when cornering with and without the complementary filter.	67
3.6 The normal and the lateral force development through the suspension with positive camber for the right turn.	57	3.16 The roll angle estimation from the bumps and holds in the road with and without the complementary filter. Whenever, the wheel is in the air, the equation (3.38) fails to predict the roll angle properly.	68
3.7 The force estimation needed for the actuator to achieve the required speed defined in Actuator requirements	58	3.17 The derivation of the camber influence compensation on the roll angle.	70
3.8 The derivation of the radius R_c of the rail that minimizes the angle change between the McPherson strut and the rail for the $\sigma_{shf} = 10^\circ$	59	3.18 The estimation of the roll angle with the camber actuation. The new camber-compensated estimator is compared to the one defined by (3.38). The cornering is simulated as the lateral force $F_y = m_{axle} a_y$ for $m_{axle} = \frac{m}{2}$ and $a_y = 1g$	71
3.9 The force estimation needed for the actuator to achieve the speed defined in table [3.2].	60	3.19 The estimation of the roll angle with the camber actuation. The rail is curved in a such a way that minimizes the change in angle between the McPherson strut and the rail. Thus, the non-linearity of Figure [3.17] is removed and the data can be approximated with less error.	72
3.10 McPherson suspension modeled as 5 points. (for background picture see McPherson)	62	3.20 The diagram for the derivation of the θ angle from the model in Figure [3.10].	74
3.11 Forward kinematics for camber angle γ of model in Figure [3.10]	63	3.21 Model verification of the step response between the Simcape model and its linearization from the estimated camber to the d_{act} distance.	75
3.12 The Simscape model with green-highlighted points as in the suspension model in Figure [3.10]. The disk around the points remarks the rotational degree of freedom of the joint.	64		
3.13 The nonlinear mapping controller diagram. The time constant of the low-pass filter is the same as in the actuator requirements in equation (2.21). The saturation is upto 24 cm and the rate limiter to 18.5 cm/s	65		
3.14 Roll estimation diagram with the complementary filter.	66		

3.22	The step response of the close loop of the controller and linearized system. The boundary conditions define the area where the controller requirements would be violated. The rise time requirement is taken equal to the steady state. The steady state is achieved when the response value reaches the specified range of 5% of its final value.	76
3.23	The diagram for the PI controller with back-calculation anti-windup with K_b and the reference γ_w with feedback from the γ estimator. The PI controller outputs d_{act} that is added to the nonlinear mapping controller output.	77
3.24	Forward kinematics for KPI angle of model in Figure [3.10]	78
4.1	The example for the centripetal acceleration a_c and the side acceleration \dot{v}_y	81
4.2	The handling characteristic graph of the vehicle describing the oversteer, neutralsteer and understeer tendency from: [10]. The $\alpha_1 = \alpha_f$ and $\alpha_2 = \alpha_r$ and $\delta = \delta_f$	83
4.3	The single track model in the steady state cornering maneuver with the constant radius R	86
4.4	The diagram of the double i -LQR with r_{ref} and β_{ref} or $\epsilon_{\dot{v}_{ref}}$ reference and state feedback.	87
4.5	The generic i -LQR structure with inputs x_{ref}, y, x , action output and state feedback gain K . The anti wind-up from the Saturation diagram [4.6] is fed to the integrator to prevent wind-up.	87
4.6	The saturation limitation as discussed in Actuator range with the low-pass filter to mode the actuator dynamics. The back-calculation method creates the anti wind-up signals that are fed to the LQR. The rate-limiter is omitted so that the step responses are simpler to read through. Note that the impact of the rate-limiter is captured mainly in the rate of change of the signal and not in the dynamics due to the anti wind-up. The $-\epsilon_{\dot{v}_{ref}}$ is negated at the output due to the different notation from (4.54).	88
4.7	The step response of the single track with r and β i -LQR without saturation or low-pass limitations.	90
4.8	The step response of the single track with r and ϵ_v i -LQR without saturation or slew rate limitations.	94
4.9	The model matching technique that can change vehicle behavior from understeer to oversteer in the steady state cornering with radius $R = 60$ m. The nominal twin track model is highlighted in blue. The other black dashed lines are references are created for different ΔCG . All responses are to the nominal twin track model.	96
4.10	The handling characteristic for the constant radius of the turn $R = 60$ m for vehicle with only front wheel steering ($\delta_r = 0$) and $\frac{\partial \delta_f}{\partial t} = 0$. The velocity increases in time. The oversteering and understeering twin track model response are compared with and without ACC.	97

4.11 The constant radius of a turn maneuver $R = 60$ m with increasing velocity for only front steering vehicle ($\delta_r = 0$). The vehicle is the same as defined in the parameters but it is slightly understeering with CG shifted by 5 cm to the front from the center.	98
4.12 The example of the right turn with and without the ACC. The vehicle turns only with the front wheels $\delta_f = 5^\circ, \delta_r = 0^\circ$ and the velocity is $V_x = 54$ km/s. The last graph compares the cornering losses. The vehicle with ACC is 45 % more efficient and consumes less energy through slip.	99
5.1 The general definition of the plant model $P(s)$	101
5.2 The bode plot envelope of the linearized set of the $G_{nom}(s)$ for the boundary conditions.	102
5.3 The bode plot envelope of uncertainties estimated from [5.2] that constitutes the $G(s)$ model.	103
5.4 The Low-level controller plant model. The non-linear mapping $F(u)$ is left out.	104
5.5 The bode plot envelope for the boundary conditions.	106
5.6 The bode plot envelope for the boundary conditions excluding velocity.	106
5.7 The bode plot envelope of uncertainties estimated from [5.2] that constitutes the $G(s)$ model.	107
5.8 The High-level controller plant model with LQR using β	108
5.9 The High-level controller plant model with LQR using ϵ_v	109
5.10 The High-level controller plant model with LQR using β for disturbance in γ_f and γ_r	110
5.11 The step response of the nonlinear mapping controller using the real body roll angle and the estimated variant. The rate limiter has $\mu_{rate} = 18.5$ cm s ⁻¹ and the low-pass filter $\tau = 1/29$ second.	111
5.12 The step response of the close loop with the nonlinear mapping and PI controller using the real body roll angle and the estimated variant. The rate limiter has $\mu_{rate} = 18.5$ cm s ⁻¹ and the low-pass filter $\tau = 1/29$ second.	112
5.13 Load variation of the Simscape model with passive camber angle 2°	113
5.14 The comparison of passive camber angle with $\gamma = 2^\circ$ and Active Camber Control against the load variation of the axle.	114
5.15 The duplet disturbance signal for the yaw rate and side slip angle.	115
5.16 The side slip angle disturbance with duplet with amplitude $\beta_d = 2^\circ$	116
5.17 The yaw rate disturbance with duplet with amplitude $r_d = 5^\circ$	117
5.18 The step response to the input command $\delta_f = \delta_r = 2^\circ$	118
5.19 The step response to the input command $\delta_f = 2^\circ$ and $\delta_r = -2^\circ$	119
5.20 The front steering disturbance response with $\delta_{f_{err}} = 1^\circ$	120
5.21 The rear steering disturbance response with $\delta_{r_{err}} = 1^\circ$	121

5.22 The response of the system to the front camber angle disturbance $\gamma_{fa} = 5^\circ$	122	G.3 Forward kinematics for camber angle γ angle of model in Figure [G.1].....	146
B.1 The calculation of the IR for the McPherson suspension.	130		
C.1 The diagram of the McPherson parameters from table [C.1].....	132		
C.2 The triangles from Figure [C.1] used for the derivation of parameters.	133		
D.1 Forward kinematics for camber angle γ for the left side geometry model of the McPherson suspension.	135		
D.2 The derivation of the θ angle for the left side geometry model of the McPherson suspension.	136		
E.1 The definition of the coordinate systems of the wheel: C wheel-body coordinate frame, the W wheel coordinate frame and the T tire coordinate frame. Picture from: [11]	138		
F.1 The state-feedback gains dependence on the velocity for the LQR with β	141		
F.2 The state-feedback gains dependence on the velocity for the LQR with a_y	142		
G.1 Double wishbone suspension modeled as 5 points (background picture from: [12])	144		
G.2 Forward kinematics for θ angle of model in Figure [G.1].	146		

Tables

2.1 CTU demonstrator vehicle parameter list	40
3.1 The table describing the total amount of the camber angle needed to compensate for the different camber gains and parasitic effects for the right turn.	52
3.2 The actuator parameters used in the CTU demonstrator vehicle.	60
A.1 CTU demonstrator vehicle nomenclature list. The nominal units are used in all equations and derivations.	126
C.1 The practical set of McPherson suspension parameters	131

Chapter 1

Introduction

1.1 Motivation

The car industry has seen a boom in the last 100 years. Everybody now owns a car and uses it every day. It is part of our life, making its safety and performance aspect vital. The vehicles have multiple safety systems to safeguard drivers and pedestrians, and one of the most important is the ABS and ESP. Nowadays, they are mandatory equipment in every car, which speaks about their importance. The vehicle skid is a life-threatening phenomenon caused by a wide range of different reasons like changing weather conditions, the state of the tires, etc. Thus, it is imperative to avoid it, and that is where the ABS and ESP come in. The ABS keeps the wheels from sliding while the ESP controls the vehicle's turning moment to follow the route specified by the steering wheel input. Specifically, they are capable of using the friction circle efficiently so that the force output is maximized while keeping the vehicle from skid and on track. The friction circle governs the maximal longitudinal and lateral forces the vehicle can create. For example, whenever the wheel goes over the pocket of water or ice, the tires' adhesion is lowered, and thus the friction circle is smaller. The ABS and ESP act and react to this change by distributing the braking moment.

However, there are still almost 6.75 million yearly car crashes in the US alone, see [13]. The work of ABS and ESP is nothing short of amazing and saved countless lives, but there are still ways how to increase the active safety of cars. The over-actuated vehicle offers such options, and one of them is the active camber actuation. The active camber can change the friction circle mid-corner to optimize it for the generation of the higher lateral forces. This would not be possible if the camber were held constant. So, instead of using only wheel steering, the vehicles can use camber in conjunction with steering

to maneuver the car. The camber can provide faster force generation, less tire wear, larger contact patch size, and it is more energy-efficient than tire slip angle. It is highly desirable to investigate camber and build safer and more efficient vehicles.

■ 1.2 Suspension types

The vehicle mass is split into sprung and unsprung mass. The unsprung mass sits directly on the ground, and it is composed of the mass of the wheels, axle tracks, and components directly connected to them. The sprung mass includes body, frame, passengers, cargo, and internal components. The larger the sprung to unsprung mass ratio is, the less the passengers are affected by bumps and other road imperfections. The connection between the two masses ensures suspension. There are two main suspension types that are commercially used: **McPherson** and **Double wishbone**.

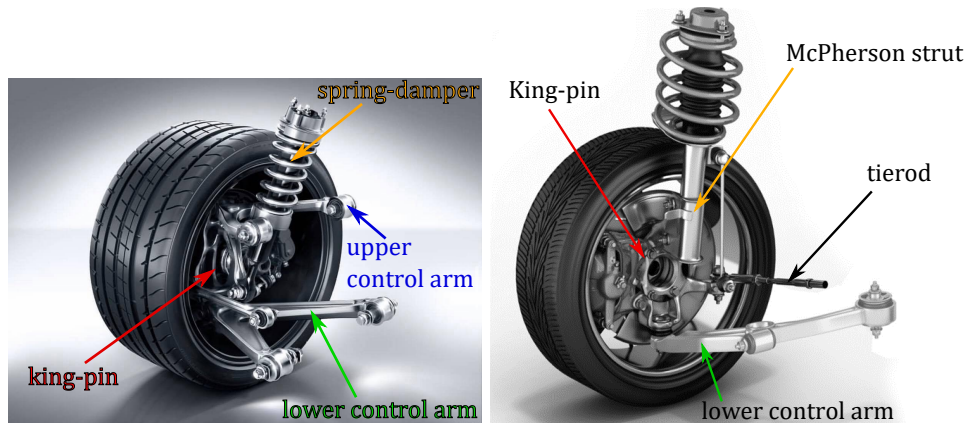
■ 1.2.1 Double wishbone

The double wishbone suspension consists of two control arms and a spring-damper. The upper and lower control arm connects the sprung mass to the unsprung mass through the king-pin that holds the wheel. The sprung mass is supported via a spring-damper mounted to the lower control arm. The wheel alignment is consistent for different steering angles, and the suspension also generates negative camber when cornering, which increases stability and better grip for the tires. The longer the wishbone arms are, the more linearly the wheel will move up and down.

■ 1.2.2 McPherson

The McPherson suspension uses only one lower control arm and spring damper McPherson strut. The lower control arm connects the sprung mass to the kin-pin, and the spring damper, which supports the sprung mass, is mounted directly to the top of the king-pin, see Figure [1.2]. The McPherson is widely used in conventional vehicles because it decreases cost, takes less space, and weighs less than the double wishbone. That is why it was chosen for the CTU demonstrator vehicle. The only disadvantage is that it is generally less stable and inconsistent for different wheel alignments. Also, the McPherson has less negative camber gain when cornering, which facilitates the worst cornering performance. The lower arm moves at an arc, but the upper strut moves linearly, and thus at first, the camber is generated in the right way

but then lost at higher wheel positions. However, these negative effects can be overcome with the over-actuation of the vehicle.



(a) : Double-wishbone suspension with described parts. Picture from: [14].

(b) : McPherson suspension with described parts. Picture from: [15].

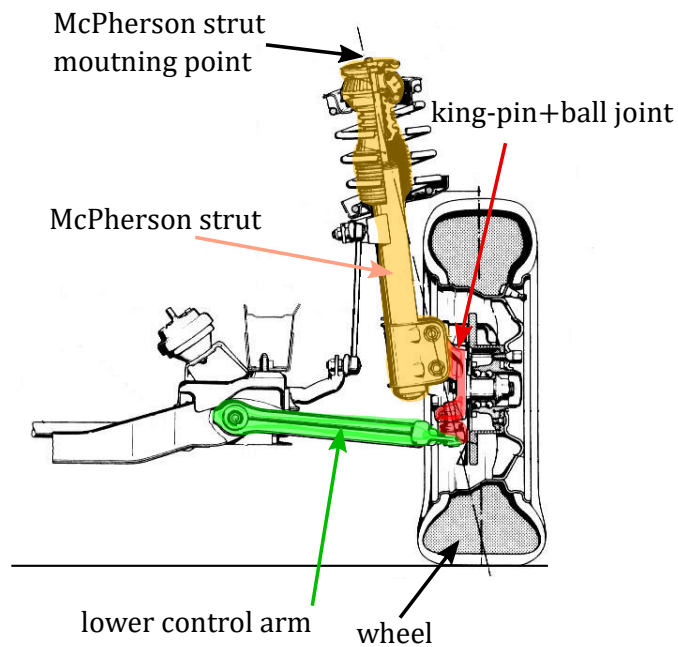


Figure 1.2: The back view of the McPherson suspension with highlighted parts. The picture from: [1]

1.3 Suspension terms

The suspension have multiple terms that define its behavior and functionality. They are going to be defined here.

1.3.1 Steering axis

The steering axis (SA) is the axis around which the wheel rotates when steered by the driver. The double wishbone defines it as the two mounting joints of the king-pin to the two control arms, see left Figure [1.3].

The McPherson king-pin is mounted rigidly to the spring-damper. Thus, the steering axis extends from the lower joint of the king-pin to the mounting joint of the McPherson strut, see right Figure [1.3].

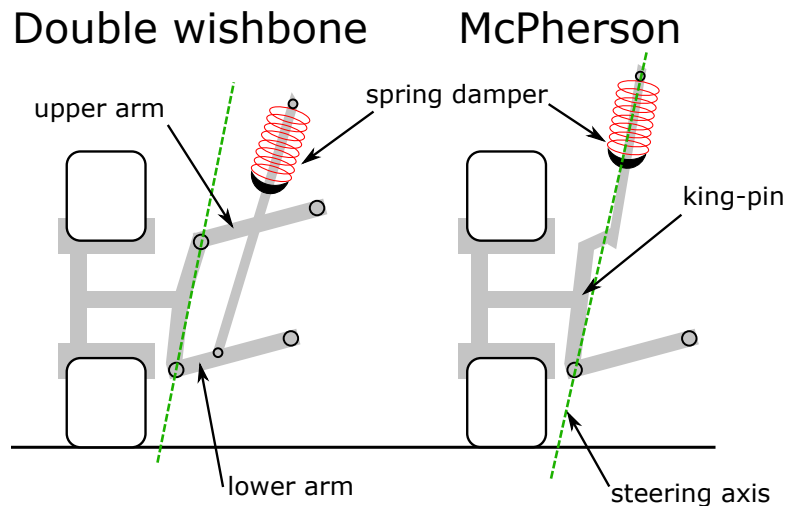


Figure 1.3: Suspension diagrams with SA highlighted in dashed green line.

1.3.2 KPI and scrub radius

The KPI stands for King-Pin Inclination, and it defines an angle of the inclination of the steering axis to the plane perpendicular to the ground, see Figure [1.4]. It is sometimes also called SAI or Steering Axis Inclination. It is used to minimize scrub radius in car manufacturing.

The scrub radius is defined as the distance between the intersection of the steering axis with the ground and the contact patch center of the tire, see Figure [1.4]. The scrub radius acts as a moment arm with the longitudinal force centered at the contact patch on the wheel. The moment creates strain

on the steering knuckle, and the steering actuator must withstand these very large moments, especially at high speeds. Thus, the scrub radius should be minimized as much as possible. Note that most commercial cars use steering systems that connect the right and left side steering mechanisms rigidly on each axle, which cancels this effect.

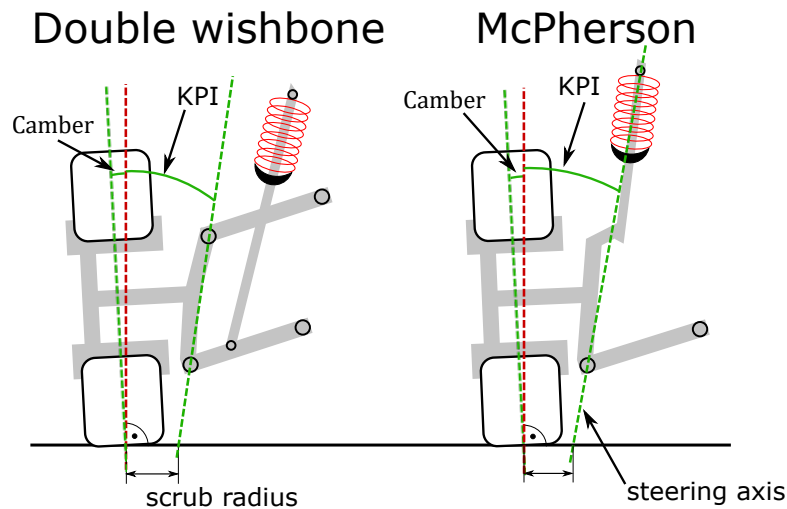


Figure 1.4: Suspension diagrams with defined King-pin inclination (KPI), scrub radius and camber angle.

■ 1.3.3 Camber angle

The camber angle is defined as the angle between the wheel axis and the plane perpendicular to the ground, see diagram [1.4]. For more information about the camber see **Problem definition**.

■ 1.3.4 Caster angle

The caster angle is the inclination angle between the joints of the steering axis looking from the side of the vehicle, see Figure [1.5]. It creates force feedback for the wheel because it points the steering wheel in the direction the car is going in because the steering axis intersects the ground before the contact patch center. It is very beneficial at high speeds because it is self-centering. It is also used to passively lean the wheels into the corner, providing better lateral stability. However, the more caster angle, the heavier the steering is, and thus the steering actuator would have to be stronger.

Nevertheless, if the caster angle is too high, it could reduce the contact

patch size and cause a tire shake or shimmy. Thus, the smaller caster angles are employed to avoid using stronger steering actuators, but the car loses the beneficial camber in the cornering. The negative caster angle is not used in the car industry because it would constantly move wheels away from the vehicle's direction.

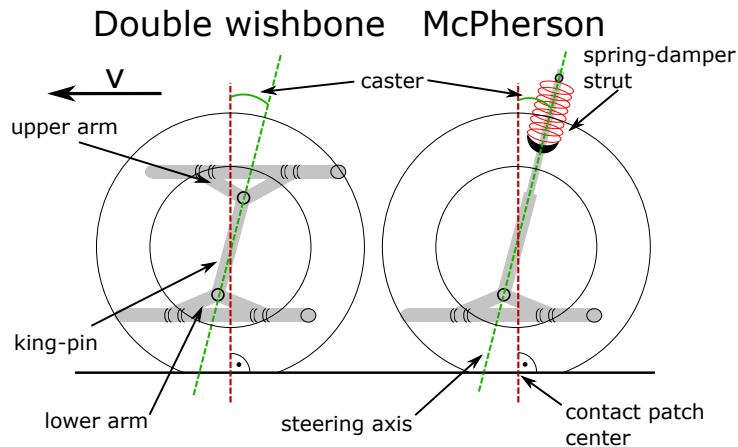


Figure 1.5: Side-view of the suspension diagrams with defined caster angle for the front wheels. The displayed caster is positive.

1.4 State-of-the-art

In this section is a brief overview of the articles and works that were already published about this topic.

The camber angle and toe angle vary substantially when driving. They are influenced by many factors like wheel travel or body roll and can have negative consequences on the vehicle performance by the changing lateral grip. The article [16] sets to mitigate these fluctuations. Two actuators were used to change arm lengths in the double-wishbone suspension, and feedback PID control was used to drive them. The camber angle variation was decreased by 58% and toe angle by 96%. The high camber angle can be undesirable if the longitudinal acceleration is the priority. The effect of camber on the tire force is presented in the study [2]. It is demonstrated that the camber increases lateral forces, and the friction circle is squished in the longitudinal direction and prolonged in the lateral direction, see Figure [1.6]. Thus, the camber actuation enables the car to maximize the cornering force if the turn is too sharp or hold the camber angle at 0 if the acceleration is the priority.

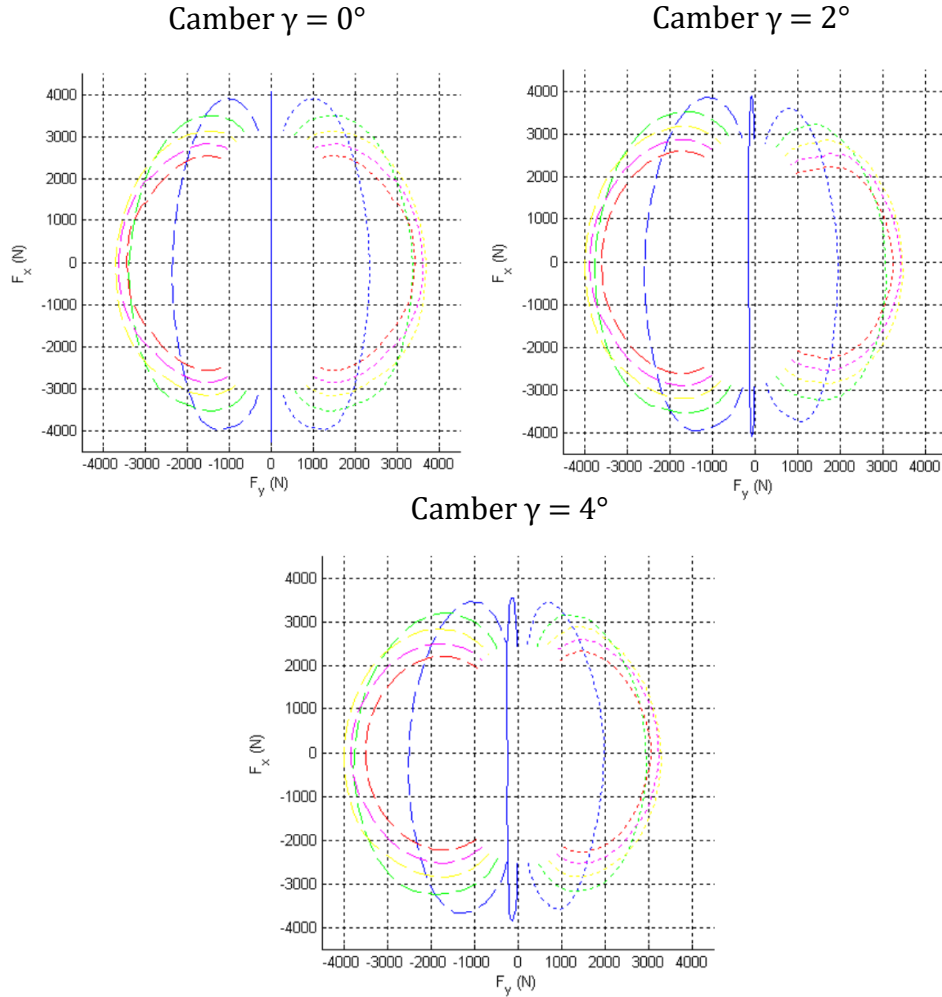


Figure 1.6: Friction circle development for different camber angles. The friction circle gets stretched to the left in F_y while squished in longitudinal force F_x . From: [2]

The active camber MPC controller was developed to increase path following, and yaw stability in [17]. The generation of forces was modeled by modified Dugoff-tyre model where the effect of camber on the lateral force was formed by a linear component. The MPC framework is used to subject the control law to the limitations of the actuator and the road. It was tested on the Double Lane Change (DLC) maneuver, and it facilitated higher passing velocity and better performance across all of the road conditions tested. In the dissertation, [6] is developed new mechatronic suspension in such a way that maximizes

the effect of the camber angle on the lateral forces. The classical tires are not well-suited to high camber angles and thus produce less camber thrust. That is why a new semi-empirical brush model was developed that telegraphs tire parameters that facilitate higher camber thrust gains and could be used to develop new types of tires. PD position controllers control the camber angle to satisfy design criteria. The vehicle had almost 30 % more cornering force and higher maneuverability.

The [3] focused on the steering feel of drivers with passive or active camber actuation that was based on the yaw rate and the lateral acceleration feedback. The active actuation had a better feel of control, and drivers struggled less to maintain the given maneuver. The paper also provides a comprehensive overview of the already designed suspensions for the active camber actuation, see Figure [1.7]. The table compares the points of actuation, space requirements, and unsprung weight. The trade-off between these columns can be effortlessly observed. The lower actuation point has smaller space requirements but adds more unsprung weight. The upper has more space requirements but adds almost no unsprung weight because the actuator is mounted on the chassis. The middle point of the actuation requires the redevelopment of the whole wheel hub and king-pin and can be very expensive while still requiring more space and increasing unsprung mass, as can be seen from Siemens and Skew cylinders in the table [1.7]. The different points of the actuation are also compared in power and camber angle range, see Figure [1.8]. The upper point has lower power requirements than the middle and the lower.

On the other hand, the camber can be used as a means of reducing energy consumption. In the [18] is shown that tire slip angle is the primary energy loss component while cornering. The [19] uses energy cost functions to evaluate the best camber angles, so the energy loss is minimized. It was found that the camber control can save up to 15 % of the energy in the sharp turns. However, high camber angles can induce high rolling resistance forces in mild maneuvers and reduce the savings.

Mercedes-Benz made many improvements throughout the years and pushed many boundaries in the development of high-performance cars. One of the most interesting and intriguing was the Formula 1 Mercedes with active toe-in and toe-out. They developed a mechanism that moved wheels towards or away from each other and could be controlled dynamically by the driver. The toe-out increases maneuverability but has large tire wear in the straights. On the other hand, the toe-in provides more stability on the straights but decreases the maneuverability. That is why the driver had a huge advantage as he could control it as he saw fit by moving the steering wheel towards

or away from him. The active toe-in and toe-out were used commercially during the Formula 1 race championship, making the active camber actuation approach appealing because it has very similar benefits while having fewer disadvantages than the toe. Another invention was the Mercedes Carving. It has an active camber suspension system and uses specialized tires that facilitate higher camber thrust gains. It had an impressive maximal lateral acceleration of $1.28g$, and the ESP was augmented to use the camber angles in conjunction with the braking distribution. It was able to decrease braking distance by 5 m from 100 km/h test. These achievements confirm what the active camber control is capable of and its capacity to improve safety and performance.






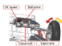






Actuation Mechanism	Figure	Max camber range	Point of actuation	Ready for active toe	Prototyped	Area of use	space requirements	additional unsprung mass weight
Ferrari [2]		$-6^\circ < \gamma < -1.5^\circ$	upper	yes	yes	sport	negligible	medium
Toyota [15]		$-5^\circ < \gamma < 5^\circ$	lower	yes	no	urban	negligible	high
Volvo [16]		$-5^\circ < \gamma < 5^\circ$	lower	yes	yes	urban	negligible	high
Caster angle [17]		$-12^\circ < \gamma < 12^\circ$	upper	no	no	road	medium	medium
UW longitudinal translation [18]		$-1^\circ < \gamma < 1^\circ$	upper	no	no	road	medium	negligible
UW lateral translation [11]		$-20^\circ < \gamma < 20^\circ$	upper	no	no	road	much	negligible
Stanford thesis [9]		$-45^\circ < \gamma < 45^\circ$	upper	no	yes	road	much	negligible
Crank bar upper wishbone [19] [20] [21] [22]		$-5.5^\circ < \gamma < 5.5^\circ$	upper	no	yes	(off-)road	negligible	negligible
Crank bar lower wishbone [23]		$-5.5^\circ < \gamma < 5.5^\circ$	lower	no	yes	urban	negligible	medium
Skew cylinders [24]		$-60^\circ < \gamma < 60^\circ$	middle	yes	yes	road	much	high
Mercedes [8]		$-30^\circ < \gamma < 0^\circ$	lower	no	yes	road/sport	much	high
Siemens [25]		$-4^\circ < \gamma < 4^\circ$	middle	yes	yes	urban	negligible	high

Figure 1.7: Overview of published suspensions. From: [3]

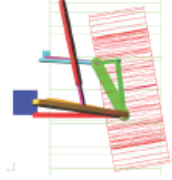
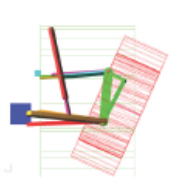
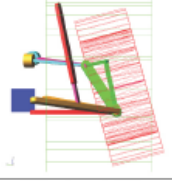
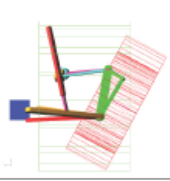
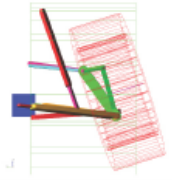
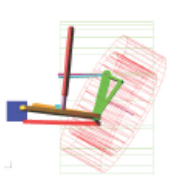
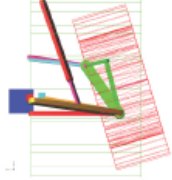
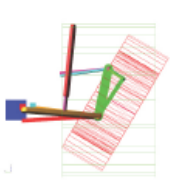
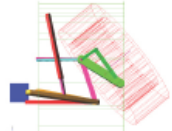
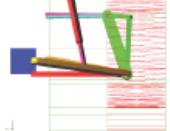
Type	Workspace / Actuator displacement without vertical wheel travel	Workspace / Actuator displacement with a minimum of -100mm - 100 mm vertical wheel travel	Camber dependency while vertical wheel travel from -100mm to 100mm	Actuation power
Upper wishbone length of rods	$-19.5^\circ < \gamma < 30^\circ$ $-65mm < \delta < 130mm$ 	$-10^\circ < \gamma < 25^\circ$ $-35mm < \delta < 100mm$ 	$< 4.5^\circ$	low
Upper wishbone position of joint	$-20^\circ < \gamma < 35^\circ$ $-70mm < \delta < 150mm$ 	$-15^\circ < \gamma < 30^\circ$ $-55mm < \delta < 120mm$ 	$< 5^\circ$	low
Lower wishbone length of rods	$-30^\circ < \gamma < 40^\circ$ $-120mm < \delta < 200mm$ 	$-18^\circ < \gamma < 30^\circ$ $-75mm < \delta < 150mm$ 	$< 3.5^\circ$	high
Lower wishbone position of joint	$-27.5^\circ < \gamma < 40^\circ$ $-90mm < \delta < 170mm$ 	$-16.5^\circ < \gamma < 30^\circ$ $-60mm < \delta < 130mm$ 	$< 3.5^\circ$	high
On the knuckle	$-40^\circ < \gamma < 0^\circ$ $-0mm < \delta < 0mm$ 	$-30^\circ < \gamma < 0^\circ$ $-0mm < \delta < 0mm$ 	$< 5^\circ$	high

Figure 1.8: Comparison of different camber actuation architectures. From: [3]

1.5 Toolboxes

The models and toolboxes used in this thesis are put forward in this section. Some of the models were augmented to fit this thesis task.

1.5.1 Simscape model of suspension

The suspension dynamics are very delicate and difficult to model with ordinary differential equations in the single or twin track models. That is why the suspension is modeled separately with Simscape developed by Mathworks [4] that uses physical modeling to create differential equations from the interaction between the given masses. The benefit of this approach is that the actuation system can be designed more precisely while the high-level control is separated as it does not require such accurate models of the suspension to design. The framework used is called the Simscape Multibody library.

The Mathworks [4] provides an example for the double wishbone and McPherson suspension models. The McPherson model closely resembles the McPherson used in the real environment, compare Figure [1.2] and [1.9]. Each part type like king-pin, control arms etc. is modeled individually as a component from the Multibody library. The suspension is mounted on a test platform with pistons that can be used to create disturbances like road bumps etc., see Figure [1.9]. The components are connected through joints that allow the movement between the suspension parts but their friction and displacements are neglected.

For the purpose of this thesis, the model was altered. The model parameters are changed so that they match the testing vehicle. The axices are changed to the Z-up configuration. The steering capability is not needed, and the model behavior is studied only in the YZ plane, see Figure [1.9]. Thus, the lower arm and the king-pin are modeled as cylindrical bodies to ease the parametrization requirements. The McPherson strut mounting point for the sprung mass is made loose, but the rail line constrains its movement. The actuator can move the mounting point around the rail and thus change the camber angle. The rail is tilted by σ_{shf} angle, which is the same as the angle of the McPherson strut from the king-pin so that the McPherson strut is perpendicular to the rail at 0 camber angle. The McPherson strut mounting point has a revolute joint with 1 DOF so that the suspension can rotate only around X-axis that is defined from the right triad as going into the paper. The actuator itself is modeled as a prismatic joint that has for the input the distance d which marks the shift of the mounting point on the rail.

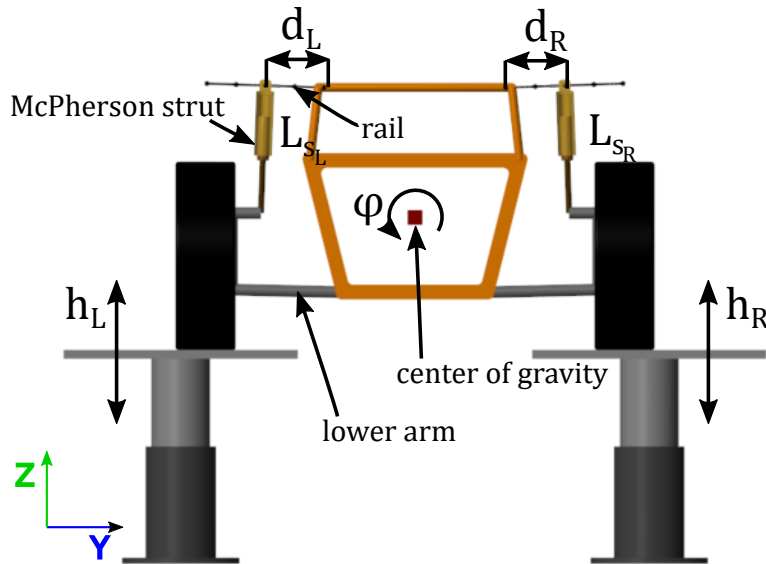


Figure 1.9: The used Simscape model of the McPherson suspension based on the Mathworks example [4]. The rail was added and the suspension parts approximated with cylindrical bodies. The d_L and d_R is the actuator stroke length on the rail line. The φ is the body roll. The L_{s_L} and L_{s_R} are the left and right McPherson strut lengths respectively and the h_L and h_R the piston heights.

1.5.2 Twin track

Hi-fi non-linear mathematical model representing complex vehicle dynamics including dynamical load transfer is adopted from [20]. The original model consists of 4 Pacejka wheels together with Newton-Euler equations of motion, aerodynamic forces and power-train. The vehicle coordinate system is shown in Figure [1.10].

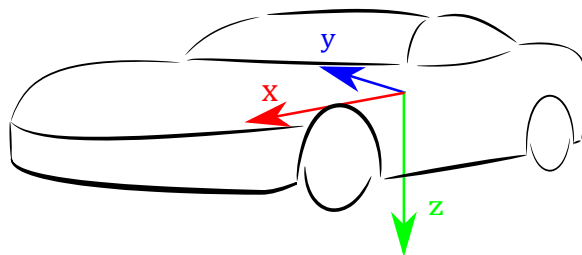


Figure 1.10: The Z-down coordinate system of the twin track vehicle with color fitting for each axis.

However, the Pacejka wheels defined in ([20]-2.27) and ([20]-2.28) in the original model do not simulate the wheel camber effect. To address this, the complex Pacejka Magic Formula [21] is employed replacing the previous model. It is implemented in the Mathworks library [4] as "**Combined-Slip Wheel 2DOF**".

The coordinate transformation in ([20]-2.24) accounts only for the steering angle but not for the rotation by the camber angle. Moreover, the **Combined-Slip Wheel 2DOF** have Z-up coordinate system where the vehicle is Z-down, see Figure [1.10]. Thus, a DCM is used instead of ([20]-2.24) where the velocities are transformed as

$$v^w = R_z(\delta) R_y(0) R_x(\pi + \gamma) v^b, \quad (1.1)$$

from the body CG point to the individual wheels and the forces

$$F^b = R_z(\delta) R_y(0) R_x(\pi + \gamma) F^w, \quad (1.2)$$

from the wheels to the body coordinate system where $R_i()$ is the rotational matrix around the particular axis. The π rotation around X axis rotates between Z-up and Z-down coordinate system. The δ and γ are not subtracted as the δ is after the rotation around X which changes the direction of rotation and the γ is from the definition of the wheel axes for the complex Pacejka Magic Formula. The complex Pacejka Magic Formula also requires brake pressure P_b instead of torque τ_{BRK} and thus a conversion formula is used:

$$P_{b_{xx}} = \frac{4 \tau_{BRK_{xx}}}{\mu \pi B_a^2 R_m N_{pads}}, \quad (1.3)$$

where R_m is the brake pad mean radius, N_{pads} is the number of brake pads, B_a is the disk brake actuator bore and μ is the kinetic friction coefficient. Their values are the same as the default values from the Mathworks block.

Next, the vehicle interaction equations in (2.4-2.16) from [20] were also augmented. The skew matrix of lengths is used to map the forces F^b and rotational speed ω^b to the moment M^b and the velocity v^b :

$$M^b = \sum_{xx=FL,FR,RL,RR} \left(\begin{bmatrix} 0 & h_{xx} & w_{xx} \\ h_{xx} & 0 & -L_{xx} \\ -w_{xx} & L_{xx} & 0 \end{bmatrix} F_{xx}^b \right), \quad (1.4)$$

$$v_{xx}^b = \sum_{xx=FL,FR,RL,RR} \left(\begin{bmatrix} 0 & h_{xx} & -w_{xx} \\ -h_{xx} & 0 & L_{xx} \\ w_{xx} & -L_{xx} & 0 \end{bmatrix} \omega^b \right), \quad (1.5)$$

where L_{xx} is the longitudinal length, w_{xx} the lateral length and h_{xx} the vertical length from the CG point to the each wheel.

The model has to be influenceable by external disturbances like the side wind or the wind gust that rotates the vehicle by hitting a trailer, for example. In other words, the model has to include inputs for external forces and moments. So, the equations (1.4) and (1.5) were updated to:

$$M^b = \sum_{xx = \text{FL,FR,RL,RR}} \left(\begin{bmatrix} 0 & h_{xx} & w_{xx} \\ h_{xx} & 0 & -L_{xx} \\ -w_{xx} & L_{xx} & 0 \end{bmatrix} F_{xx}^b \right) + \begin{bmatrix} 0 \\ F_{y_{\text{ext}}} \\ 0 \end{bmatrix}, \quad (1.6)$$

$$v_{xx}^b = \sum_{xx = \text{FL,FR,RL,RR}} \left(\begin{bmatrix} 0 & h_{xx} & -w_{xx} \\ -h_{xx} & 0 & L_{xx} \\ w_{xx} & -L_{xx} & 0 \end{bmatrix} \omega^b \right) + \begin{bmatrix} 0 \\ 0 \\ M_{z_{\text{ext}}} \end{bmatrix}, \quad (1.7)$$

where $F_{y_{\text{ext}}}$ can be used to model the side wind gust and $M_{z_{\text{ext}}}$ can be used to exert the external rotation which have direct consequences on the vehicle yaw rate and side slip angle. The new inputs and outputs of the twin track model are depicted in Figure [1.11].

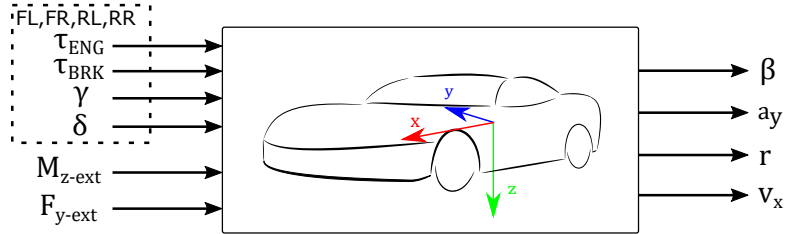


Figure 1.11: New inputs/outputs of the twin track model. The τ_{ENG} and τ_{BRK} define the motor and braking torque that is employed at each wheel.

1.5.3 Single track mathematical model

The single track model represents simplification adopted from [22]. The vehicle coordinate system is shown in Figure [1.12].

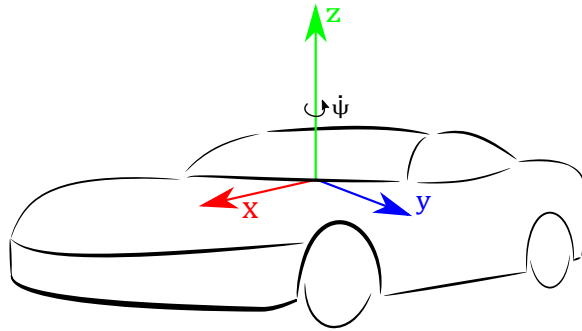


Figure 1.12: The Z-up coordinate system of the single track vehicle with color fitting for each axis.

The single track model is mainly used for the controller design and thus it will be linearized. However, the equations has to be extended by the camber angle actuation. The linearization procedure will be presented in three steps:

1. Equations of motion
2. Forces and torques
3. Final differential equations

■ Equations of motion

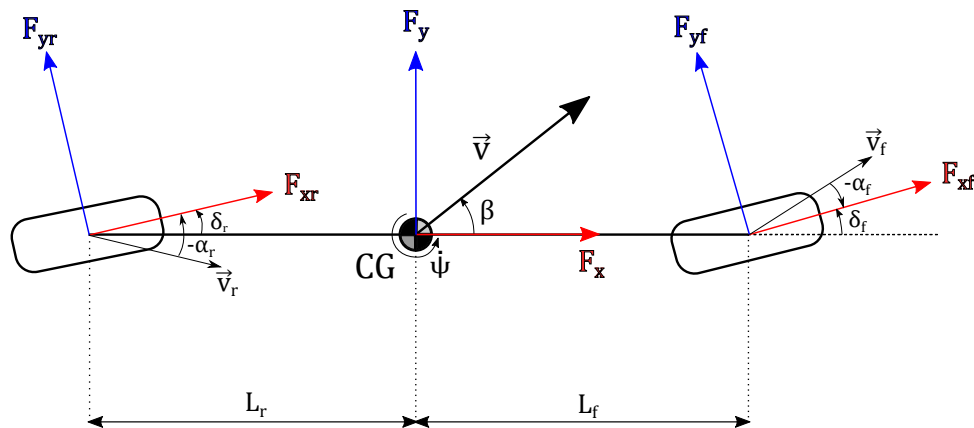


Figure 1.13: The single track diagram. The left and right wheels are moved to the center of each axle.

The nonlinear equation of motion for the diagram in Figure [1.13] are:

$$F_x = m \dot{v}_x, \quad (1.8)$$

$$F_y = m \dot{v}_y, \quad (1.9)$$

$$M_z = J \ddot{\psi}, \quad (1.10)$$

where \dot{v}_x is a longitudinal acceleration, \dot{v}_y a lateral acceleration, m a vehicle mass, $\dot{\psi}$ a yaw rate, ψ a yaw angle and J a moment of inertia around Z-axis. The longitudinal and lateral force is marked as F_x and F_y respectively and the torque around Z-axis as M_z . The yaw rate notation of $r = \dot{\psi}$ will be adopted for this thesis. The velocity vector can be distributed to the longitudinal and lateral direction as follows:

$$v^2 = v_x^2 + v_y^2, \quad (1.11)$$

$$v_x = \vec{v} \cos(\psi + \beta), \quad (1.12)$$

$$v_y = \vec{v} \sin(\psi + \beta) = v_x \tan(\beta + \psi). \quad (1.13)$$

$$(1.14)$$

where \vec{v} is the velocity vector and β a sideslip angle. The equation (1.9) can be rewritten with (1.13) as:

$$F_y = m \left(\dot{v}_x \tan(\beta) + v_x \frac{\dot{\beta} + r}{\cos(\beta + \psi)^2} \right). \quad (1.15)$$

The lateral dynamics are primarily considered for the single track model. That is why the following assumptions are made:

- The longitudinal velocity is assumed constant $\dot{v}_x = 0$ and will be marked as V_x .
- The yaw angle is assumed to be $\psi = 0$ for the simplification.
- The β is assumed to be small and the following approximation of goniometric functions is employed:

$$\sin(\beta) \approx \beta, \quad \cos(\beta) \approx 1, \quad \tan(\beta) \approx \beta. \quad (1.16)$$

The final equations of motion with the assumptions above are:

$$F_y = m V_x (\dot{\beta} + r), \quad (1.17)$$

$$M_z = J \dot{r}, \quad (1.18)$$

where the $F_x = 0$. The linearized model considers only the lateral dynamics.

■ Forces and torques

The lateral force F_y and yaw torque M_z based on tire slip angles are going to be defined in this section. Based on Figure [1.13]:

$$F_y = F_{yf} + F_{yr}, \quad (1.19)$$

$$M_z = L_f F_{yf} - L_r F_{yr}, \quad (1.20)$$

where F_{yf} and F_{yr} are front and rear lateral wheel traction forces. They are defined by the Pacejka Magic Formula and their linearization for the small tire sideslip angles yields:

$$F_{yi} = C_{\alpha_i} \alpha_i + C_{\gamma_i} \gamma_i, \quad (1.21)$$

where $i = f, r$ for front and rear respectively. The C_{α_i} is the cornering stiffness and the C_{γ_i} the cambering stiffness, see section **Linearization of Pacejka Magic Formula** for more information. The term $C_{\gamma_i} \gamma_i$ accounts for the camber thrust force produced by a wheel cambering.

The wheel longitudinal v_{x_i} and lateral velocity v_{y_i} at the wheel coordinate system at the each axle center for the single track model can be defined as:

$$v_{x_i} = V_x, \quad (1.22)$$

$$v_{y_i} = v_y \pm L_i r, \quad (1.23)$$

$$(1.24)$$

where $i = f, r$ stands for front and rear respectively and the L_i is the distance of the CG to the front and rear axle respectively for particular i . The tire slip angle can be defined as arc-tangent of wheel longitudinal and lateral velocity, see Figure [1.13]:

$$\alpha_i = \tan\left(\frac{v_y \pm L_i r}{V_x}\right) + \delta_i. \quad (1.25)$$

The α_i are assumed small and thus the approximation of goniometric functions in (1.16) applies as well. The (1.25) reduces to:

$$\alpha_f = \delta_f - \beta - \frac{L_f}{V_x} r, \quad (1.26)$$

$$\alpha_r = \delta_r - \beta + \frac{L_r}{V_x} r. \quad (1.27)$$

■ Final differential equations

Substituting (1.26), (1.27) and (1.21) into (1.17) and (1.18) yields the system differential equations describing lateral dynamics of the single track model:

$$\dot{\beta} = -\frac{C_{\alpha_f} + C_{\alpha_r}}{m V_x} \beta + \left(\frac{L_r C_{\alpha_r} - L_f C_{\alpha_f}}{m V_x^2} - 1 \right) r + \frac{C_{\alpha_f}}{m V_x} \delta_f + \frac{C_{\alpha_r}}{m V_x} \delta_r + \frac{C_{\gamma_f}}{m V_x} \gamma_f + \frac{C_{\gamma_r}}{m V_x} \gamma_r, \quad (1.28)$$

$$\dot{r} = \frac{L_r C_{\alpha_r} - L_f C_{\alpha_f}}{J} \beta - \frac{L_f^2 C_{\alpha_f} + L_r^2 C_{\alpha_r}}{J V_x} r + \frac{L_f C_{\alpha_f}}{J} \delta_f - \frac{L_r C_{\alpha_r}}{J} \delta_r + \frac{L_f C_{\gamma_f}}{J} \gamma_f - \frac{L_r C_{\gamma_r}}{J} \gamma_r. \quad (1.29)$$

Its state-space form is:

$$\begin{bmatrix} \dot{\beta} \\ \dot{r} \end{bmatrix} = \begin{bmatrix} -\frac{C_{\alpha_f} + C_{\alpha_r}}{m V_x} & \frac{L_r C_{\alpha_r} - L_f C_{\alpha_f}}{m V_x^2} - 1 \\ \frac{L_r C_{\alpha_r} - L_f C_{\alpha_f}}{J} & -\frac{L_f^2 C_{\alpha_f} + L_r^2 C_{\alpha_r}}{J V_x} \end{bmatrix} \cdot \begin{bmatrix} \beta \\ r \end{bmatrix} \\ + \begin{bmatrix} \frac{C_{\alpha_f}}{m V_x} & \frac{C_{\alpha_r}}{m V_x} \\ \frac{L_f C_{\alpha_f}}{J} & -\frac{L_r C_{\alpha_r}}{J} \end{bmatrix} \cdot \begin{bmatrix} \delta_f \\ \delta_r \end{bmatrix} + \begin{bmatrix} \frac{C_{\gamma_f}}{m V_x} & \frac{C_{\gamma_r}}{m V_x} \\ \frac{L_f C_{\gamma_f}}{J} & -\frac{L_r C_{\gamma_r}}{J} \end{bmatrix} \cdot \begin{bmatrix} \gamma_f \\ \gamma_r \end{bmatrix}. \quad (1.30)$$

Chapter 2

Problem definition

First, the camber angle is defined in the **Camber definition** and its dependency on the suspension variables is established in **Camber development**. The models, that determine the behavior of the cambered wheel, are outlined in the **Brush Model - Contact patch development** and **Camber in Pacejka**. These models are then linearized in the section **Linearization of Pacejka Magic Formula** so that they can be utilized in the single track control theory. The **Camber benefits** presents the advantages of the Active Camber Control (ACC) with the framework established by the models. Finally, the **Active Camber Control system design** defines the problem itself and confines it to the vehicle parameters and requirements that construct the boundary conditions of the control problem. These requirements are transformed in the **Actuator requirements** to the model specifications. The section **Approach to the problem solution** describes the approach taken for finding the solution of the problem.

2.1 Camber definition

The camber angle is defined as an angle deviation around the wheel X-axis from its upright position perpendicular to the ground. It can also be specified as an intersection of the wheel axis and perpendicular plane to the ground. See Figure [2.1]. The camber is defined as positive whenever the wheel is inclined from the vehicle and negative when inclined to the vehicle body. The camber angle in Figure [2.1] is positive.

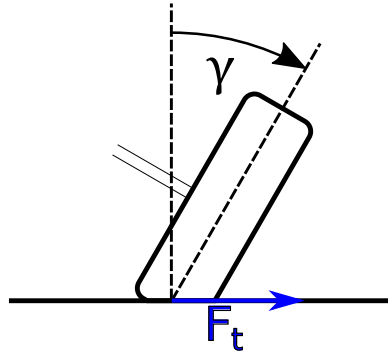


Figure 2.1: The wheel with positive camber angle γ and the lateral blue camber thrust force F_t .

2.2 Camber development

The camber angle is not static. It is constantly changing when the vehicle is in motion. The Figure [2.2] shows the camber gain with the wheel travel. The behavior is very complex. The McPherson suspension has at first negative camber gain on the outer wheel because it cambers the wheel into the corner. The outer wheel is the wheel that is on the outer edge of the corner. However, after reaching a particular value, it continues to positive camber, which is highly undesirable as it cambers the wheel in the wrong direction. The double wishbone has only negative camber with wheel travel because the upper wishbone arm gives another degree of freedom to the suspension, which helps to navigate the wheel in the expected manner. Nevertheless, the extra arm brings disadvantages because it requires more space than McPherson, who does not have any upper arms.

For the purpose of this thesis, the complex behavior shown in Figure [2.2] will be defined with three primary sources, see Figure [2.3] below. However, the behavior will not be entirely captured because it neglects the joint clearance and other factors. On the other hand, it will be precise enough so that the suspension camber angle can be reasonably modeled.

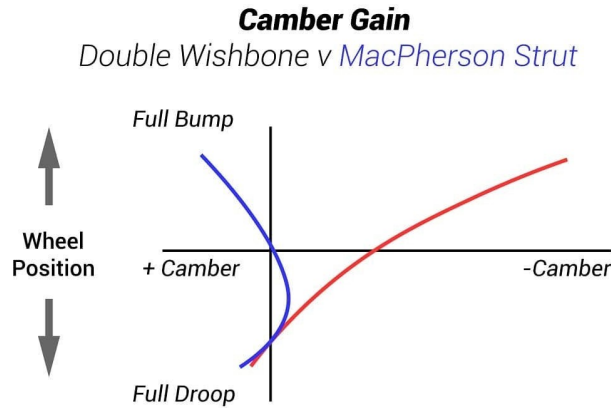


Figure 2.2: The camber gain development based on the wheel travel between the McPherson and double wishbone suspension. The blue line depicts the McPherson and the red line the double wishbone. From: [5]

■ 2.2.1 Camber due to body roll

When the vehicle undergoes a turning maneuver, the sprung mass moves in the opposite direction (Newton 1st law of motion). The suspension has to withstand this motion which leads to change in the linkage formation, which directly induces camber, see Figure [2.3].

■ 2.2.2 Camber due to KPI

When the wheels are steered, the wheels move around the steering axis, creating the camber. The KPI effect on camber is shown in the Figure [2.3]. Moreover, the nominal loads acting on the wheels are also changed, and the outer wheel of the maneuver is overloaded while the inner is unloaded. The spring-dampers thus change in length, which changes the KPI angle and contributes to creating more or less camber respectively. The article [11] provides rule of thumb that $\delta = 10^\circ$ and $KPI = 10^\circ$ creates approximately $|\Delta\gamma| = 0.15^\circ$.

■ 2.2.3 Camber due to Caster

When the wheels are steered, the wheel moves around the steering axis, changing its camber. The more caster angle ϕ , the more camber is being created, see Figure [2.3]. The article [11] provides rule of thumb that $\delta = 10^\circ$

and $\phi = 10^\circ$ creates approximately $|\Delta\gamma| = 2^\circ$. The camber created is almost ten times higher than for the KPI angle. That is why the caster angle is much more important to tend to than the KPI.

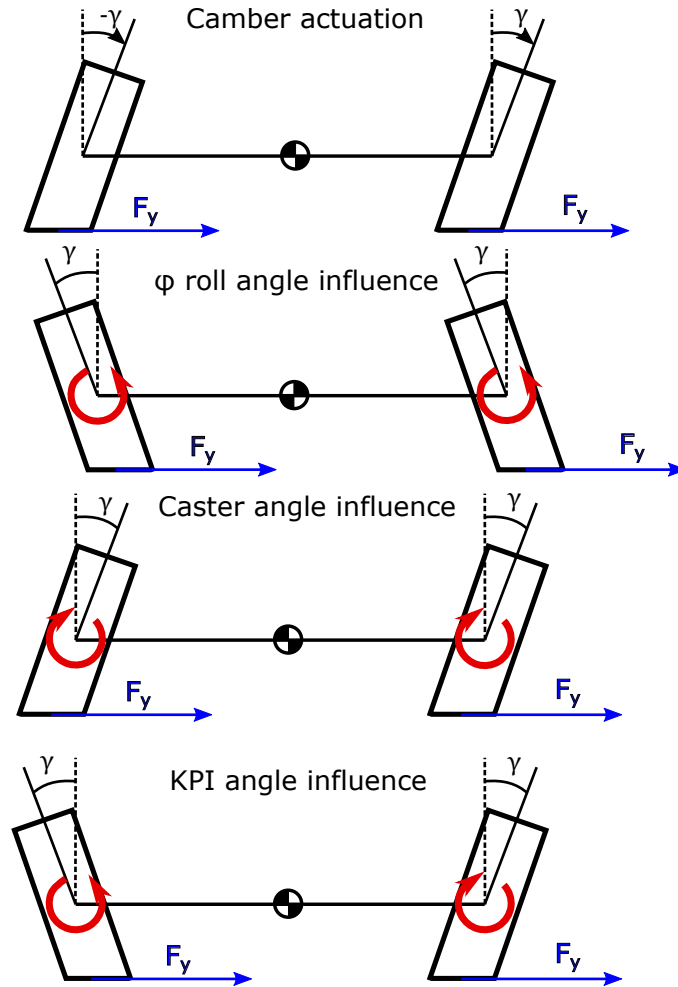


Figure 2.3: The overview of the induced camber from different sources. The top figure shows the desired wheel inclination and the F_y denotes the lateral force of the vehicle in the maneuver, not the camber thrust. The other figures depict the induced camber in the maneuver. Note that the wheels are steered but it is not shown in the diagrams for the simplicity.

2.3 Brush Model - Contact patch development

The understanding of the formulation of forces in the tire is necessary so that the equations of motions for the **Toolboxes** can be calculated. The Brush Model is the physical model of the tire. It is widely used to depict force generation because it uses physics equations and relations that are easier to understand and visualize. The area, which is in contact with the ground, is called a contact patch. It is responsible for generating forces that drive the vehicle. The maximum force that the contact patch can produce is limited by the amount of normal load F_z available times the friction coefficient μ . This creates a boundary called a friction circle that the longitudinal and lateral forces are restricted to stay within, see Figure [2.4].

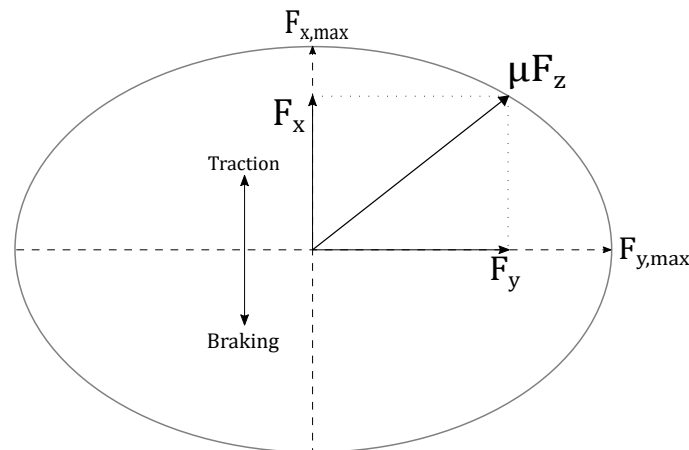


Figure 2.4: The friction circle that defined the maximal longitudinal and lateral forces. The vector sum of F_x and F_y is limited by the μF_z value.

Both F_z and μ are changing throughout the ride, and thus the friction circle is constantly developing. The F_z is generally affected by chassis roll and pitch and change in mass while μ depends mainly on the F_z itself, the temperature, tire material, road, and weather conditions. When the car is not moving, the elements of dF_z are distributed across the contact patch symmetrically around the wheel center, which gives the resultant F_z after integration (the middle picture in [2.5]). When the wheel starts rolling, the distribution is skewed, and the resultant force is off-center. This creates a moment that goes against the wheel motion, and it is called rolling resistance (the left picture in [2.5]). For the sake of simplicity, let's assume that the wheel keeps the symmetric parabolic distribution and define two regions:

adhesion limit and sliding region limit (see the right picture in [2.5]). The adhesion limit corresponds to the maximal force that the wheel can create, and the sliding region limit to the maximal force after the adhesion limit has been reached (see more in **Camber in Pacejka**). Both limits have the same F_z , but they differ in friction coefficient.

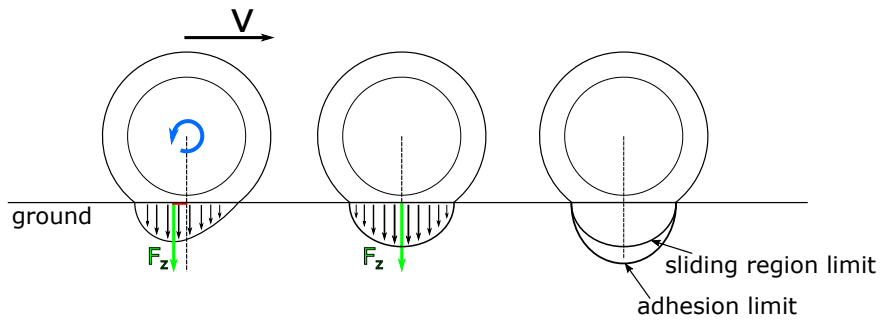


Figure 2.5: On the far left is the real-world normal load distribution throughout the contact patch with blue rolling resistance opposing the motion. In the middle is the parabolic distribution used for the Brush model analysis. On the right side are the adhesion and sliding limits in the accordance to the parabolic distribution. From: [6]

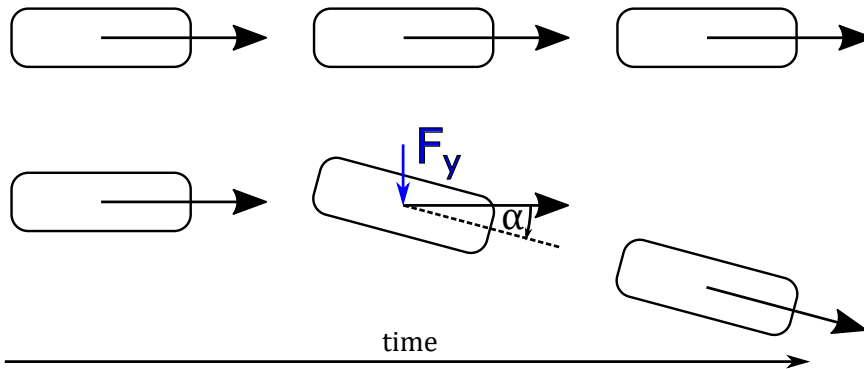


Figure 2.6: The typical behavior of the tire going forward and at a slip angle. The slip angle is create as a reaction to the change in direction and diminishes when the new direction is established.

The classical approach for turning the vehicle is to steer the wheels and thus change the direction of motion. However, this will create a centrifugal force that will oppose the change in the direction. The contact patch is composed of thread elements connected to the ground through the Van-der-Waals bonds and hysteresis effect. In the maneuver, the thread elements are pulled and

stretched, resulting in lateral force F_y that opposes the centrifugal force and turns the vehicle (centripetal force). The slip angle is defined as the angle between the direction of motion and the steered wheel, see Figure [2.6]. It is proportional to the generated lateral force, see left Figure [2.5].

The more sharp maneuver is, the more slip angle is needed to turn the vehicle. This is visualized in the top Figure [2.7], where the increasing of slip angle raises the resultant lateral force, which gradually devours the whole contact patch. The moment the adhesion limit is reached, the threads will slide. Whenever the threads slide, the friction decreases, and the available force drops to the sliding limit.

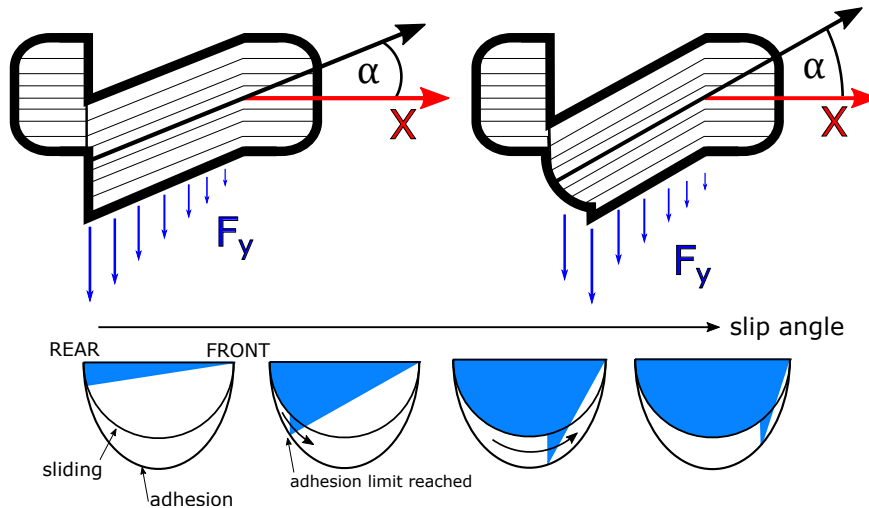


Figure 2.7: The top figure is the Brush Model of the tire for the slip angle with depicted side force F_y . On the bottom is the lateral force development cycle for increasing slip angle. The adhesion peak travels from the back to the front as it fills the sliding region. From: [6]

Another approach is to camber the wheel and turn without the need to steer. The force developed from the camber angle is called camber thrust. The camber thrust is created from the deformation of rubber where the thread elements are forced to move to where the wheel is inclined to, which creates lateral force. See top Figure [2.8].

The higher the camber angle is, the more lateral force is created till a physical limit is reached. The camber angle uses the shape of the contact patch more efficiently and reaches the adhesion limit on the whole area simultaneously. It does not lose any available force to the unnecessary sliding. In bottom figure of [2.8], the process is visualized. However, some remarks

have to be made. The parabolic distribution does not accurately estimate the contact patch in the real vehicle, as discussed in Figure [2.5]. Also, the process in [2.7] is described for zero effective slip angle, which would be impossible. Nevertheless, the benefits of the camber are undeniable, see section **Camber benefits**.

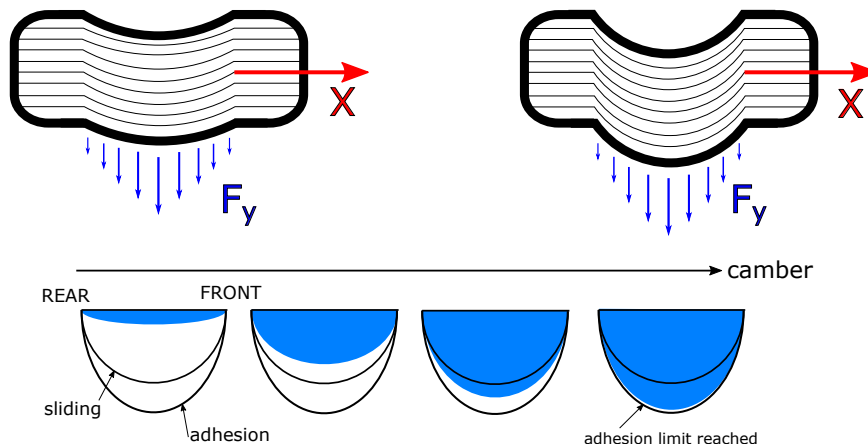


Figure 2.8: The top figure is the Brush Model of the tire for the camber angle with depicted side force F_y . On the bottom is the lateral force development cycle for increasing camber angle. The adhesion peak is reached at the same time through-out the contact patch. From: [6]

2.4 Camber in Pacejka

The Brush Model presents a respectable illustration for understanding the physics of the force generation. However, it assumes and neglects many features that make it inaccurate, see, for example, Figure [2.5]. Hans B. Pacejka created a semi-empirical Magic Formula that predicts longitudinal and lateral forces as well as the aligning moment in the contact patch. It is very accurate as the force is estimated by a formula created from the best fit to the experimental data. That is why it was used in the twin track vehicle model in the **Toolboxes**. The formulation for lateral force is as follows:

$$F_y = F_z D \sin(C \arctan(B \alpha - E (B \alpha - \arctan(B \alpha)))). \quad (2.1)$$

It depends directly on the slip angle α and uses C, E, B as shape factors and D and F_z to scale the curve. The typical curve can be seen in Figure [2.9].

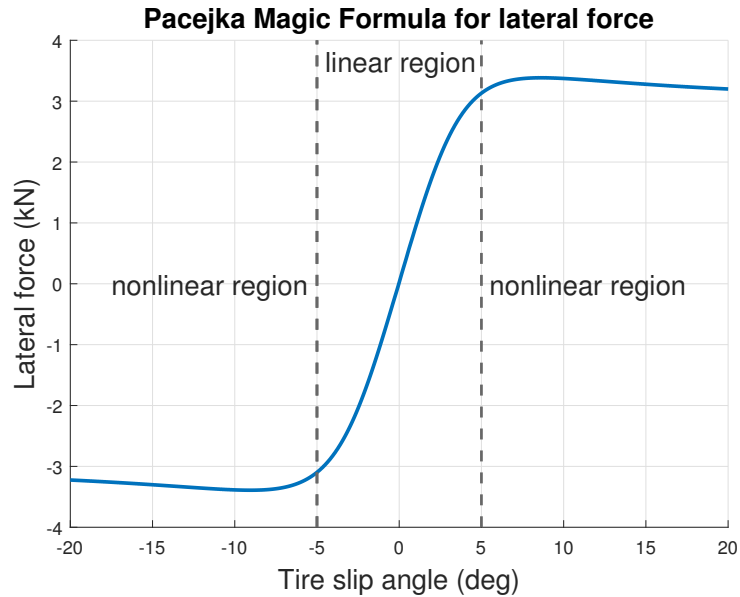


Figure 2.9: The lateral force of the Magic Formula in (2.1) across different tire slip angles.

The C , E , B , D factors in the equation (2.1) are themselves dependent on other variables like normal load, camber or road friction and they are clearly defined in the Pacejka book [21] in equations (4.E9)-(4.E78).

The characteristic shape of the curve can be divided into linear and nonlinear regions. In the linear region, the traction force increases with the slip angle. However, when the maximum value is reached, the force decreases in value. This region is regarded as nonlinear and represents complete sliding or loss of control.

The part of the tire, which is in contact with the ground, is made out of rubber. This material is viscoelastic. See Figure [2.10]. As the tire is in contact with the ground, bonds are created between the surface and the rubber. The strength of these bonds is depicted here as the loss factor. In other words, the loss factor is proportional to the amount of energy the material can create. The energy is used to oppose the centrifugal forces of the vehicle while cornering. That is why the loss factor is regarded as the friction coefficient and normalized to number 1 (see left Y-axis of figure [2.10]). Nevertheless, the normalized value of 1 also depends on the state of the road. The dry road has a value of 1, while the wet and ice/snow road have 0.8 and 0.3, respectively.

The tire moves mainly between the viscoelastic and highly elastic rubber

states because the wheels are stressed and warmed up while in motion. The glassy state is visited only when the vehicle is at the complete stop. The viscoelastic and highly elastic rubber states can be approximated by two different friction coefficients. The viscoelastic friction coefficient is called "adhesion limit", and the highly elastic rubber is the "slide region limit". See more in **Brush Model - Contact patch development**.

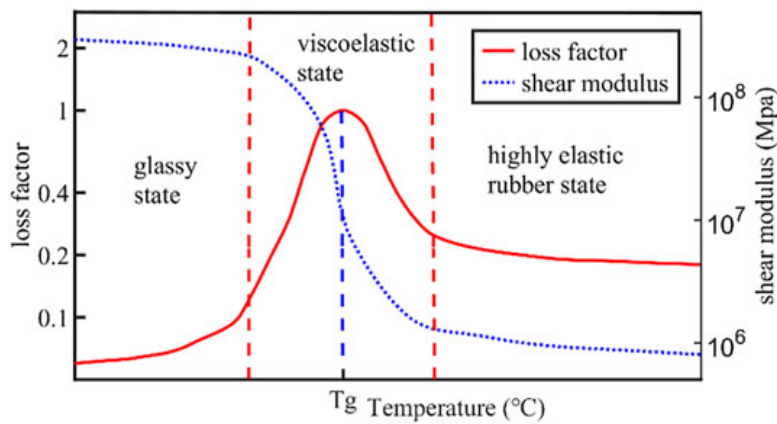


Figure 2.10: The dependency of loss factor of different states of rubber on the temperature. The amount of stress (energy), it can withstand, is directly related to the friction coefficient in tires. From: [7]

The peak in the viscoelastic state corresponds directly to the maximum value of the Pacejka Magic Formula curve. As the resultant force gradually consumes the contact patch, the temperature increases, and thus the friction coefficient decreases and the maximum force too.

The effect of camber on the lateral force Pacejka Magic Formula can be seen in Figure [2.11]. It is mirrored for the negative camber and negative slip angle. The camber thrust is less than the forces generated by slip angle but not insignificant. The camber increases generated force in the linear region but disappears around the curve peak when the contact patch is completely devoured by the resultant force, see Figure [2.11]. Also, the higher the tire slip angle is, the less camber thrust is generated. This supports findings from **Brush Model - Contact patch development** where the camber thrust is highest when there is a zero effective slip angle.

Moreover, the tires have an optimal camber angle that is dependent on the normal load where the lateral force is maximized. When the vehicle turns, its body rolls and changes the normal load on the tires. Thus, the normal load is distributed unevenly between the right and left sides of the contact patch,

where one side is more loaded than the other. That is why there exists an optimal camber angle which would incline the wheel in such a way that the normal load is evenly distributed and thus the force is maximized. This is not captured in the Mathworks model and thus cannot be visualized.

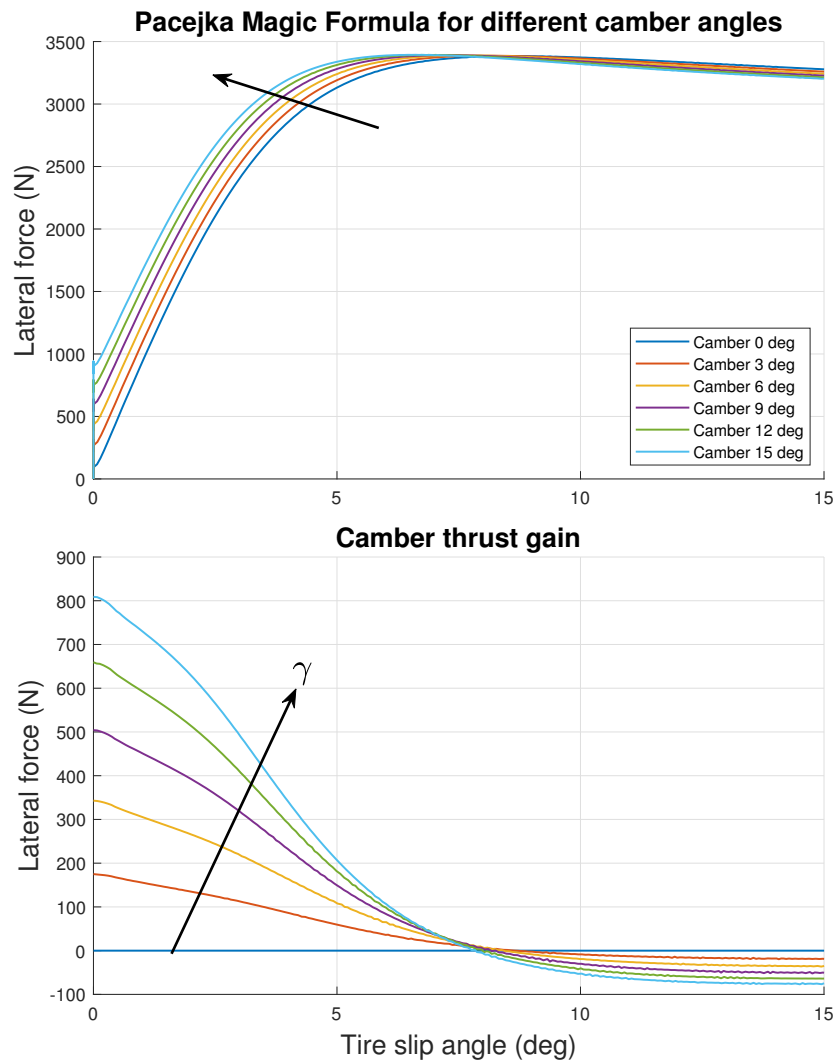


Figure 2.11: The lateral force of the Magic Formula across different camber angles. The peak force value does not change. On the other hand, the force can be generated with no slip angle. The camber thrust diminishes at the force peak. The bottom figure shows only the force gained from the camber thrust.

The friction circle is also affected by the camber angle. It is prolonged

and shifted in the lateral force direction, and squished in the longitudinal direction. Thus, the more of the camber angle is used, the less longitudinal force can be generated, see **Friction circle development with camber**. Nevertheless, the reduction in the maximal longitudinal force does not need to be the same as the gain in the lateral force.

2.5 Friction circle development with camber

The friction circle shape cannot be actively changed in conventional cars, which limits the ESP and ABS effectiveness. However, the camber angle can do just that. The friction circle in Figure [2.12] is created from the conjunction of the multiple simulated maneuvers. The largest euclidean norm then represents the maximal force achieved, which is then used for the friction circle estimation as an ellipse, see Figure [2.12]. Whenever the camber angle is induced, the friction circle is squished in the longitudinal force direction and prolonged and shifted in the lateral force direction, see Figure [2.13]. The Figure [2.14] shows the zoomed part of the friction circle edges. The lateral force gain is almost 4x higher than the longitudinal force loss.

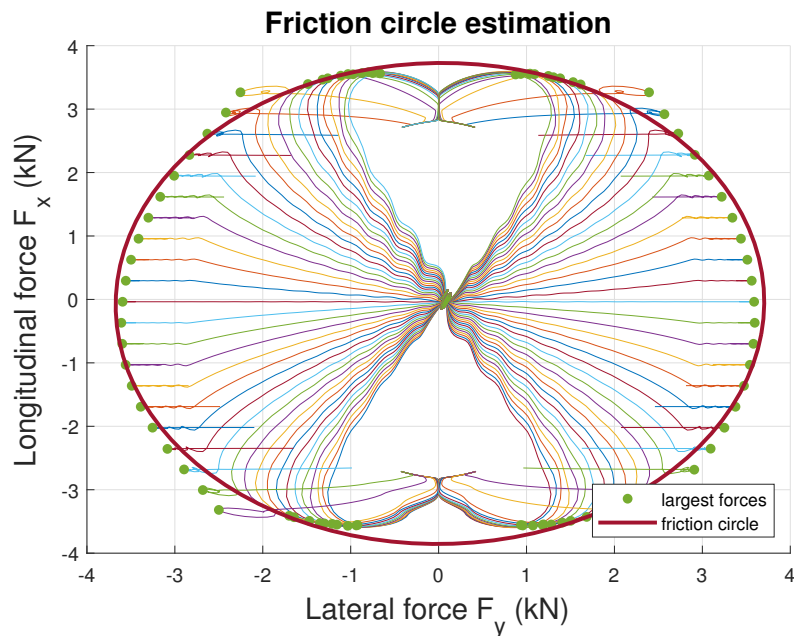


Figure 2.12: Friction circle estimation as an ellipse from the complex Pacejka Magic Formula model from Matlab. The points with the highest euclidean norm are used for the estimation.

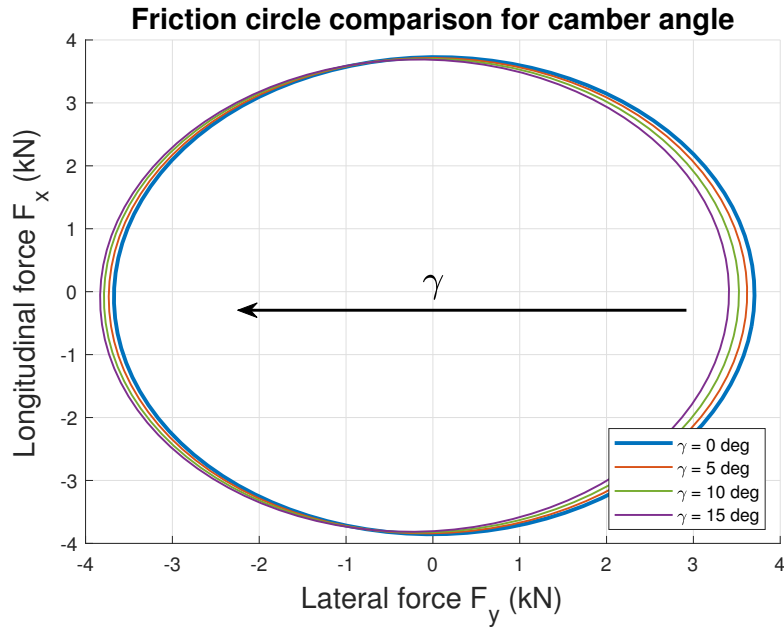


Figure 2.13: The comparison of the friction circles with different camber angles. The shifting of the friction circle is marked by an arrow.

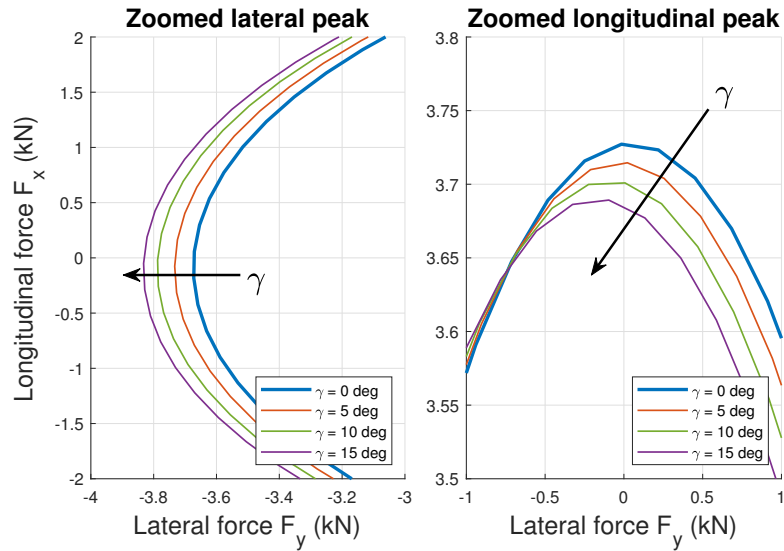


Figure 2.14: The lateral and longitudinal force peak movement zoomed from Figure [2.13]. The gain in the lateral force is almost 4x higher than the loss in the longitudinal force.

2.6 Linearization of Pacejka Magic Formula

The Pacejka Magic Formula model is nonlinear and thus cannot be used for the linear models like **Single track mathematical model**, but it can be approximated for small slip angles where the force gain from slip and camber can be decoupled. Figure [2.11] shows that the camber thrust slowly disappears as the slip angle increases. Thus, the camber thrust can be approximated as linear till a particular slip angle value is reached. This method was used by many researchers, including in [17] but the saturation by particular slip angle value makes it still nonlinear. Nevertheless, if the operating point of the linear model is chosen to be at 0 slip angle, the saturation can be ignored, and the force formula can be decoupled with:

$$F_y = C_\alpha \alpha + C_\gamma \gamma. \quad (2.2)$$

2.6.1 Linearization of slip angle

The characteristic shape of the Pacejka curve in Figure [2.4] can be approximated linearly around zero for small slip angles as

$$F = C_\alpha \alpha \quad (2.3)$$

where C_α is defined as a slope of the curve around 0 slip angle, see Figure [2.15]. The top Figure shows the linear approximation of the Pacejka curve. The gradient of the top Figure [2.15] is shown at the bottom. The value of the cornering stiffness is at the zero slip angle. Note that the cornering stiffness model is applicable only around the zero slip angle.

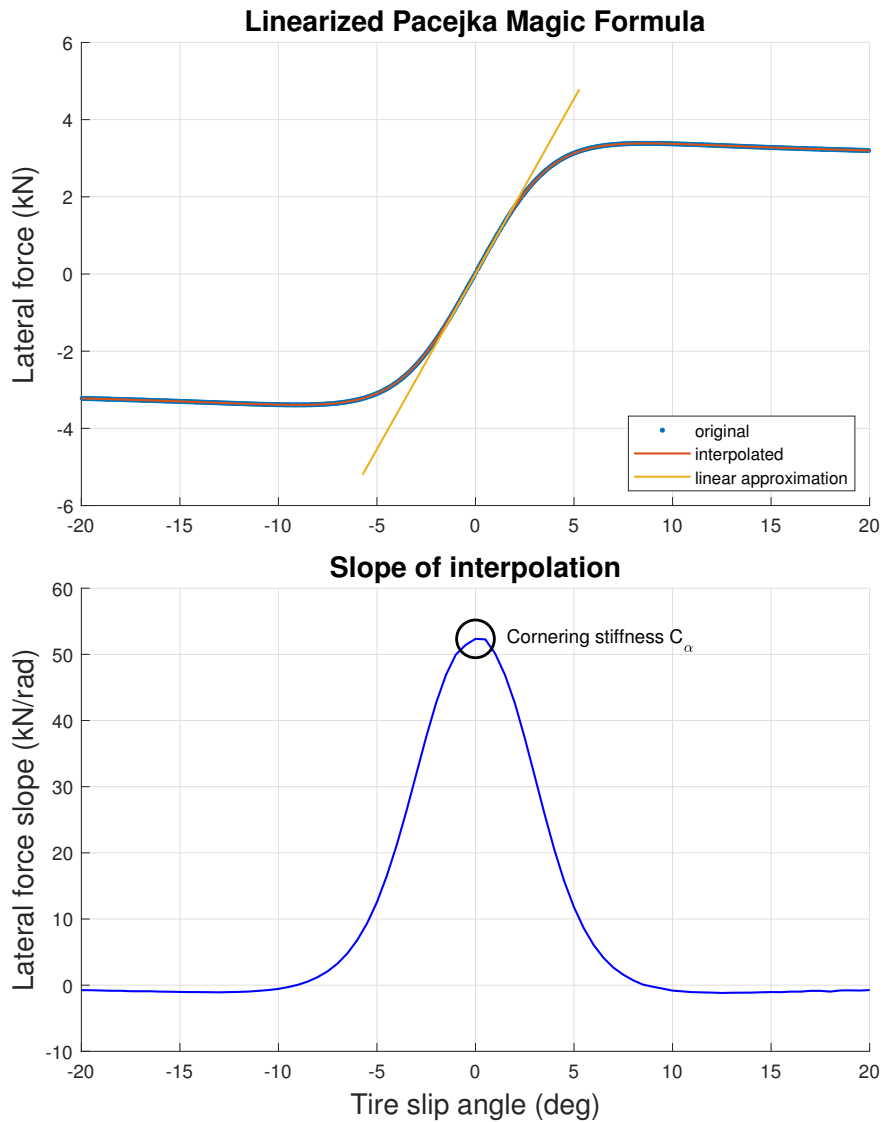


Figure 2.15: The linearization of the Pacejka Magic Formula from the gradient of the curve around zero. The value of the slope at zero slip angle is the cornering stiffness.

2.6.2 Linearization of camber angle

The camber thrust can be approximated similarly to the slip angle as:

$$F = C_\gamma \gamma. \quad (2.4)$$

However, the cambering stiffness C_γ is calculated as the average across all camber thrusts at zero slip angle. Figure [2.16] shows the camber thrusts where the estimations are shown as the dashed lines. The cambering stiffness model is also applicable only around the zero slip angle.

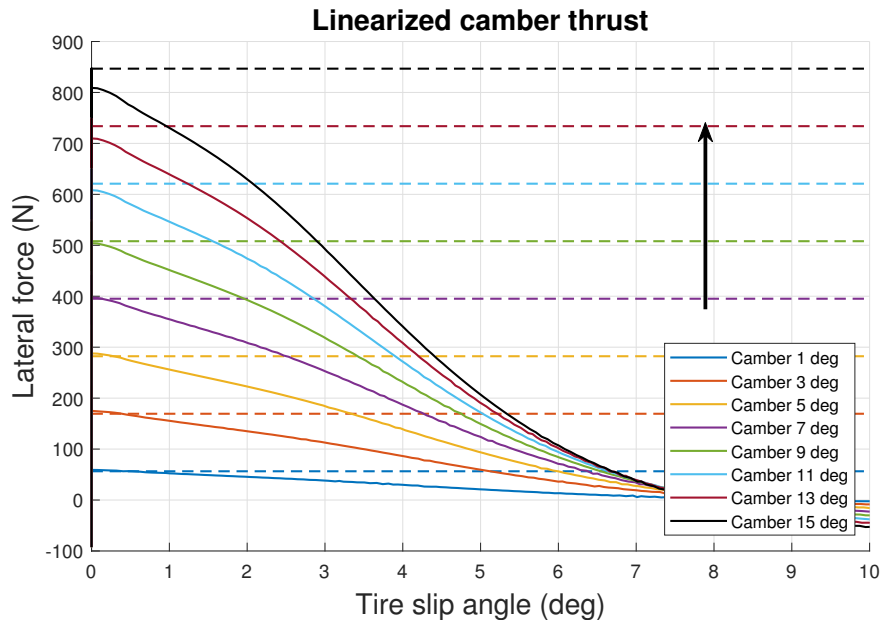


Figure 2.16: The linearization of the Pacejka Magic Formula for the camber thrust. The average of all the camber thrust values at 0 slip angle is the cambering stiffness. The estimation of the camber thrust by cambering stiffness is depicted as the dashed lines for the particular camber angles.

2.7 Camber benefits

2.7.1 Cornering losses

The conventional cars use the wheel sideslip angle to compensate the cornering forces. However, the slip angles create cornering resistance force F_c that consumes energy [18]. The power consumed can be calculated as:

$$P = \frac{W}{t} = \frac{F_c s}{t} = F_c v_x = (F_{cf} + F_{cr})v_x, \quad (2.5)$$

where F_{cf} and F_{cr} are components of the cornering resistance in the front and rear respectively. The cornering resistance depends on the lateral forces

and slip angles, see Figure [2.17]:

$$F_{cf} = \sin(\alpha_f)F_{yf} \approx \alpha_f F_{yf}, \quad (2.6)$$

$$F_{cr} = \sin(\alpha_r)F_{yr} \approx \alpha_r F_{yr}. \quad (2.7)$$

The lateral forces can be further approximated by cornering stiffness yielding:

$$P = F_c v_x = (C_{\alpha_f} \alpha_f^2 + C_{\alpha_r} \alpha_r^2) v_x, \quad (2.8)$$

where one can see that the energy lost is proportional to the square of the tire slip angle α . To save more energy and increase performance, the camber actuation is very attractive. The active camber actuation reduces the magnitude of the slip angles because the resultant lateral force is achieved at smaller slip values and does not produce any losses in the process.

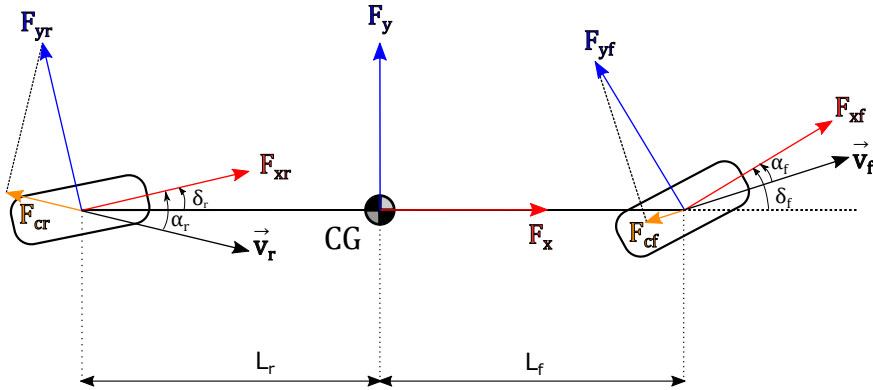


Figure 2.17: The single track model with depicted cornering resistance forces F_{cf} and F_{cr} .

2.7.2 Camber for faster lateral force generation

The camber can also generate lateral force faster from steering input. In the top of Figure [2.18] is the lateral force response to the steering input for the general conventional car without the camber control. The lateral force increases till the vehicle skids. The maximum force is reached around 2 seconds. The curve can be considered linear up to 1 second where the camber thrust will have an additive effect as discussed in section **Linearization of Pacejka Magic Formula**, see Figure [2.11]. If the camber reaches $\Delta\gamma = 30^\circ/\text{s}$ actuation speed, the generated lateral force will be increased in the linear region as shown in the bottom Figure [2.18]. For example, the vehicle needs $F_y = 2500\text{ N}$ to pass around a corner. In the Figure [2.18], the

car with the conventional steering system requires 0.8s to acquire enough force but the cambered wheel is able to realize the same value in 0.5s which is almost 2 times faster.

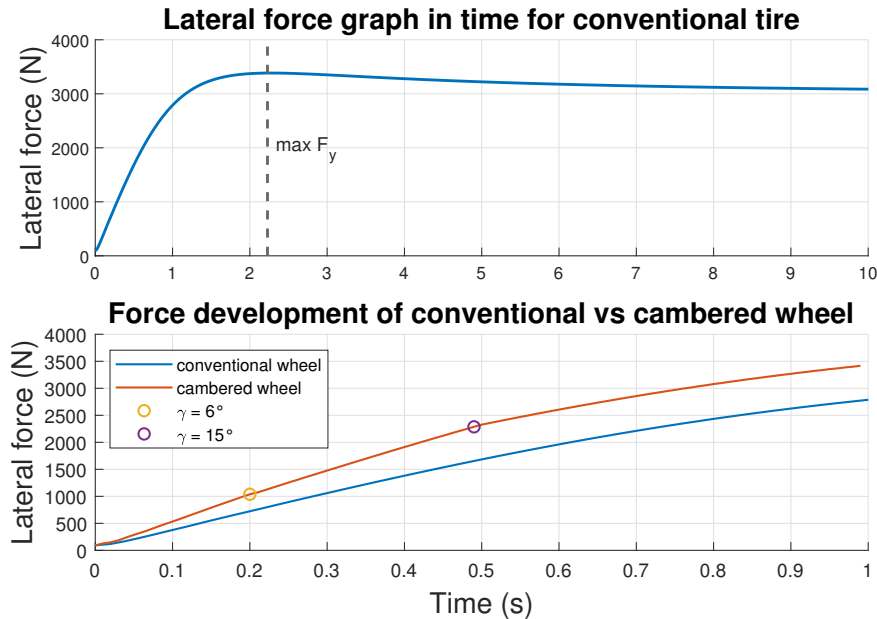


Figure 2.18: In the top figure is the lateral force response for the steering input. The peak is reached around 2 seconds so upto 1 second can be the curve considered linear. In the bottom is comparison of the force response between the conventional and the cambered wheel that uses $\Delta\gamma = 30^\circ/\text{s}$. The camber is saturated at $\gamma_{max} = 15^\circ$.

2.7.3 Line Of Peaks problem

The Line Of Peaks defines a phenomenon where the lateral force peak moves with respect to the tire sideslip angles when subjected to different wheel normal forces when the car body rolls around its X-axis. The shift is shown in Figure [2.19]. The peak does not move vertically as it would be assumed but rather diagonally, which changes the position of the peak force. This effect is highly undesirable because when the normal load increases, the peak is moved to the higher slip angles, which increases the tire wear and the magnitude of tire sideslip angles needed to reach the higher lateral forces.

On the other hand, the camber moves the peak almost horizontally. Thus, it can be used to mitigate the Line Of Peaks phenomenon and keep the peak stable on the referenced slip angle. The amount of camber angle needed to

accomplish this is around -5° to 5° for conventional car tires based on the Figure [2.19].

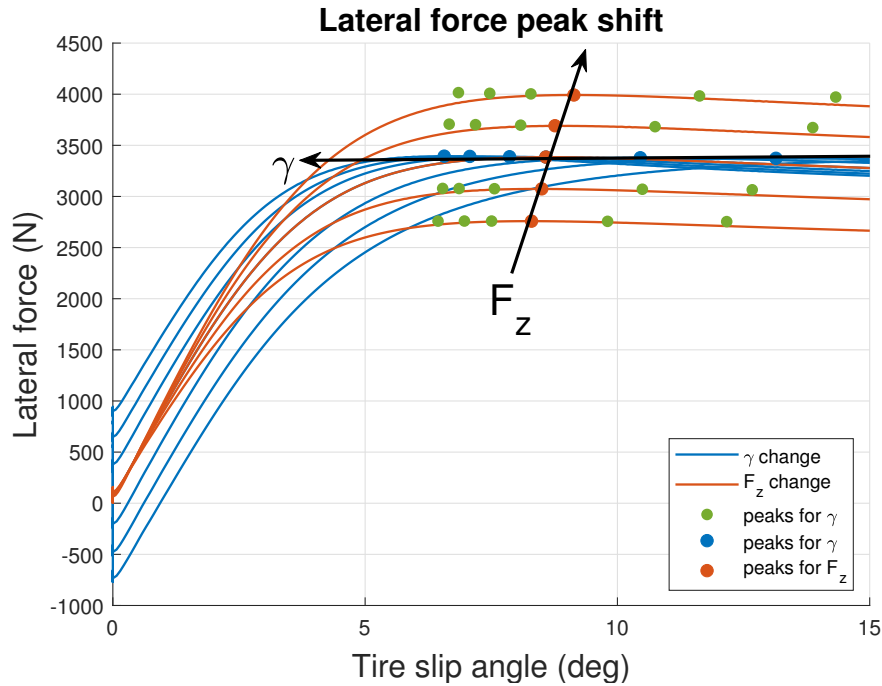


Figure 2.19: The lateral force peak moves differently for given normal loads and camber angles. The camber angle moves peak almost horizontally while the normal load moves it diagonally. The arrows show the change for increasing γ and F_z values. The camber is changed from -15° to 15° and normal load from 80% to 120%. The green points show the peak movement for other than the nominal F_z and their curves are not shown for the simplicity.

2.7.4 Usage diversity of camber angle

The configuration of the front and rear camber angles can create either the side force F_y or the yaw rate torque M_z , see Figure [2.20]. The side force can be used for Double Lane Change (DLC) maneuvers. On the other hand, the yaw rate torque can be used for extreme maneuverability at low speeds or very sharp corners. However, creating a yaw rate torque with rear wheels cambered out of the corner could be potentially dangerous and unsafe because it can decrease the contact patch area at high speeds. There was not found much research regarding this fact, and further testing will be needed. This thesis will not make any restrictions for camber angles regarding this phenomenon.

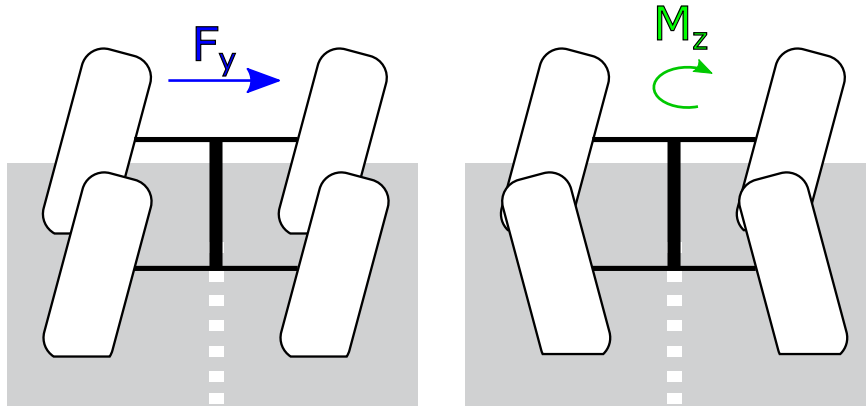


Figure 2.20: Two different camber configurations. The left figure generates side force F_y while the right figure creates the yaw rate torque M_z .

2.8 Active Camber Control system design

The CTU is developing a new demonstrator vehicle. In these sections, the Active Camber Control will be defined from the control system design perspective with regard to the measured variables and goals. The IO diagram of the CTU demonstrator for this particular problem is shown in Figure [2.21]. The control law should be designed in such a way that it depends on the steering input from the driver. That is why the steering angles are outputs and not inputs to the system. The diagram very closely mimics the twin track model shown in [1.11]. However, the suspension outputs L_s , η and d are also added. The suspension is modeled separately as its dynamics are very delicate and hard to describe with the differential equations. Thus, the suspension is created in Simscape that constructs them automatically, see **Simscape model of suspension**.

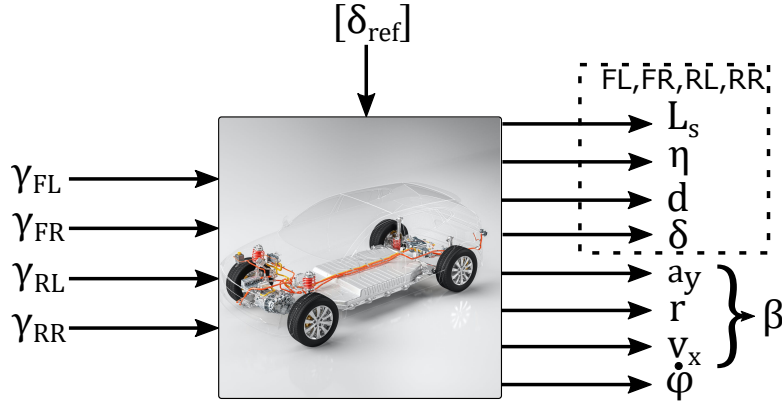


Figure 2.21: The input and output diagram of the CTU demonstrator vehicle. The side slip angle β is estimated. The $[\delta_{ref}]$ marks the vector of 4 referenced steering angles from the driver or other control system. The vehicle picture from: [8].

2.8.1 Controlled variables

The control variables are the system inputs that actuators can change to alter the system behavior. Due to the topic of this thesis, the camber angle is the actuated variable. Each wheel has its own actuator that can be independently controlled, see Figure [2.21]. For example, the FL stands for front-left and the RR for rear-right. Note that the actuators have to be administered as well so that the particular camber angles will be realized.

2.8.2 Measured variables

The measured variables are the system outputs that the control algorithm can observe to get information about the system state. The number and type of the measured variables are chosen on purpose so that all can be obtained with the obtainable equipment and have low SNR (Signal-to-noise-ratio). The control algorithm is thus realizable in real-world applications.

The first four variables are measured for each wheel. The L_s is the length of the spring-damper strut. The d is the stroke length of the amber actuator, and it is directly taken as an output from its actuator interface. The η defines the angle of the lower control arm to the wheelbase of the vehicle, see Figure [2.22]. The sensor is already used in many cars. It is the Xenon Level Sensor used to level the front lights with the road. The δ_{ref} are the steering angles obtained from the driver steering input and the δ are the steering angles of the vehicle. The $\dot{\phi}$, a_y , and r are the roll rate, lateral acceleration, and

yaw rate, which are obtainable from the MEMS accelerometer and gyroscope, respectively. The sideslip angle β cannot be measured directly and thus has to be estimated. It can be calculated as:

$$\beta = \int \left(\frac{a_y}{v_x} - r \right) dt, \quad (2.9)$$

where v_x is the longitudinal velocity of the vehicle. Nevertheless, it can be estimated through any other means, and many publications are focusing solely on this topic, see [23] or [24].

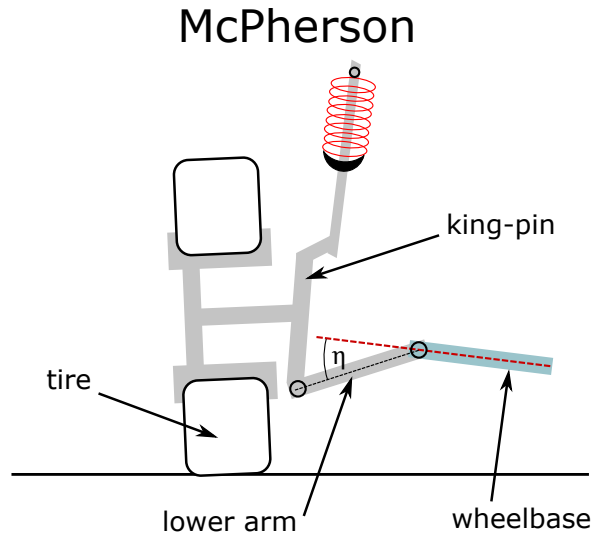


Figure 2.22: The diagram defining the η angle for the McPherson suspension. It is the angle between the wheelbase and the lower control arm.

2.8.3 Parameters and control requirements

The car parameters are assembled from the CTU demonstrator vehicle and its list is shown in the table [2.1] below.

Table 2.1: CTU demonstrator vehicle parameter list

Symbol	Value	Units	Definition
L_1	38	cm	length of the lower control arm
L_{2SA}	26.5	cm	length of king-pin + ball joint in the SA

Symbol	Value	Units	Definition
L_{sSA}	45	cm	length of the McPherson strut measured in the SA
L_w	11.5	cm	length between the wheel axle in the king-pin and the ball joint center
L_{shf}	9	cm	distance of the McPherson strut closest point to the king-pin projected onto the lower arm
σ_{shf}	2	<i>deg</i>	angle of the McPherson strut from the king-pin
ϕ_f	2	<i>deg</i>	caster angle at the front suspension
ϕ_r	0	<i>deg</i>	caster angle at the rear suspension
k_f	55	N/mm	front spring constant
k_r	50	N/mm	rear spring constant
L_{s_n}	44	cm	spring natural length
c	3	N/mm/s	damping coefficient
g	9.81	m/s ²	gravitational acceleration
m	1500	kg	vehicle mass
Tire	R18 205/45	tire type	
R_o	32.15	cm	unloaded tire radius
R_i	23.05	cm	rim radius
T_w	20.5	cm	tire width
L_f	1.231	m	longitudinal distance of the CG from the front axle
L_r	1.231	m	longitudinal distance of the CG from the rear axle
w_f	0.71	m	lateral distance of the CG from the vehicle side at the front axle
w_r	0.705	m	lateral distance of the CG from the vehicle side at the rear axle
h_{CG}	0.44	m	height of the center of gravity
P_M	95	kW	motor power on each wheel

Symbol	Value	Units	Definition
T_{max}	220	N m	maximal torque of the motor
G_r	11.2	–	gear ratio
τ	0.01	s	motor time constant
I_{xx}	400	kg m ²	moment of inertia around the CG X axis
I_{yy}	1700	kg m ²	moment of inertia around the CG Y axis
I_{zz}	1900	kg m ²	moment of inertia around the CG X axis
C_f	52.01	kN/°	front cornering stiffness for one wheel
C_r	52.01	kN/°	rear cornering stiffness for one wheel
C_{γ_f}	3.234	kN/°	front camber cornering stiffness for one wheel
C_{γ_r}	3.234	kN/°	rear camber cornering stiffness for one wheel

The cornering stiffness C_{α_f} and C_{α_r} is calculated based on the **Linearization of slip angle** and the camber cornering stiffness C_{γ_f} and C_{γ_r} is based on the **Linearization of camber angle** from the Mathworks tire model of complex Pacejka Magic Formula with tire parameters from table [2.1]. The caster angles are intentionally chosen small so that the independent steering for each wheel does not require strong actuators as discussed in **Suspension terms**. The car is thought to be neutral-steer, thus the $L_f = L_r$. The mass distribution on the front and rear is very similar due to the battery, motors, and gearbox positions on the vehicle chassis. However, the CG position changes whenever the vehicle is loaded or unloaded by passengers or cargo. Moreover, there exist other condition changes like road profile, weight distribution, or velocity. All of these variations establish the boundary conditions which make up the vehicle requirements. The boundary conditions are:

1. Load variation up to 20 %.
2. CG position change up to 15 cm to the front or rear from the center (around 5 % on each side).
3. Road profiles: dry, wet, ice/snow.
4. Velocity up to 150 km/h.
5. Spring and damper coefficient variation up to 10 %

The road profiles are represented by friction coefficient changes, see **Camber in Pacejka**. In conjunction, the vehicle must withstand a defined wind gust that can exert side force or angular moment on the car. Moreover, the vehicle is expected to be outdoor tested with the lateral acceleration up to $a_{y_{max}} = 1 g$. The control system has to be also robust to abrupt changes in the system parameters like length of lower arm L_1 . The controller stability margins have to be at least $PM \geq 45^\circ$ for phase margin and gain margin $GM \geq 6 dB$ which are default conditions in almost any applications that use controllers.

2.9 Active camber actuation point

There are multiple ways how to actuate camber in the suspension but generally they can be separated into three types:

1. Lower arm extension
2. Upper mounting point displacement
3. Adjustment of the king-pin

The article [3] provides a well-thought-out overview and comparison of the already published systems, see Figure [1.7]. Any adjustments for the camber actuation inside the wheel hub and king-pin will require sizable structural modifications because of the small space. That will be costly and require high power actuation due to the larger unsprung weight. The lower arm extension also needs a high-power actuation system because the actuator will have to drag the wheel across the surface. The upper mounting point displacement demands the least power but requires more displacement to achieve the same camber angle as the other two proposals. However, it does not increase the unsprung mass, and no modifications of the McPherson suspension parts are needed. That is why it was chosen as this thesis approach for the camber actuation.

The McPherson strut mounting point is augmented so that it can move along a rail where the actuator controls its movement, see **Simscape model of suspension**. This calls for a controller that will regulate the stroke length of the actuator to achieve the particular camber angles. The actuator also has to produce enough forces to actuate the camber angle fast enough and withstand the ones it is subjected to.

2.10 Actuator requirements

The actuator has to be fast enough to react to the changes in the vehicle states. This calls for the actuator's rate of change estimation, which can be used in the single and twin track model to develop control algorithms. The most prevalent modes are:

1. **Body roll due to road bumps**
2. **Body pitch due to road bumps**
3. **Longitudinal and Lateral force development**

The actuator rate of change is governed by the μ_{rate} and its identification is shown in section **Slew rate identification** below.

2.10.1 Body roll due to road bumps

Whenever one side of the car drives over a bump, the body will roll in response. The actuator has to be fast enough to regulate such disturbance. To determine the frequency of the model response, the model of the car suspension in Simscape is used, see **Simscape model of suspension**. The model represents the McPherson suspension as is shown in Figure [1.9]. The model is linearized from the piston position h_R to the roll angle φ of the body mass center (red square). The subsequent step response is in Figure [2.23].

The step response closely resembles a 2nd degree system which has transfer function:

$$H(s) = \frac{\omega_n^2}{s^2 + 2\zeta\omega_n s + \omega_n^2} \quad (2.10)$$

The damping ratio ζ and natural angular frequency ω_n are determined by equations:

$$\zeta = \frac{-\ln(OS/100)}{\sqrt{\pi^2 + \ln(OS/100)^2}} \quad (2.11)$$

$$\omega_n \approx \frac{4}{T_s \zeta} \quad (2.12)$$

where $OS = 12.5\%$ is the overshoot percentage and $T_s = 0.1$ s the settling time which can be read from the step response [2.23]. Thus, the damped frequency of the mode equates to:

$$f_d = \frac{1}{2\pi} \omega_n \sqrt{1 - \zeta^2} = 9.62 \text{ Hz.} \quad (2.13)$$

with damping coefficient $c = 3000 \text{ N/m/s}$ and spring constant $k = 55\,000 \text{ N/m}$.

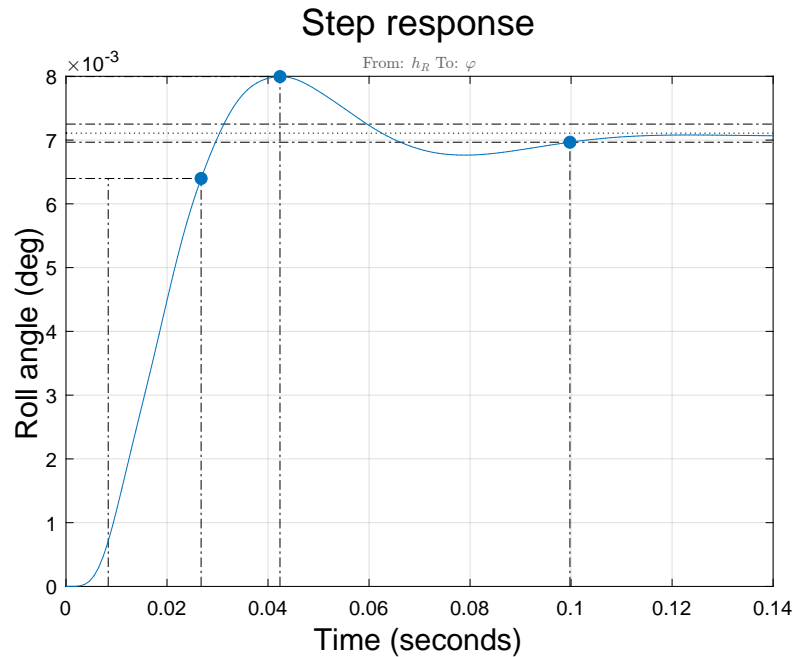


Figure 2.23: Step response of the linearized system from the piston position to the body roll in [1.9].

2.10.2 Body pitch due to road bumps

The actuator also has to be able to compensate for on-axle weight changes that can be excited, for example, by driving over the speed-breakers, acceleration, or deceleration. The system response is typically in the range between 1-2 Hz, taken from [25].

2.10.3 Longitudinal and Lateral force development

The wheel relaxation phenomenon gives the number of wheel rotations needed for the forces to fully develop at the contact patch. The number of rotations is typically between 1-2 depending on the wheel speed.

If the car top speed is $v_{max} = 150 \text{ km/h} \approx 40 \text{ m/s}$ and the wheel formulates forces in one and a half rotations, the frequency of the response is:

$$\omega = \frac{1}{1.5} \frac{v_{max}}{R_0}, \quad (2.14)$$

$$f = \frac{\omega}{2\pi} \approx 15 \text{ Hz} \quad (2.15)$$

where $R_0 = 0.3215$ m is the radius of the undeformed wheel from table [2.1]. Note that the precise frequency for the lateral force would be smaller because it also depends on the steering speed. However, the CTU demonstrator steering speed is not known. The typical frequency for the development of lateral force in the conventional car with driver could be up to $f = 2$ Hz for $a_y = 0.4g$ taken from [26]. The main purpose of the active camber is to act and react to the lateral acceleration, not to the longitudinal. That is why the frequency for the lateral force development is taken to be

$$f = 2 \text{ Hz}. \quad (2.16)$$

■ 2.10.4 Slew rate identification

The actuator should be fast enough to react to all frequencies. The required velocity of the actuation can be calculated as the slew rate limitation. The slew rate μ_{rate} is defined as the maximal change in value per second. The amplitude of the final value is set to one because the 1° of camber angle is deemed sufficient to compensate for most of the parasitic effects, see [16] for the typical ranges. Thus, the unit-step value input would be achieved in $1/\mu_{rate}$ seconds.

However, the actuators are hardly ever approximated with slew rate, and more often than not, they are approximated with low-pass filters. The higher frequencies are damped as the device is unable to react fast enough to the input. Moreover, the dynamics of the low-pass filter are linear and thus suitable to use in the Linear System Control design. The transfer function for low-pass filter is:

$$H(s) = \frac{1}{\tau s + 1}, \quad (2.17)$$

where the τ is the system time constant and relates to the speed of the system response. In other words, the τ is the duration that the signal needs to reach its final value with the slew rate μ_{rate} , see Figure [2.24].

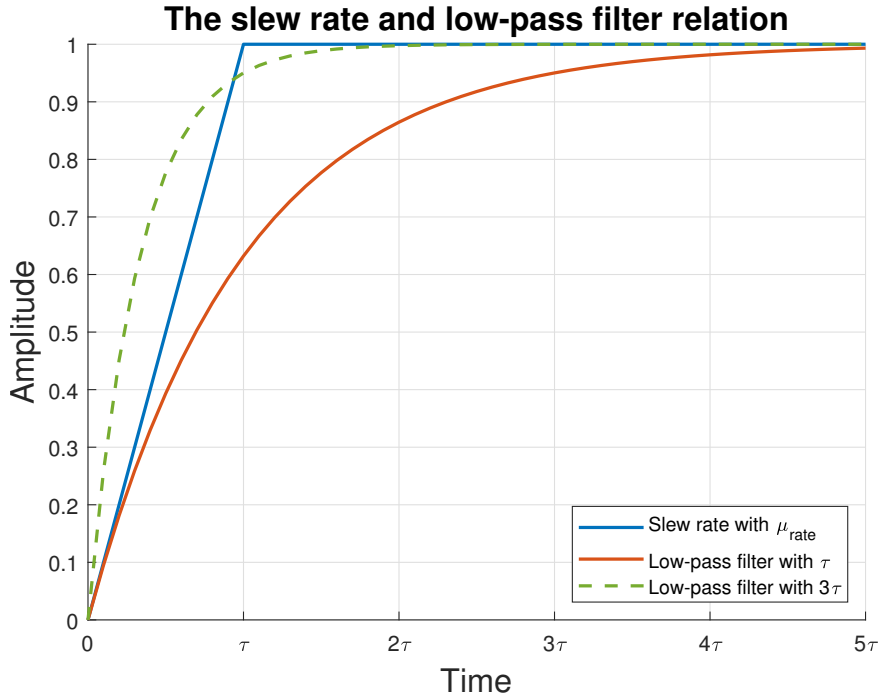


Figure 2.24: The slew rate to low-pass filter relation.

In time $T = \tau$, the response of the low-pass filter reaches 63% of its final value. For $T = 3\tau$ the response reaches 95% which is deemed sufficient. The time (period) is related to frequency by:

$$f = \frac{1}{T} = \frac{1}{3\tau} = \frac{\mu_{rate}}{3}, \quad (2.18)$$

and to the slew rate parameter as $\mu_{rate} = 1/\tau$ because the actuator would reach the final value in time τ if it had actuation speed μ_{rate} . The maximal frequency found is:

$$f_{max} = \max(9.62, 2, 2) \text{ Hz}, \quad (2.19)$$

$$(2.20)$$

where the frequency of the **Longitudinal and Lateral force development** is only for the lateral acceleration attribute. Thus, the required actuation speed is:

$$v_{req} = \mu_{rate} = 3 f_{max} = 29^\circ/\text{s}. \quad (2.21)$$

2.11 Approach to the problem solution

This thesis tackles the assembling of the active suspension control system in two main parts that are represented in **chapter 3** and **chapter 4**.

The actuator has to be fast enough so it can be effective at alternating vehicle states as discussed in **Actuator requirements** and withstand forces that originate from the chosen actuation point in **Active camber actuation point**. The process of meeting these actuator requirements is addressed in the first part of **chapter 3**. The Mathworks Simscape Multibody model is used to model individual parts of the McPherson suspension where the estimation of required force, speed, and the stroke length is taken.

The actuator has to be able to establish the given camber angle and compensate all the parasitic effects discussed in **Camber development**. The generated camber angle should maximize the performance of the vehicle based on the **Camber benefits** section and be robust to the variations determined in the **Parameters and control requirements**. Due to complexity, the control law is divided into two parts Low-Level and High-Level. The Low-Level directly controls the actuator and ensures that the set camber angle will be realized. The Mathworks Simscape model will be used to design and test it. It is presented in the second part of **chapter 3**. The **chapter 4** is dedicated to the High-Level controller. The High-Level control law sets the camber angle for the Low-Level. It takes into account the driver inputs and chooses the appropriate camber angles.

The **chapter 5** is devoted to the testing of the Low-level and High-level controllers. The controllers are first tested in robustness and disturbance rejection and then in the reference tracking in the various experiments that simulate real-world situations like a wind gust.

Chapter 3

Mechatronic system control implementation

In this chapter, the actuator and Low-level controller are derived for the McPherson suspension that is used in the CTU demonstrator. See Attachments for **Double wishbone suspension**. The first section **Camber actuation** defines the actuator parameters based on the boundary conditions. The **Actuator range**, **Acting forces** and **Actuator response time** requirements are presented in the framework of the Simscape model. However, the type of the actuator chosen with the given parameters is not commercially available and thus the final specifications are resolved in the **Resultant actuator specifications**. The Low-level controller is tackled in the **Low-level controller**. The solution requires the estimation of other parameters like roll angle that are addressed in **Roll estimation** section. The nonlinear mapping approach is also enhanced with the controller in **Control law: Feedback PI controller** for the robustness stability. The last section **Compensation of the KPI and caster influence on camber** focuses on the minimization of the steering angle effects on the camber angle. The final controller can fully compensate all the effects on the camber angle that were discussed in the **Camber development**.

3.1 Camber actuation

The actuation point of the camber was chosen in the **Active camber actuation point** together with the actuation speed in the **Actuator requirements**. The suspension dynamics are very delicate and complex, making them hard to describe by the differential equations. The Simscape model presented in the **Simscape model of suspension** is used to ease this process and define the dynamics. The actuator is modeled as a prismatic joint whose input is the distance d on the rail. The required forces to achieve the displacement

are calculated automatically by Simscape. However, there are no saturation limits and dynamics of the response time for the actuator. The actuator span is addressed in the **Actuator range** and the response time in the **Actuator response time**. The actuator also has to be able to withstand all forces that it encounters and, on top of that, actuate the camber angle, see section **Acting forces**.

■ 3.1.1 Actuator range

The amount of the camber angle needed for the active camber actuation has to be established to determine the actuator stroke length range. The regular tires R18 205/45 used in the CTU demonstrator vehicle are not designed for the large camber angles. The caster-camber plates can adjust the static camber angle by $\pm 3^\circ$ in the conventional vehicle. The camber range used by the KTH demonstrator vehicle [27] is $\pm 15^\circ$, but they used non-commercial tires that are specialized in the generation of the camber thrust. Thus, the camber angle range was chosen to be $\pm 5^\circ$ so that the camber thrust can still be effective and the tires do not experience excessive tire wear. The exact camber range for the tire is hard to determine because it depends on many factors like racetrack design, suspension geometry, and stiffness, weight, tire material compound, temperature etc.

However, the camber angle is also influenced by roll angle φ , KPI, and ϕ caster angle as discussed in the **Camber development**. The actuation range of the camber angle has to account for these effects. The roll angle for the lateral acceleration of $a_y = 1g$ is shown in Figure [3.1] with the camber gained. The maneuver can be mirrored, so the maximum value of the camber angle from the left and right sides has to be considered. The model was subjected to side force $F_y = m_{axle}g$ where the m_{axle} is the vehicle mass supported by the axle. The vehicle is assumed $L_f = L_r$ as defined in table [2.1] and thus $m_{axle} = \frac{m}{2}$. The graph also shows different mass variations that represent the load shifting in the vehicle. The maximal approximate value is found to be $\gamma_\varphi = \pm 5^\circ$, see Figure [3.1]. Note that the camber angle gains in the real vehicle will be smaller because the friction and displacements of the joints are neglected.

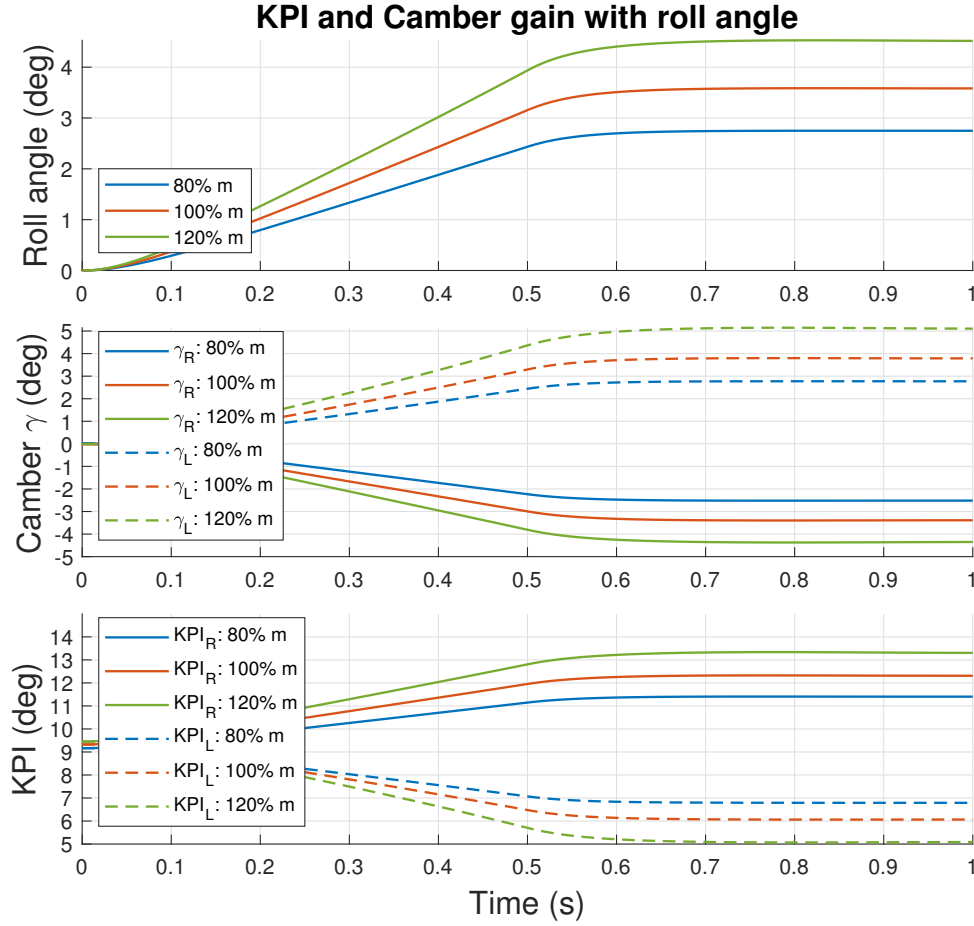


Figure 3.1: The camber gain from the roll angle in the Simscape suspension model with m_{axle} mass. The model was subjected to ramp of the side force $F_y = m_{axle} g$ for different mass variations.

The steering angle with caster angle ϕ and KPI also produces camber. The formula describing the relation is defined in (E.12). The caster angle is constant, see table [2.1], but the KPI angle is changing with the length of the spring-damper in the McPherson strut. The KPI angle variation in the turn with $a_y = 1 g$ is depicted in Figure [3.1]. The Simscape model has KPI = 9.5° when it is at rest. The inner wheel in the maneuver has KPI = 13° and the outer wheel KPI = 5° in the worst case when the axle is overloaded. The caster angle is assumed constant $\phi = 2^\circ$ for both wheels. If the steering angle is assumed to be $\delta = 10^\circ$ (right turn), the equations (3.52) and (3.53)

presented in **3.3** define the camber gain for both wheels:

$$\Delta\gamma_R = 0.5^\circ, \tag{3.1}$$

$$\Delta\gamma_L = -0.3^\circ. \tag{3.2}$$

The table [3.1] describes the required camber angle range. The table is read as follows. For example, the left wheel has to be able to actuate between $\langle -5^\circ, 5^\circ \rangle$. To achieve the -5° camber angle, the wheel has to compensate the 4.7° that comes from the body roll and CASTER+KPI. Thus, the total amount of the camber angle required for the -5° is -9.7° .

Camber gain type	Left wheel camber	Right wheel camber
Wheel camber actuation	$\langle -5^\circ, 5^\circ \rangle$	$\langle -5^\circ, 5^\circ \rangle$
Body roll	5°	-5°
Caster+KPI	-0.3°	0.5°
Total required	$\langle -9.7^\circ, 0.3^\circ \rangle$	$\langle -0.5^\circ, 9.5^\circ \rangle$

Table 3.1: The table describing the total amount of the camber angle needed to compensate for the different camber gains and parasitic effects for the right turn.

However, the problem is mirrored because the vehicle can turn also in the opposite direction to the left. Thus, the worst case of the total amount presented in table [3.1] must be provided on both wheels. The required camber actuator range is $\langle -9.7^\circ, 9.7^\circ \rangle = 19.4^\circ$.

The amount of the actuator stroke length needed can be estimated from the camber to rail coefficient $\gamma_{ratio} = 0.82^\circ/\text{cm}$ which is derived from the Figure [3.2]. Thus, the maximal amount of stroke length d_{max} required to fully compensate and actuate the dynamics of the vehicle is:

$$d_{max} = 19.4^\circ / \gamma_{ratio} \approx 24 \text{ cm}. \tag{3.3}$$

Thus, the saturation limit and the actuator range is set in the interval: $\langle \mathbf{0}, \mathbf{24} \rangle$ cm. Note that the purpose of the γ_{ratio} is to ease the notation for the estimation of the actuator parameters and it is in no way used in the development of the control algorithms.

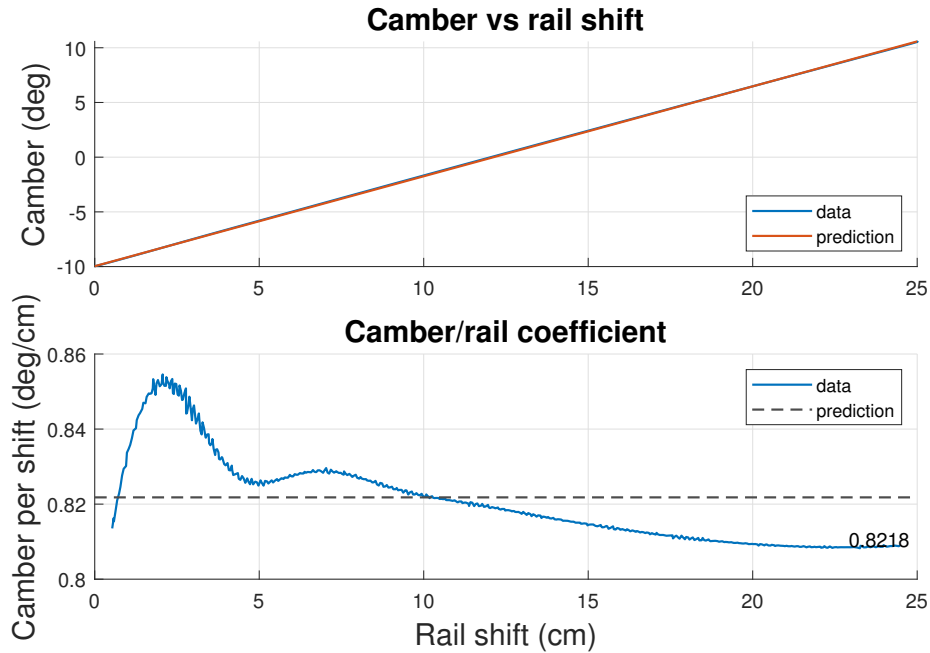


Figure 3.2: The calculation of the camber to rail ratio. The data are measured from the actuator stroke length defined as the extension of the prismatic joint to the camber angle of the wheel in the **Simscape model of suspension**.

3.1.2 Actuator response time

The prismatic joint, that models the actuator in the Simscape, doesn't have any internal dynamics that constrain its response time. Thus, the actuator moves almost as fast as the Δd in its input. That is why, the actuator model is created as shown in diagram [3.3]. The model consists of the low-pass filter for the linear dynamics and the nonlinear rate-limiter and saturation. The low-pass filter is defined as discussed in the **Actuator requirements** and the saturation from the **Actuator range**. The theoretical rate-limiter value can be found with the camber to the rail coefficient ratio γ_{ratio} from Figure [3.2] as $29^\circ/\text{s}/\gamma_{\text{ratio}} \approx 35.4 \text{ cm s}^{-1}$. However, the actual value depends on the type of actuator that is commercially available, see **Resultant actuator specifications**.

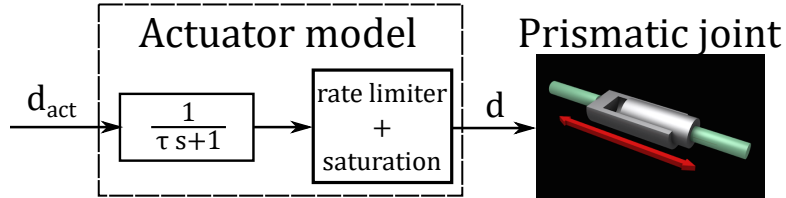


Figure 3.3: The model of the actuator with input d_{act} and output distance d to the prismatic joint in the Simscape. The $\tau = 1/29\text{s} \approx 0.035\text{s}$ while the saturation is from $0 - 24\text{cm}$ and the rate limiter $\pm 35.4\text{cm/s}$. The picture of the prismatic joint from: [9]

3.1.3 Acting forces

The actuator is subjected mainly to the lateral F_y and normal F_z forces. The diagram showing their propagation through the McPherson suspension is depicted in Figure [3.4].

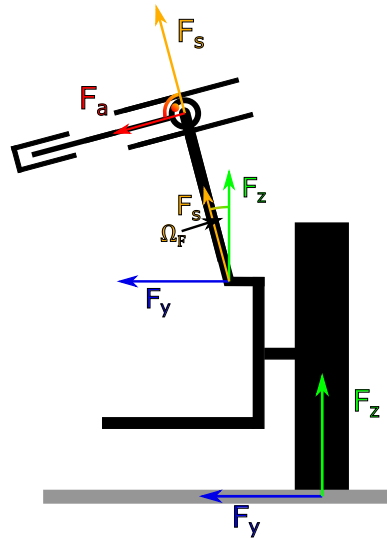


Figure 3.4: The normal and lateral force development through the McPherson suspension for the right wheel.

The F_y and F_z transform to the F_s that propagates through the spring-damper in the McPherson strut and the F_a is the force that the actuator is subjected to and has to withstand. The rail in the Figure [3.4] is perpendicular to the McPherson strut as defined in **Simscape model of suspension** and thus the $F_a = 0$ because no force is transferred onto the actuator. That

is why car manufacturers do not need a strong base to account for these forces. The wheel travel from bumps etc. can change this angle, but it is neglected. On the other hand, the camber actuation can change this angle quite dramatically, and thus an evaluation of the F_y and F_z influence on the F_a has to be made. The diagrams of McPherson strut for the negative and positive camber angle are depicted in Figures [3.5] and [3.6] respectively.

If the maximal lateral acceleration is assumed to be $a_{y_{max}} = 1g$. The amount of the lateral load transfer to one wheel can be calculated from [28] as:

$$\Delta F_{z_{side}} = - \left(\frac{K_f}{w_f} + \frac{K_r}{w_r} \right) - m \frac{a_y}{L_f + L_r} \left(\frac{L_r h_f}{w_f} + \frac{L_f h_r}{w_r} \right) = \pm 4422 \text{ N}, \quad (3.4)$$

$$\Delta F_{z_{wheel}} = \frac{\Delta F_{z_{side}}}{2} = \pm 2211 \text{ N}, \quad (3.5)$$

where the heights are assumed to be $h_r = h_f = h_{CG}$ and the roll stiffness K_f and K_r are calculated from [25] as:

$$K_f = 2 k_f \text{IR}^2 w_f^2 = 21\,315 \text{ N m/rad}, \quad (3.6)$$

$$K_r = 2 k_r \text{IR}^2 w_r^2 = 19\,106 \text{ N m/rad}. \quad (3.7)$$

The vehicle CG is at its center because $L_f = L_r$ and thus (3.5) is half of (3.4). The installation ratio IR is calculated in the attachments **Calculation of the installation ratio IR**. The tire stiffness is neglected and the anti-roll bar is not present in the model. Thus, the lateral force and normal force, that the wheels are subjected to, are:

$$F_y = \frac{1}{4} m_{\text{whl}} a_{y_{max}} = 3679 \text{ N}, \quad (3.8)$$

$$F_{z_{wheel}} + |\Delta F_z| = \left(\frac{1}{4} + \frac{1}{8} \right) m_{\text{whl}} g = 5890 \text{ N}, \quad (3.9)$$

$$F_{z_{wheel}} - |\Delta F_z| = \left(\frac{1}{4} - \frac{1}{8} \right) m_{\text{whl}} g = 1468 \text{ N}, \quad (3.10)$$

where m_{whl} is the normal load on one wheel. Now, the F_a forces can be established. The maximum amount of camber angle that the CTU demonstrator vehicle can be subjected to in this example is $\gamma_{max} = 5^\circ$ based on the discussion in the **Actuator range** because the other 4.7° will be used for the compensation of effects such as the body roll because the vehicle is subjected to $a_y = 1g$ in this example. The camber actuation is expected to be at $\gamma = -5^\circ$ for the left turn maneuver (right wheel $+|\Delta F_z|$ and $F_y > 0$)

and at $\gamma = 5^\circ$ for the right turn maneuver (right wheel $-|\Delta F_z|$ and $F_y < 0$). The angle Ω_F and the Γ_F is expected to change with the γ as:

$$\Omega_F = \sigma_{shf} - \gamma, \quad (3.11)$$

$$\Gamma_F = 90^\circ + (d - 12 \text{ cm}) \gamma_{ratio}, \quad (3.12)$$

where d is the actuator stroke length.

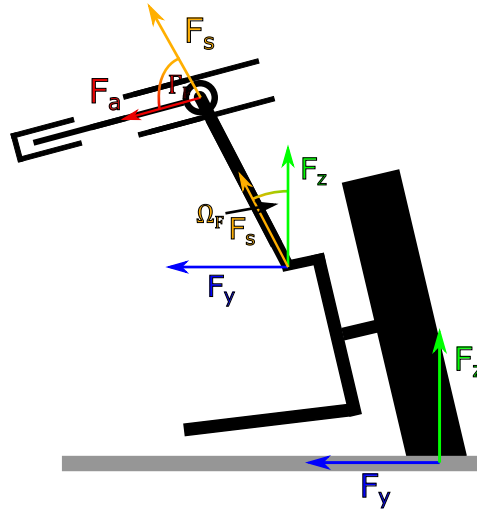


Figure 3.5: The normal and the lateral force development through the suspension with negative camber for the left turn.

The right wheel configuration is examined which is sufficient because the left wheel is mirrored. The force propagation for the left turn based on the diagram in Figure [3.5] is:

$$\gamma = -5^\circ, \quad (3.13)$$

$$\begin{aligned} F_{a,zL} &= (F_{z,wheel} + |\Delta F_z|) \cos(\Omega_F) \cos(\Gamma_F) \\ &= 5890 \cos(7^\circ) \cos(80.3^\circ) \text{ N} = 985 \text{ N}, \end{aligned} \quad (3.14)$$

$$F_{a,yL} = F_y \sin(\Omega_F) \cos(\Gamma_F) = 3679 \sin(7^\circ) \cos(80.3^\circ) \text{ N} = 76 \text{ N}, \quad (3.15)$$

$$F_{a,staticL} = F_{a,zL} + F_{a,yL} = 1061 \text{ N}, \quad (3.16)$$

where $F_{a,zL}$ and $F_{a,yL}$ are the normal and lateral forces respectively that are propagated through the suspension onto the actuator rail for the left turn and the $F_{a,staticL}$ is the total amount of the static force that the actuator has to withstand for this configuration.

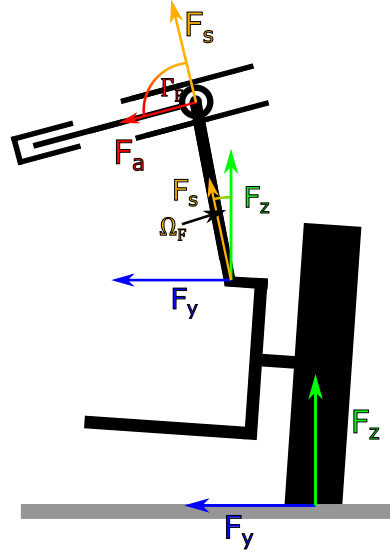


Figure 3.6: The normal and the lateral force development through the suspension with positive camber for the right turn.

The force propagation for the right turn based on the diagram in Figure [3.6] is:

$$\gamma = 5^\circ, \quad (3.17)$$

$$\begin{aligned} F_{a,zR} &= -(F_{z,wheel} - |\Delta F_z|) \cos(\Omega_F) \cos(180^\circ - \Gamma_F) \\ &= -1468 \cos(-3^\circ) \cos(99.7^\circ) \text{ N} = -247 \text{ N}, \end{aligned} \quad (3.18)$$

$$\begin{aligned} F_{a,yR} &= F_y \sin(\Omega_F) \cos(180^\circ - \Gamma_F) \\ &= -3679 \sin(-3^\circ) \cos(99.7^\circ) \text{ N} = -32 \text{ N}, \end{aligned} \quad (3.19)$$

$$F_{a,staticR} = F_{a,zR} + F_{a,yR} = -279 \text{ N}, \quad (3.20)$$

where $F_{a,zR}$ and $F_{a,yR}$ are the normal and lateral forces respectively that are propagated through the suspension onto the actuator rail for the right turn and the $F_{a,staticR}$ is the total amount of the static force that the actuator has to withstand for this configuration.

Thus, the maximal amount of the static force (3.20) and (3.20) that the actuator has to withstand is $\max(|F_{a,staticR}|, |F_{a,staticL}|) = 1061 \text{ N}$. The $\gamma = 5^\circ$ for the left maneuver and $\gamma = -5^\circ$ for the right maneuver configurations on the right wheel are not examined as the camber angle will not be actuated this way. Thus it is pointless to include them. The actuator must also be able to change and actuate the camber angle dynamically. The dynamic force

needed to move the actuator at $29^\circ/\text{s}$ speed is:

$$F_{a,dyn} \approx 700 \text{ N.} \quad (3.21)$$

The force is estimated from the Simscape model, see Figure [3.7]. Thus, the actuator has to be able to form $F_{a,max} = \max(|F_{a,static_R}|, |F_{a,static_L}|) + F_{a,dyn} = 1761 \text{ N}$.

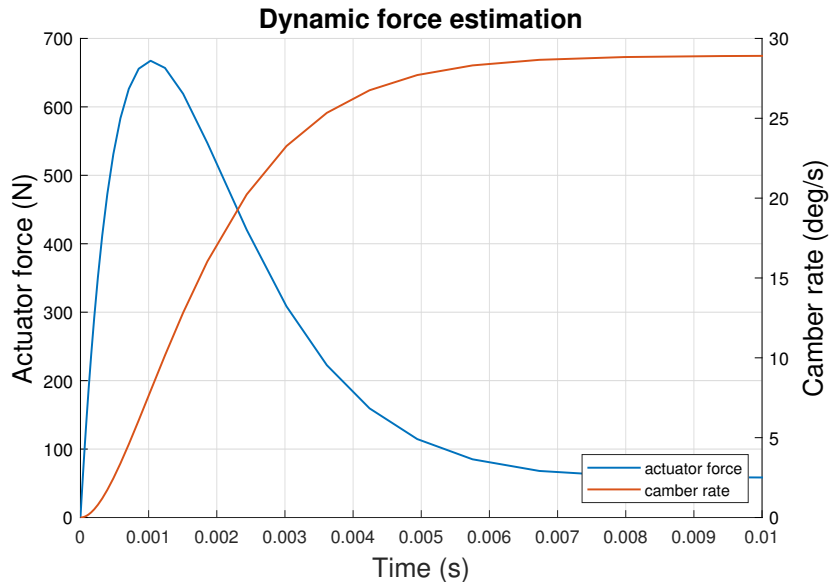


Figure 3.7: The force estimation needed for the actuator to achieve the required speed defined in **Actuator requirements**.

3.1.4 Minimization of static force

The $F_{a,static}$ is produced from the change in the angle between the McPherson strut and the rail, and it is materialized by the actuator when the camber angle is altered. The rail-line can be curved in such a way that minimizes this angle change resulting in minimization of the $F_{a,static}$ force. The derivation is captured in the Figure [3.8]. The example uses $\sigma_{shf} = 10^\circ$ for the simplicity. The point D represents the mounting point of the McPherson strut that is moved by the actuator on the rail, and it stands at the middle of the rail at a 0 camber angle. Thus, the length of the rail from D to one side is $L = 12 \text{ cm}$ from (3.3). The radius R_c defines the circular rail that would be perpendicular to the McPherson strut at all positions. When the point D would be moved to point D_2 , the orange triangle is created where R_c can be

calculated as:

$$R_c = L \tan(80.3^\circ) = 70.2 \text{ cm.} \quad (3.22)$$

Thus, the rail curved with radius $R_c = 70.2$ cm minimizes the static forces induced on the actuator because the angle between the rail and the McPherson strut is almost 90° at all times. The change in spring-damper length does also influence the radius R_c but it is not considered as the angle variation is negligible.

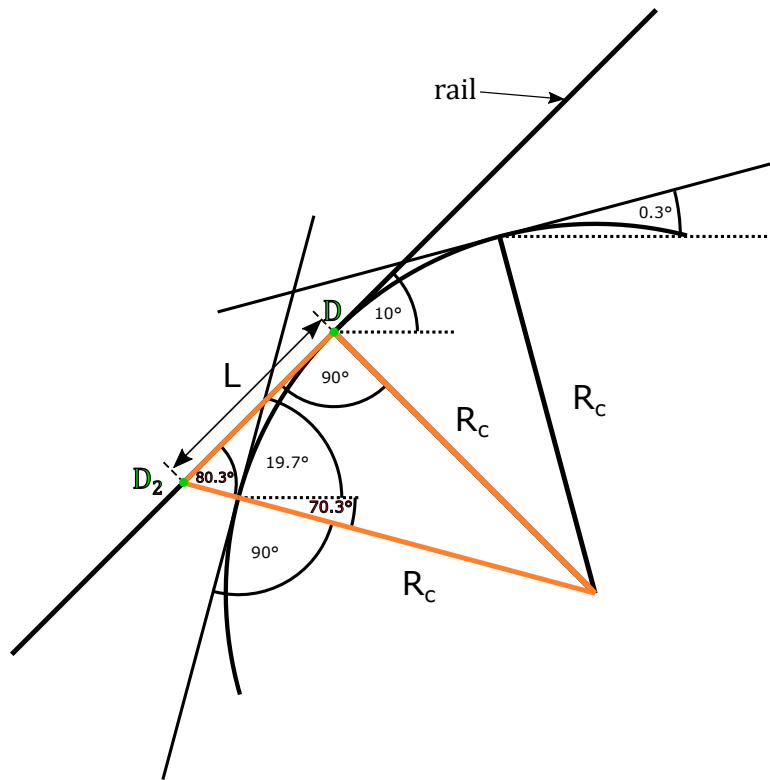


Figure 3.8: The derivation of the radius R_c of the rail that minimizes the angle change between the McPherson strut and the rail for the $\sigma_{shf} = 10^\circ$.

3.1.5 Resultant actuator specifications

The actuator parameters were defined in the dedicated sections above. However, it must be commercially available. The final actuator chosen is the electrical linear actuator due to its cost to power ratio and availability. The disadvantage is that not all of the parameters defined above will be satisfied. The table [3.2] shows the comparison between the actuator parameters. The

force and speed can be interchanged with the gear ratio. The closest match to the expected values is with the gear ratio of 5, and it is shown in the 4th column of ht table [3.2].

Actuator specification	Expected value	Actuator parameter	Chosen match
Push/Pull force	700 N	3500 N	700 N
Maxed push/pull force	1761 N	4960 N	992 N
speed with load	35.4 cm/s	3.7 cm/s	18.5 cm/s
stroke length	24 cm	10 cm	50 cm

Table 3.2: The actuator parameters used in the CTU demonstrator vehicle.

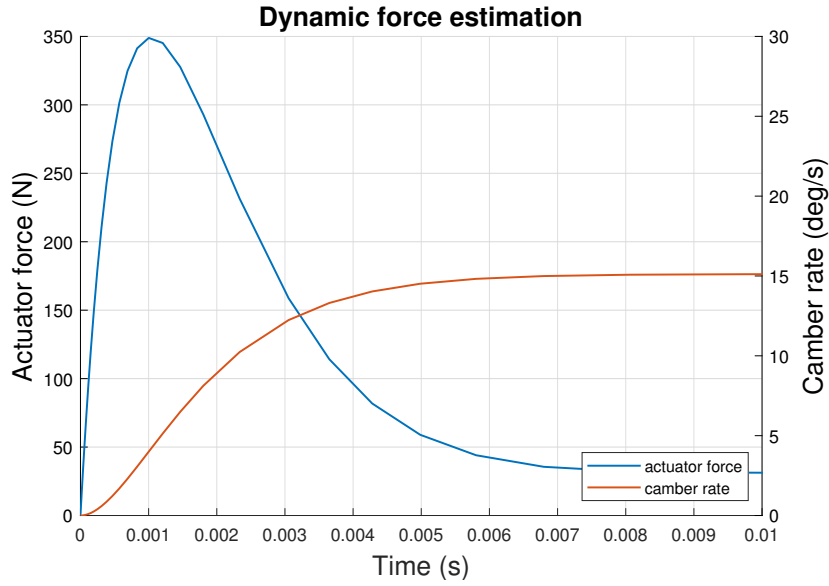


Figure 3.9: The force estimation needed for the actuator to achieve the speed defined in table [3.2].

The speed requirement is the most restrictive. The $18.5 \gamma_{ratio} \text{ } ^\circ/\text{s} \approx 15 \text{ } ^\circ/\text{s}$ which is way below the $29 \text{ } ^\circ/\text{s}$ requirement but fast enough so that the proof of concept can be made. The $F_{a,dyn} = 700 \text{ N}$ will not be needed because it depends on the speed, see Figure [3.9]. The actual value for speed 18.5 cm/s is actually $F_{a,dyn} = 350 \text{ N}$, see Figure [3.9]. Thus, the maximum force that could be required is $F_{max} = 1411 \text{ N}$ which is higher than the estimate of the actuator. However the electric actuator is also self-locking and thus it can withstand much higher force when holding the stroke length. The worst case

would be that the actuator would get stuck or that it would slow down which is deemed suitable for the proof of concept.

■ 3.2 Low-level controller

The McPherson suspension can be modeled with a kinematic geometry model that is discussed in **McPherson geometry model**. The Low-level controller is then derived as the solution of the geometry model in **Control law: nonlinear mapping**. However, it requires an estimation of other parameters like roll angle, which are discussed in **Roll estimation**. The nonlinear mapping controller does not have high enough disturbance rejection and robustness. That is why it is extended by the **Control law: Feedback PI controller**.

■ 3.2.1 McPherson geometry model

The McPherson suspension can be modeled geometrically as 5 points (A,B,C,D,E) in 2D, see Figure [3.10]. The point *A* is at the revolute joint of the lower control arm mounting point. It is assumed that its position is constant and does not change. Next is the point *B* is at the ball joint between the lower arm and the king-pin. The angle θ is defined as the angle of the lower control arm to the ground. The lower arm length is L_1 , and the king-pin with the ball joint is L_2 where both are constants. The king-pin is assumed to be vertically aligned with the wheel as any misalignment is constant and can be subtracted out and compensated. Thus, the camber angle of the wheel is the same as the angle of the king-pin from the perpendicular plane to the ground, see right Figure [3.10]. The point *C* is the highest point of the king-pin, and it is angled from *B* by camber γ as shown. The L_x is the McPherson strut length projected to the point *C*. The Ω_C is the inner angle between the king-pin and L_x arm. Both, the L_x and Ω_C can be calculated from the original McPherson strut length L_s , see attachments **Derivation of McPherson suspension parameters**. The point *D* is at the revolute joint of the McPherson strut mounting point on the rail, and the point *E* is the rail base point. The point *E* is assumed constant, but it rotates around the point *A* by roll angle φ . The d defines the minimum distance between *D* and *E*, and the actuator directly controls it.

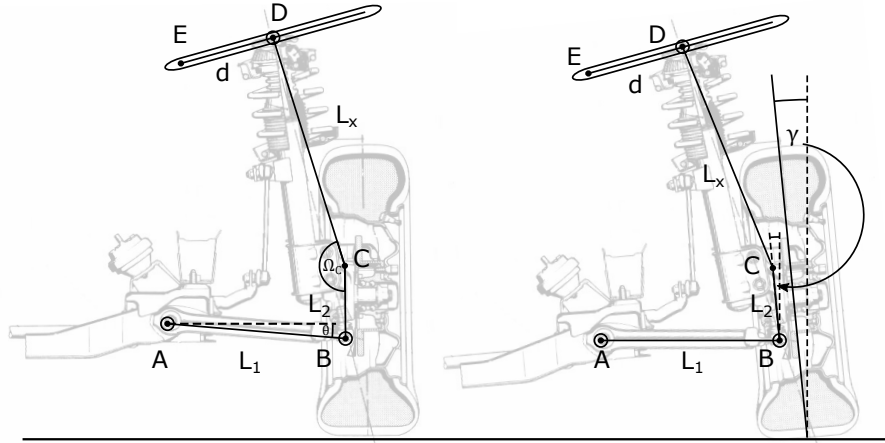


Figure 3.10: McPherson suspension modeled as 5 points. (for background picture see **McPherson**)

3.2.2 Forward kinematics

The geometric model in Figure [3.10] defines the camber angle γ purely from the suspension structure. The forward kinematics must be solved to calculate camber for particular suspension configuration and parameters. The forward kinematics diagram is depicted in Figure [3.11]. The points A and E are known where A is assumed as the center of the coordinate system. Thus, the point E has to be rotated by roll angle φ around the point A :

$$A = \begin{bmatrix} A_y \\ A_z \end{bmatrix} = \begin{bmatrix} 0 \\ 0 \end{bmatrix}, \quad (3.23)$$

$$E = \begin{bmatrix} \cos(\varphi) & -\sin(\varphi) \\ \sin(\varphi) & \cos(\varphi) \end{bmatrix} \cdot \begin{bmatrix} E_y \\ E_z \end{bmatrix}, \quad (3.24)$$

and the point B can be found with angle θ as:

$$B = \begin{bmatrix} L_1 \cos(\theta) \\ L_1 \sin(\theta) \end{bmatrix}. \quad (3.25)$$

The forward kinematics for the camber angle γ from Figure [3.11] can be calculated as:

$$\gamma = -\Lambda_{BE} + \Gamma_B + \Omega_B + \frac{\pi}{2}, \quad (3.26)$$

where

$$\Lambda_{BE} = \arctan 2(E_z - B_z, E_y - B_y), \quad (3.27)$$

$$\Gamma_B = \arccos \left(\frac{|\mathbf{BE}|^2 + |\mathbf{BD}|^2 - d^2}{2 |\mathbf{BE}| |\mathbf{BD}|} \right), \quad (3.28)$$

$$\Omega_B = \arccos \left(\frac{L_2^2 + |\mathbf{BD}|^2 - L_x^2}{2 L_2 |\mathbf{BD}|} \right), \quad (3.29)$$

$$|\mathbf{BD}| = \sqrt{L_2^2 + L_x^2 - 2 L_2 L_x \cos(\Omega_C)}, \quad (3.30)$$

$$|\mathbf{EB}| = \sqrt{(E_y - B_y)^2 + (E_z - B_z)^2}. \quad (3.31)$$

For the left side derivation, see attachments **Derivation of the McPherson geometry model for the left side**.

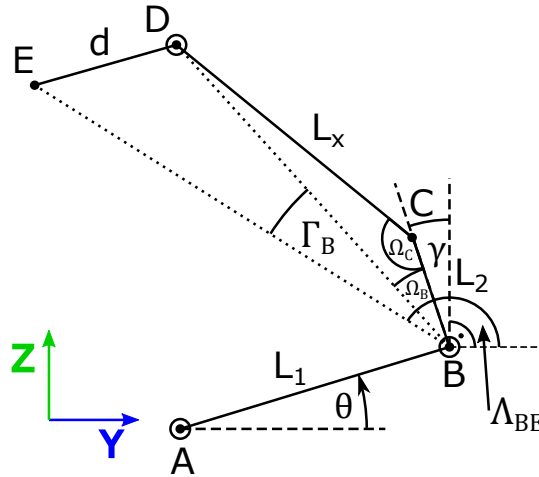


Figure 3.11: Forward kinematics for camber angle γ of model in Figure [3.10]

3.2.3 Control law: nonlinear mapping

The control law defines the input to the actuator so that the reference is met. The **Simscape model of suspension** is used to simulate the system response. The actuator is defined as a prismatic joint from point E to the point D , see Figure [3.12]. Thus, the input to the actuator is d (the distance on the rail between the point D and E). The reference is the camber angle γ_w we want to have.

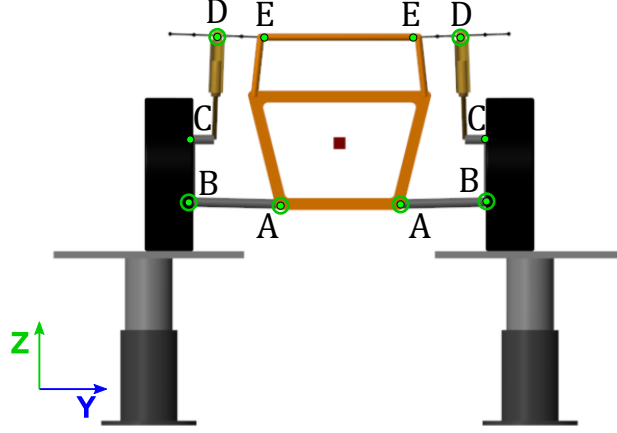


Figure 3.12: The Simscape model with green-highlighted points as in the suspension model in Figure [3.10]. The disk around the points remarks the rotational degree of freedom of the joint.

The equation (3.26) can be used to derive such a law. The γ can be denoted as γ_w and the d is the unknown:

$$\gamma_w = -\Lambda_{BE} + \Gamma_B(d) + \Omega_B + \frac{\pi}{2}, \quad (3.32)$$

and by solving for d the following expression is found:

$$\Gamma_B(d) = \Lambda_{BE} + \gamma_w - \Omega_B - \frac{\pi}{2}, \quad (3.33)$$

$$\frac{|\text{BE}|^2 + |\text{BD}|^2 - d^2}{2|\text{BE}||\text{BD}|} = \cos\left(\Lambda_{BE} + \gamma_w - \Omega_B - \frac{\pi}{2}\right), \quad (3.34)$$

$$|\text{BE}|^2 + |\text{BD}|^2 - d^2 = 2|\text{BE}||\text{BD}| \cos\left(\Lambda_{BE} + \gamma_w - \Omega_B - \frac{\pi}{2}\right), \quad (3.35)$$

$$d = \sqrt{|\text{BE}|^2 + 2|\text{BE}||\text{BD}| \sin(-\gamma_w + \Omega_B - \Lambda_{BE}) + |\text{BD}|^2}, \quad (3.36)$$

where due to the nature of the model, the d can be only positive. The solution is actually algebraic and gives precise d distance for reaching the given camber angle γ_w . However, it is assumed that the φ , θ , Ω_C , and L_x are known. The equation (3.36) is derived only for the right side suspension, for the left side see appendix **Derivation of the McPherson geometry model for the left side**. Note that the (3.36) is defined purely from the suspension kinematics. The suspension dynamics play no role in the stroke length determination.

The θ is defined as the angle of the lower control arm to the ground. "to the ground" is crucial here as it is very hard to measure. However, from the **Measured variables** specification, the η can be measured. Obviously, generally the $\eta \neq \theta$ because the η is relative to the chassis and not to the ground. However, the chassis is parallel to the ground whenever the car is not turning, and, more importantly, the angle of the chassis to the ground is the roll angle φ . In conclusion, the θ can be measured as

$$\theta = \eta + \varphi. \quad (3.37)$$

If the η is unavailable, the control law will still apply. However, the solution would be implicit and require an iteration algorithm to solve or a feedback controller, see more in section **Unknown θ angle**.

The L_x and Ω_C can be obtained from the length of the McPherson strut L_s , see attachments **Derivation of McPherson suspension parameters** on how to derive it. The φ is the hardest component to measure, and it is subject to many studies. The section **Roll estimation** is dedicated to its estimation.

The nonlinear mapping diagram of the controller is shown in Figure [3.13]. See **Low-level reference testing** for the controller performance analysis.

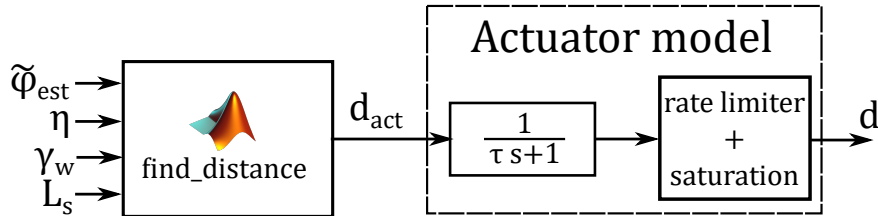


Figure 3.13: The nonlinear mapping controller diagram. The time constant of the low-pass filter is the same as in the actuator requirements in equation (2.21). The saturation is upto 24 cm and the rate limiter to 18.5 cm/s

3.2.4 Roll estimation

The body roll φ is directly proportional to the difference between the McPherson strut lengths L_s on the left and right side and can be estimated as:

$$\tilde{\varphi}_{est} = K_\varphi (L_{sR} - L_{sL}), \quad (3.38)$$

where L_{sL} and L_{sR} is the McPherson strut length for the left and right side respectively. The K_φ depends on many factors like weight distribution, suspension structure etc.. Thus it is found empirically as a constant by

comparing the estimation to the real roll angle from the **Simscape model of suspension**. To increase the measurement accuracy, the complementary filter is added. It predicts the measured variables based on their rate. The diagram for φ is shown in Figure 3.14.

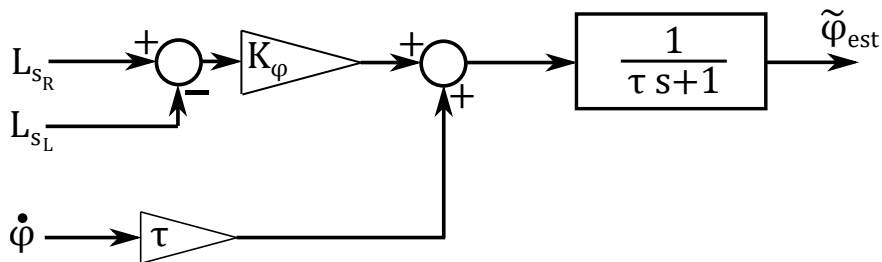


Figure 3.14: Roll estimation diagram with the complementary filter.

The time constant τ sets how much of the rate should be considered for the prediction. It was chosen to be $\tau = 0.005$ s. The **Simscape model of suspension** is used to simulate the suspension dynamics. Figure [3.15] shows the roll angle estimation for the different turns. The bumps and holes have fast dynamics, so the roll angle is hard to estimate, especially when the wheel is in the air, see Figure [3.16]. For example, when the road bump ceases, the wheel is temporary in the air before it hits the ground again, and the formula (3.38) fails to predict the roll angle properly. However, the complementary filter minimizes the error by almost 10%.

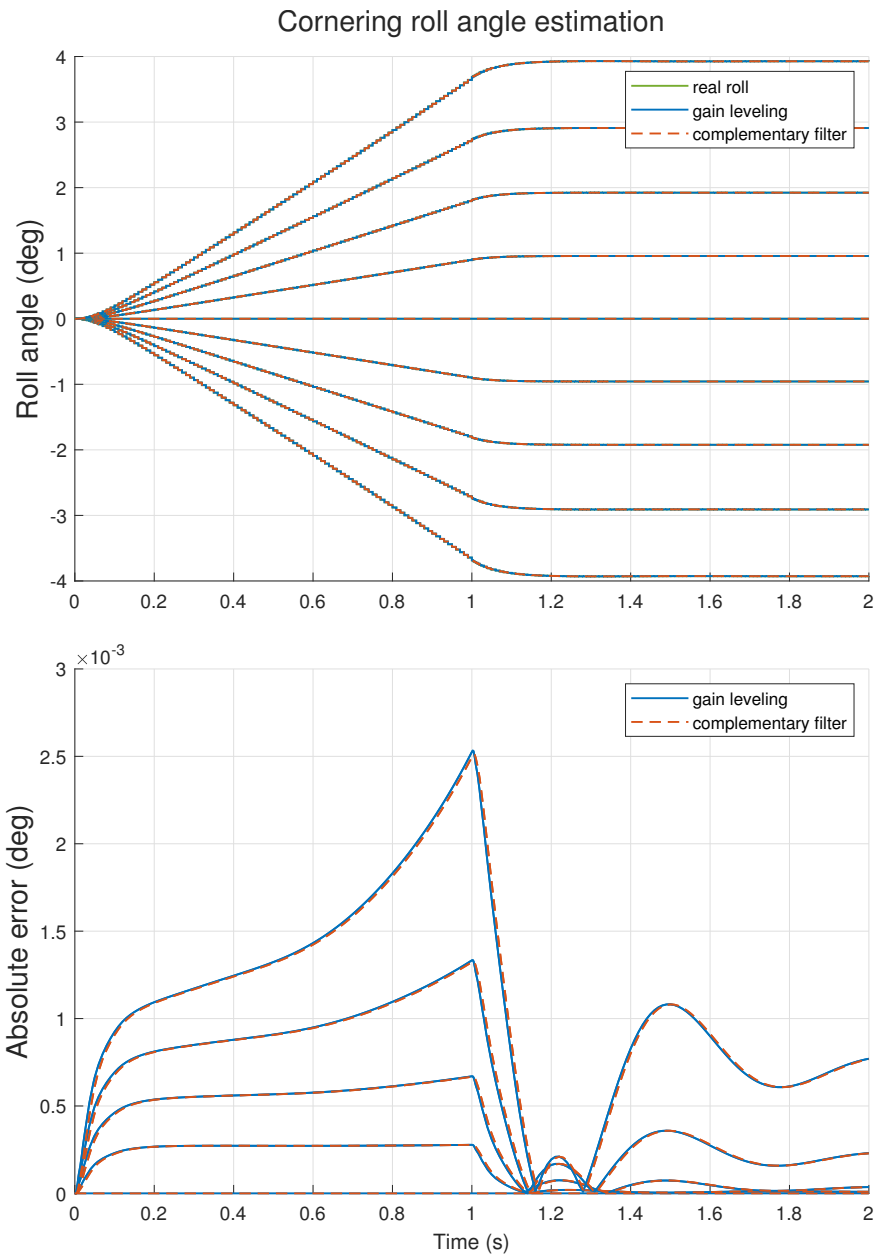


Figure 3.15: The roll angle estimation when cornering with and without the complementary filter.

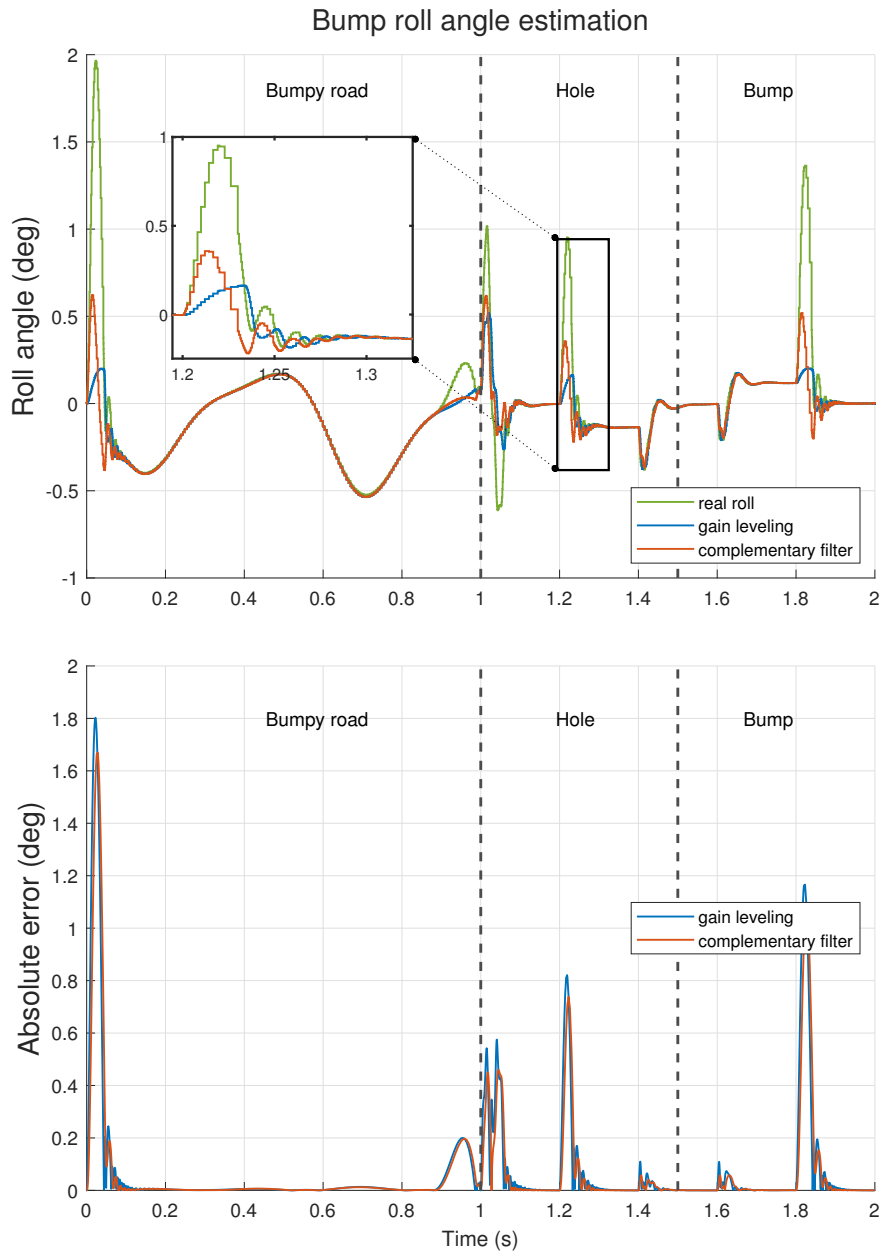


Figure 3.16: The roll angle estimation from the bumps and holds in the road with and without the complementary filter. Whenever, the wheel is in the air, the equation (3.38) fails to predict the roll angle properly.

■ Influence of the alteration of the suspension geometry on the roll angle

The roll angle estimation with formula (3.38) and complementary filter is sufficient for regular driving conditions as shown in Figure [3.15]. However, the actuation of camber also influences body roll. There are two main sources. First, the roll from the structure-change of the suspension. Whenever the $\Delta\gamma \neq 0$, the arrangement of the suspension links is changed, and their difference on the left and right side induces roll. The second reason is the change of the angle between the rail and the McPherson strut at point D, see Figure [3.10]. Conventionally, this angle is constructed such that it is perpendicular to the surface where the McPherson strut is mounted to. However, the rail serves to move point D, which changes the angle. The normal force that compresses the spring is dependent on this angle. Whenever the normal force changes, the spring length is altered as well, which plagues the L_s measurement, see top Figure [3.18]. Both effects are fighting as one rolls the car onto one side and the second to the other, making the estimation very imprecise. The change in the normal force is transferred onto the rail and has to compensate by the camber actuator, see section **Camber actuation**.

The influence of the camber angle on the body roll can be compensated. The top Figure [3.18] marks the amount of the roll gained from the difference of the actuator stroke lengths (distance between the E and D points). A linear function can approximate it. Thus, the final estimation can be augmented by an addition of a linear term that predicts the amount of the roll angle gained from the camber actuation:

$$\tilde{\varphi}_{est} = CF [K_\varphi (L_{sR} - L_{sL})] + K_\gamma (d_R - d_L), \quad (3.39)$$

where $CF[]$ marks complementary filter and d_R and d_L are the right and left actuator stroke lengths (length between the E and D points). The K_γ is approximated with the least-squares method from the difference between the real and predicted roll from the complementary filter, see the error in the middle Figure [3.18]. The bottom Figure shows the absolute error between the new camber-compensated predictor and the complementary filter. The error is significantly reduced. The roll angle is predicted to 0.5° accuracy at the worst case. Note that the worst cases are for the camber configurations that will not be used in the system's normal operation. Figure [3.18] confirms this and depicts the vehicle in a cornering maneuver where the wheels are cambered from 0 to the direction of the turn so that the wheels are leaning into the corner.

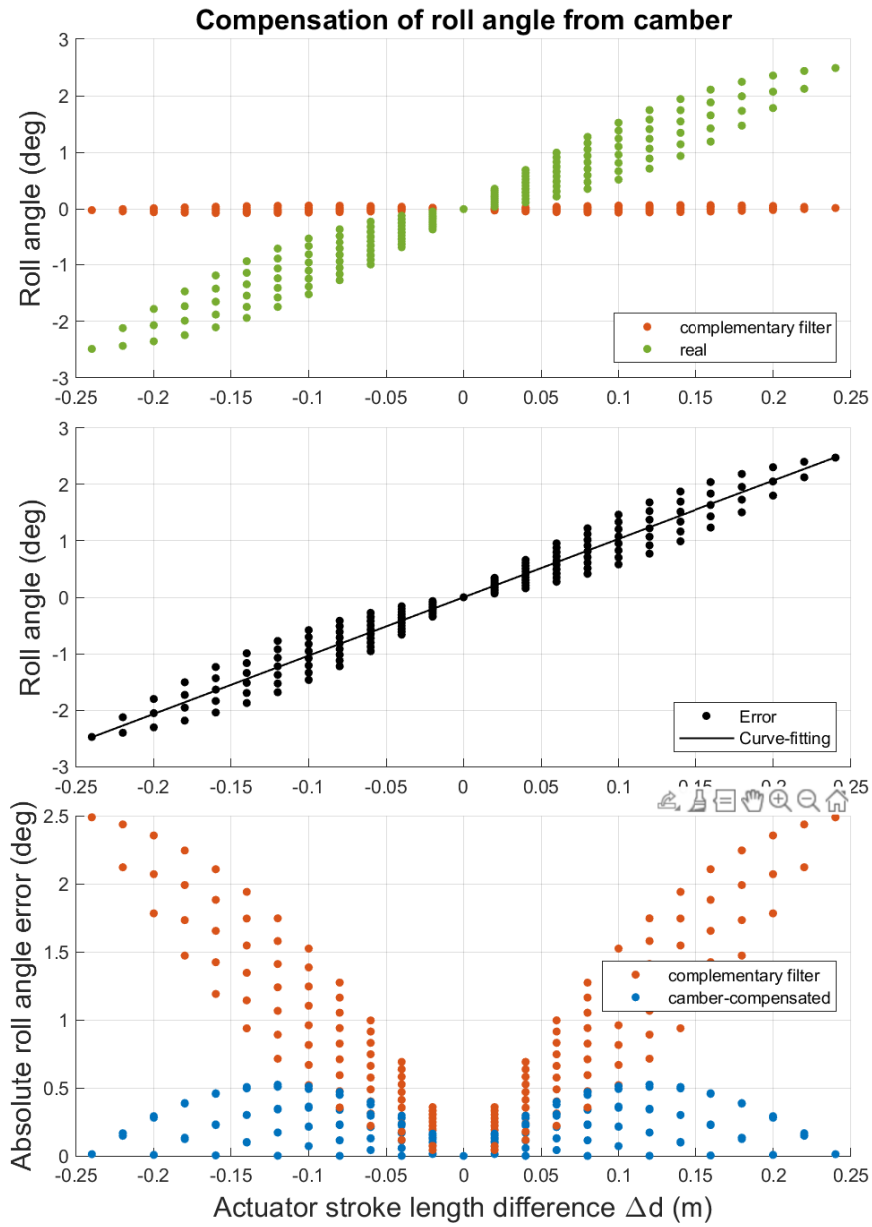


Figure 3.17: The derivation of the camber influence compensation on the roll angle.

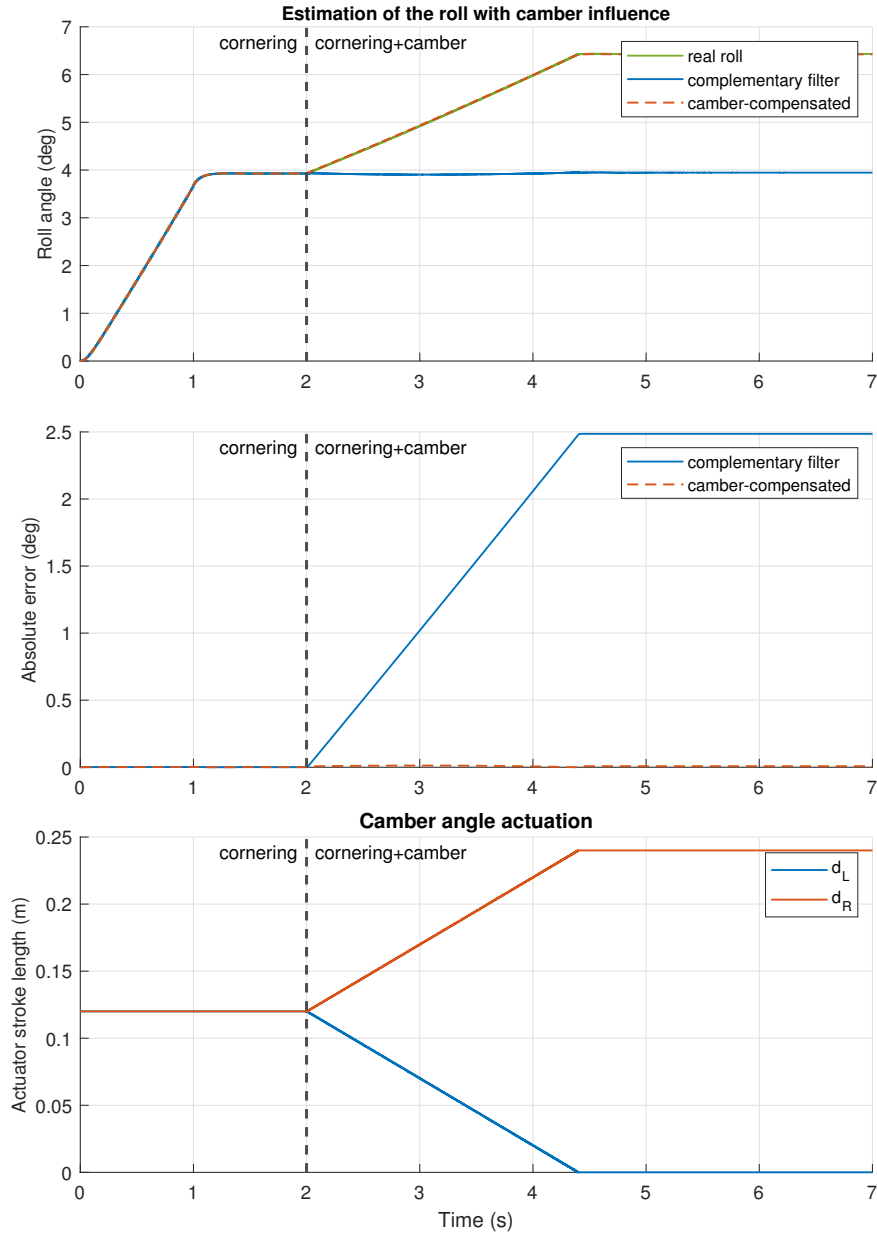


Figure 3.18: The estimation of the roll angle with the camber actuation. The new camber-compensated estimator is compared to the one defined by (3.38). The cornering is simulated as the lateral force $F_y = m_{\text{axle}} a_y$ for $m_{\text{axle}} = \frac{m}{2}$ and $a_y = 1g$.

The roll angle error is not diminished completely with (3.39). The change

of the angle between the McPherson strut and the rail is the reason for the non-linearity in the middle Figure [3.17]. The rail can be curved so that the angle stays at 90 degrees which completely diminishes its effect on the roll angle. Thus, only the structure configuration effect would be left which can be compensated by the (3.39), see section **Camber actuation** for the curvature calculation. The curve-fitting for the curved rail is depicted in the top Figure [3.19]. The non-linearity is greatly reduced. The bottom Figure shows the absolute error of the roll angle between the different approaches where the curved rail has the lowest error. However, the CTU demonstrator will not use the curved rail because its advantage is not high enough to facilitate its construction.

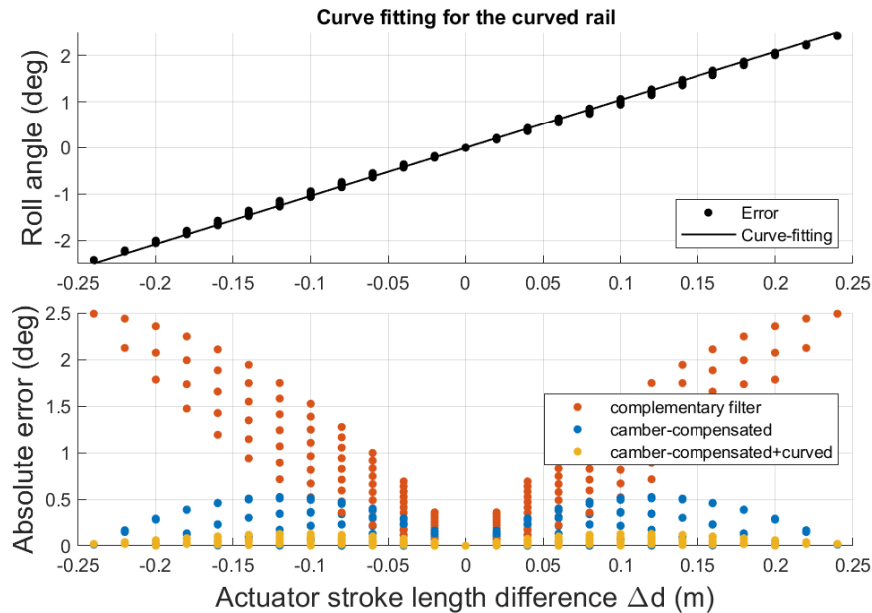


Figure 3.19: The estimation of the roll angle with the camber actuation. The rail is curved in a such a way that minimizes the change in angle between the McPherson strut and the rail. Thus, the non-linearity of Figure [3.17] is removed and the data can be approximated with less error.

3.2.5 Unknown θ angle

Even-though it was establish in section **Active Camber Control system design** that the η can be measured, it is not necessarily needed for the control law definition. Moreover, the measurement device can be damaged or be too noisy. Thus, a new control law is created that does not require η .

If the θ is not known, it has to be calculated to define the new control law. Figure [3.20] shows the diagram of the McPherson suspension model where the θ is derived. The $|\text{BD}|$ and $|\text{AE}|$ are found by (3.30) and (3.42) respectively and the $\kappa = \sigma_{shf}$ because the angle between the McPherson strut and the rail-line is 90 degrees at the nominal camber. The κ is constant because the rail is assumed not curved. However, if the rail was curved, the κ would be a function of the stroke length d . Thus, the point D can be found with:

$$D = \begin{bmatrix} d \cos(\kappa + \varphi) \\ d \sin(\kappa + \varphi) \end{bmatrix} + \begin{bmatrix} E_y \\ E_z \end{bmatrix}, \quad (3.40)$$

where the φ has to be included to account for the body roll rotation. The distances to point A from D and E are defined with euclidean norm:

$$|\text{AD}| = \sqrt{(A_y - D_y)^2 + (A_z - D_z)^2}, \quad (3.41)$$

$$|\text{AE}| = \sqrt{(E_y - A_y)^2 + (E_z - A_z)^2}. \quad (3.42)$$

Then, the Γ_{D1} and Γ_{D2} can be found with cosine rule formulas as:

$$\Gamma_{D1} = \arccos \left(\frac{d^2 + |\text{AD}|^2 - |\text{AE}|^2}{2 d |\text{AD}|} \right), \quad (3.43)$$

$$\Gamma_{D2} = \arccos \left(\frac{|\text{BD}|^2 + |\text{AD}|^2 - L_1^2}{2 |\text{BD}| |\text{AD}|} \right), \quad (3.44)$$

and used to derive distance $|\text{EB}|$:

$$|\text{EB}| = \sqrt{|\text{BD}|^2 + d^2 - 2 d |\text{BD}| \cos(\Gamma_{D1} + \Gamma_{D2})}. \quad (3.45)$$

Finally, the Γ_A is also defined by the cosine formula in triangle $\triangle AEB$ which denotes the final equation for the θ angle:

$$\Gamma_A = \arccos \left(\frac{L_1^2 + |\text{AE}|^2 - |\text{EB}|^2}{2 L_1 |\text{AE}|} \right), \quad (3.46)$$

$$\Lambda_{AE} = \arctan 2(E_z - A_z, E_y - A_y), \quad (3.47)$$

$$\theta = -\Gamma_A + \Lambda_{AE}. \quad (3.48)$$

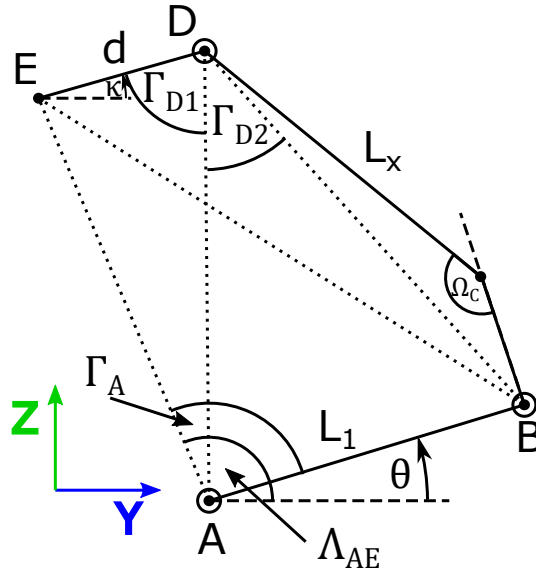


Figure 3.20: The diagram for the derivation of the θ angle from the model in Figure [3.10].

■ Control law: Feedback PI controller

The nonlinear mapping controller finds the stroke length for the referenced camber angle given the state of the system parameters. However, this approach is prone to disturbance, and the controller can experience problems when reaching the reference value because it uses only kinetic nonlinear mapping. Nevertheless, the reference camber angle can also be tracked with the PI controller, which uses the equation (3.48) and (3.26) to estimate the real camber angle of the suspension. The PI controller uses a feedback loop between the reference and the estimation, increasing system robustness and not requiring the η measurement. Both controllers can be used together where the PI helps solve the weaknesses of the nonlinear mapping.

The model is first linearized from the $\gamma_{est} = \gamma$ in (3.26) to the input of the prismatic joint (distance d_{act}) of the **Control law: nonlinear mapping**. The operating point (OP) is chosen as:

$$OP_d = 0.12 \text{ m}, \quad (3.49)$$

$$OP_\gamma = 0^\circ. \quad (3.50)$$

The model verification between the Simscape and the linearized system is shown below. The graph shows the step responses of the nonlinear and linearized system. As expected, the model is valid mainly around the operating

point at 0 camber angle. Nevertheless, the dynamics of the system are captured well.

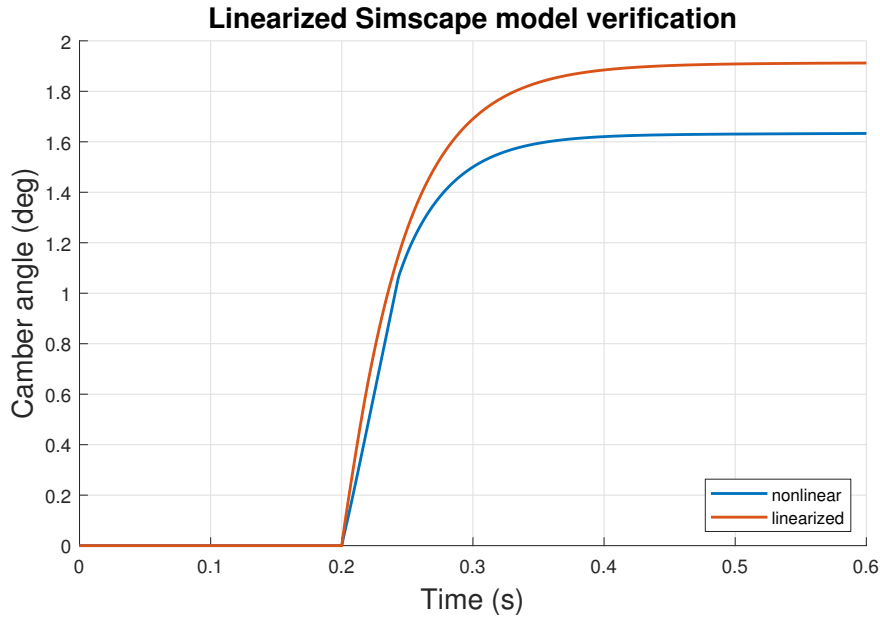


Figure 3.21: Model verification of the step response between the Simscape model and its linearization from the estimated camber to the d_{act} distance.

The controller is modeled with RL-tool, see Figure [3.22]. The controller should ensure minimal overshoot and fast response time. The overshoot is undesirable because it could potentially incentivize camber angles that would be too high for the given maneuver and threaten the vehicle's stability. Small overshoots are allowed because many systems are not modeled precisely and have damping effects on the response. The response time should be close to $1/29s \approx 0.035s$ as discussed in **Actuator requirements**. The step response of the close loop system with the PI controller is shown in Figure [3.22]. The yellow area defines boundaries for the step response as stated above. The step response satisfies both of the requirements and has zero steady-state error that is the defining feature of the PI controller.

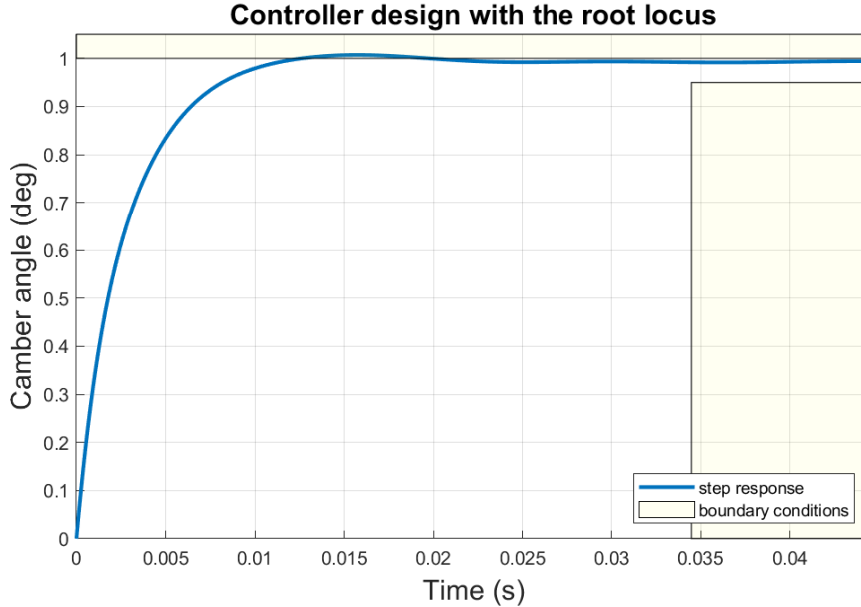


Figure 3.22: The step response of the close loop of the controller and linearized system. The boundary conditions define the area where the controller requirements would be violated. The rise time requirement is taken equal to the steady state. The steady state is achieved when the response value reaches the specified range of 5% of its final value.

The PI controller transfer function of the close loop step response in the Figure [3.22] is:

$$C(s) = \frac{0.2s + 4}{s}. \quad (3.51)$$

The stability limits of the controller are $PM = 93.5^\circ$ and $GM = \infty dB$ which completely satisfies the **Parameters and control requirements**. The diagram of the PI controller structure is shown in Figure [3.23]. The actuator is modeled with the rate-limiter saturation and low-pass filter, which can cause the wind-up phenomenon because of the integrator that is present in the PI. Thus, the back-calculation method with gain K_b is used. It subtracts the additional overshoot of the d_{act} value before the actuator model that is accumulated by the integrator. See **Low-level reference testing** for the controller performance analysis.

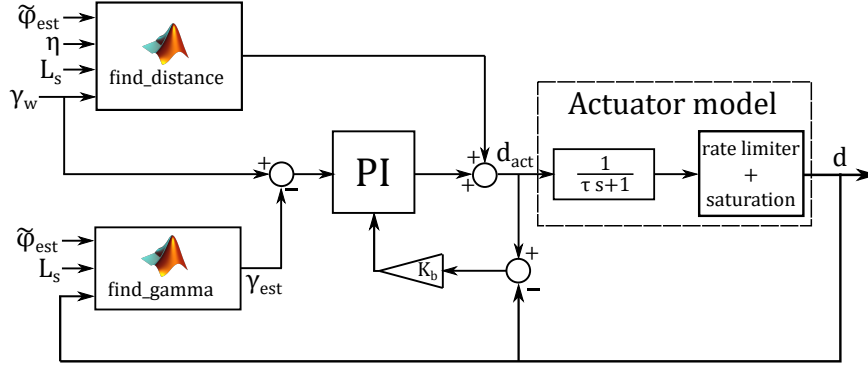


Figure 3.23: The diagram for the PI controller with back-calculation anti-windup with K_b and the reference γ_w with feedback from the γ estimator. The PI controller outputs d_{act} that is added to the nonlinear mapping controller output.

3.3 Compensation of the KPI and caster influence on camber

The wheel camber is also influenced by the KPI and the caster angle when the wheel is steered by δ steering angle. The influence is shown in **Camber development**. The caster leans wheels into the corner and creates beneficial camber. However, it plagues and offsets the estimated camber measurement, and it has to be managed. The article [11] uses a homogeneous transformation to establish the camber angle as a function of ϕ caster, KPI, and δ steering angle. The same derivation will be repeated in the attachments **Derivation of the KPI and caster influence on camber angle** but with the framework established in this thesis. However, to fully understand the derivation, please refer to [11].

The final formulas updated for the notation in this thesis for the left and right wheel are:

$$\gamma_l = -\frac{\pi}{2} + \left[\frac{\cos(\text{KPI}) \sin(\phi)}{\sqrt{1 - \sin(\phi)^2 \sin(\text{KPI})^2}} \sin(\delta) - \frac{\cos(\text{KPI}) \cos(\phi)^2 \sin(\text{KPI})}{\sin(\text{KPI})^2 \sin(\text{KPI})^2 - 1} (\cos(\delta) - 1) \right], \quad (3.52)$$

$$\gamma_r = \frac{\pi}{2} - \left[\frac{\cos(\text{KPI}) \sin(\phi)}{\sqrt{1 - \sin(\phi)^2 \sin(\text{KPI})^2}} \sin(\delta) + \frac{\cos(\text{KPI}) \cos(\phi)^2 \sin(\text{KPI})}{\sin(\text{KPI})^2 \sin(\text{KPI})^2 - 1} (\cos(\delta) - 1) \right]. \quad (3.53)$$

The steering angle δ is known, and the caster angle ϕ is assumed to be held constant. However, the KPI angle is dependent on the spring-damper L_s length. Luckily, it can be calculated from the model in Figure [3.11]. The new model diagram for the KPI angle is depicted in Figure [3.24], see **KPI and scrub radius** for definition.

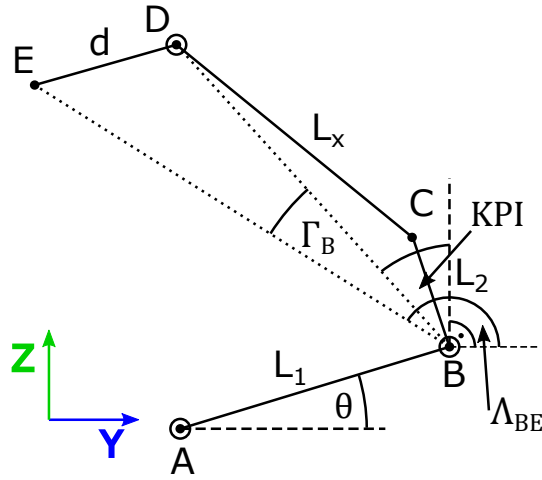


Figure 3.24: Forward kinematics for KPI angle of model in Figure [3.10]

The KPI angle from the diagram [3.24] is found as:

$$\text{KPI} = \Lambda_{BE} - \Gamma_B - \frac{\pi}{2}, \quad (3.54)$$

where Γ_B and Λ_{BE} are defined in (3.28) and (3.27) respectively. Now, the camber angle from the all 3 sources defined in **Camber development** can be estimated.

Chapter 4

Active Camber Control

The High-level controller is responsible for selecting the camber angle for the Low-level controller will be derived here. The **Single track mathematical model** is used to derive the double LQR controller and the **Twin track** to test its performance. First, the design approach is tackled in the section **Design**. Then, the reference signals are derived in **Reference signals** section and the controller structure is shown **Controller structure**. Finally, the **Twin track model with the ACC** demonstrate the capabilities and benefits of the used LQR control.

4.1 Design

The purpose of the controller is to camber the wheels in such a way that the vehicle performance is increased. This means that the controller has to follow the driver's intention. The driver turns the steering wheel and the wheels to perform the maneuver. The wheel steering angles δ can be used to estimate the intended maneuver and transform it into the yaw rate r and sideslip angle β reference that can be followed with the controller, see **Reference signals**. The driver modeling is out of the scope of this thesis because the thesis focuses on the development of the controller for the active camber actuation and not steering. That is why the steering angles are assumed to be given. They can be passed directly by the driver or by another controller.

The sideslip angle β is a very dubious variable, and the estimations generally have quite large errors. For example, the estimation of the β presented in (2.9) would be experiencing random walk due to the integration of the noise and bias. That is very dangerous and creates risk for the integrity and stability of the control law. That is why the sideslip angle is replaced by lateral acceleration a_y measured by accelerometer and the $\epsilon_{\dot{v}_{ref}}$ reference.

The camber angles are assumed to be the same for the left and right wheels on each axle separately, $\gamma_f = \gamma_{FL} = \gamma_{FR}$ and $\gamma_r = \gamma_{RL} = \gamma_{RR}$ (front camber angle is the same for the left and right wheel etc.). The Low-level controller already compensates for the negative effects of cornering on the wheel's camber angle. Moreover, the tire model used for the evaluation does not reflect any advantages of using different camber angles on the left and right sides. The same simplification was used in [17] and many other articles. That is why the notation of the camber angles is also changed for the High-level controller. The Low-level controller has defined positive camber angles when the wheels are leaned to the left and negative when to the right. The High-level controller has the positive camber angles $\gamma_f, \gamma_r > 0$ when the wheels are leaned to the right and negative $\gamma_f, \gamma_r < 0$ when to the left.

4.2 Reference signals

The lateral acceleration of the vehicle measured by accelerometer is composed from the side \dot{v}_y and centripetal accelerations a_c , see Figure [4.1]:

$$a_y = \dot{v}_y + a_c. \quad (4.1)$$

$$(4.2)$$

The \dot{v}_y is used in the single track model and defines purely the lateral side force acting on the vehicle, see right Figure [4.1] where $a_c = 0$. The a_c defines purely centripetal acceleration that the vehicle experiences in the steady state cornering, see left Figure [4.1] where $\dot{v}_y = 0$. Together they constitute the a_y as shown in equation (4.1). The a_c in the steady state cornering can be calculated as:

$$a_c = \frac{V_x^2}{R} = V_x r, \quad (4.3)$$

$$r = \frac{V_x}{R}, \quad (4.4)$$

where the R is the radius of a turn, V_x longitudinal velocity and r the yaw rate.

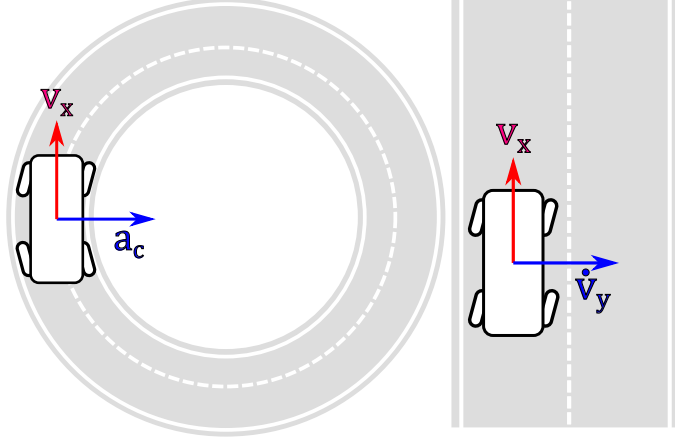


Figure 4.1: The example for the centripetal acceleration a_c and the side acceleration \dot{v}_y .

The yaw rate r from (4.4) is the expected rotational velocity that the vehicle should have to pass around the corner with the radius R and can be used as the desired yaw rate reference r_{ref} . The **Single track mathematical model** model dynamics are completely defined by the yaw rate r and the sideslip angle β . The calculation of the yaw rate r_{ref} and the sideslip angle β_{ref} reference is well known because it is already used in the ESP, see [29]. The [29] presents a way of calculating R which can be used with equation (4.4) to define r_{ref} :

$$r_{ref} = \frac{V_x}{L_f + L_r + \frac{m V_x^2 (L_r C_r - L_f C_f)}{2(L_f + L_r) C_r C_f}} \delta_f, \quad (4.5)$$

where δ_f is the steering angle of the front wheel. The CTU demonstrator vehicle has 4WS. The derivation in [29] can be repeated for the 4WS vehicle to get:

$$r_{ref} = \frac{V_x}{L_f + L_r + \frac{m V_x^2 (L_r C_r - L_f C_f)}{2(L_f + L_r) C_r C_f}} (\delta_f - \delta_r), \quad (4.6)$$

where δ_r is the steering angle for the rear wheel. However, the β_{ref} cannot be derived in terms of both δ_f and δ_r with the approach used in [29]. On the other hand, the single track equation (1.28) defined the differential equation of the β . When the vehicle is in the steady state cornering the $\dot{\beta} = 0$ and the

equation becomes:

$$0 = -\frac{C_f + C_{\alpha_r}}{m V_x} \beta_{ref} + \left(\frac{L_r C_{\alpha_r} - L_f C_{\alpha_f}}{m V_x^2} - 1 \right) r_{ref} + \frac{C_{\alpha_f}}{m V_x} \delta_f + \frac{C_{\alpha_r}}{m V_x} \delta_r, \quad (4.7)$$

where the $\gamma_f = \gamma_r = 0$ as the reference from the driver depends only on the steering angles. The camber angles are controlled by the driver and thus cannot constitute the reference. The r_{ref} in (4.7) is substituted for (4.6) and the equation is solved for β_{ref} to get:

$$\begin{aligned} \beta_{ref} = & \delta_f C_{\alpha_f} \frac{2 C_{\alpha_r} L_r^2 - L_f V_x^2 m + 2 C_{\alpha_r} L_f L_r}{2 C_{\alpha_f} C_{\alpha_r} L_f^2 + 4 C_{\alpha_f} C_{\alpha_r} L_f L_r - C_{\alpha_f} m L_f V_x^2 + 2 C_{\alpha_f} C_{\alpha_r} L_r^2 + C_{\alpha_r} m L_r V_x^2} \\ & + \delta_r C_{\alpha_r} \frac{2 C_{\alpha_f} L_f^2 + L_r V_x^2 m + 2 C_{\alpha_f} L_f L_r}{2 C_{\alpha_f} C_{\alpha_r} L_f^2 + 4 C_{\alpha_f} C_{\alpha_r} L_f L_r - C_{\alpha_f} m L_f V_x^2 + 2 C_{\alpha_f} C_{\alpha_r} L_r^2 + C_{\alpha_r} m L_r V_x^2}. \end{aligned} \quad (4.8)$$

The sideslip angle is defined for constant longitudinal velocity V_x with lateral velocity and acceleration for small angles as:

$$\beta = \frac{v_y}{V_x}, \quad (4.9)$$

$$\dot{\beta} = \frac{\dot{v}_y}{V_x}. \quad (4.10)$$

By substituting for the β and $\dot{\beta}$ in (1.28) by (4.9) and (4.10), the \dot{v}_y side acceleration differential equation is found:

$$\dot{v}_y = -\frac{C_{\alpha_f} + C_{\alpha_r}}{m V_x} v_y + \left(\frac{L_r C_{\alpha_r} - L_f C_{\alpha_f}}{m V_x} - V_x \right) r + \frac{C_{\alpha_f}}{m} \delta_f + \frac{C_{\alpha_r}}{m} \delta_r + \frac{C_{\gamma_f}}{m} \gamma_f + \frac{C_{\gamma_r}}{m} \gamma_r, \quad (4.11)$$

where the reference side acceleration $\dot{v}_{y_{ref}}$ can be derived by substituting the r_{ref} and $V_x \beta_{ref}$ for r and v_y respectively:

$$\dot{v}_{y_{ref}} = -\frac{C_{\alpha_f} + C_{\alpha_r}}{m} \beta_{ref} + \left(\frac{L_r C_{\alpha_r} - L_f C_{\alpha_f}}{m V_x} - V_x \right) r_{ref} + \frac{C_{\alpha_f}}{m} \delta_f + \frac{C_{\alpha_r}}{m} \delta_r + \frac{C_{\gamma_f}}{m} \gamma_f + \frac{C_{\gamma_r}}{m} \gamma_r. \quad (4.12)$$

To exclude the δ_f , δ_r , γ_f and γ_r influence of the input variables on the reference, new variable $\epsilon_{\dot{v}}$ is created:

$$\epsilon_{\dot{v}_{ref}} = \dot{v}_{y_{ref}} - \frac{C_{\alpha_f}}{m} \delta_f - \frac{C_{\alpha_r}}{m} \delta_r - \frac{C_{\gamma_f}}{m} \gamma_f - \frac{C_{\gamma_r}}{m} \gamma_r. \quad (4.13)$$

Thus, the final reference equation for the $\epsilon_{\dot{v}}$ acceleration is defined as:

$$\dot{\epsilon}_{\dot{v}_{ref}} = -\frac{C_{\alpha_f} + C_{\alpha_r}}{m} \beta_{ref} + \left(\frac{L_r C_{\alpha_r} - L_f C_{\alpha_f}}{m V_x} - V_x \right) r_{ref}. \quad (4.14)$$

4.2.1 Handling limits for the vehicle

The references derived above apply to the vehicle in the normal driving conditions. However, there are not bounded by friction limitations of the tires and the road. That is why, the references are bounded by equations derived in [29] as follows:

$$r_{max} = 0.85 \frac{\mu g}{V_x}, \quad (4.15)$$

$$\beta_{max} = \arctan(0.02 \mu g), \quad (4.16)$$

$$a_{y,max} = \mu g, \quad (4.17)$$

where μ is the friction coefficient of the road.

4.2.2 Handling characteristic of the vehicle

The vehicle steering dynamics are generally divided into oversteer, understeer, and neutral steer. The oversteering vehicle turns more than the driver commands it, while the understeering vehicle turns less. The neutral steering vehicle turns the same amount. The handling characteristic of the vehicle is a graph that relates the lateral acceleration to the front steering angle δ_f ($\delta_r = 0$) or to the difference of the front and rear tire slip angle $\Delta\alpha = \alpha_f - \alpha_r$, see Figure [4.2]. It serves to distinguish between the oversteer, understeer, and neutral steer tendencies of the vehicle.

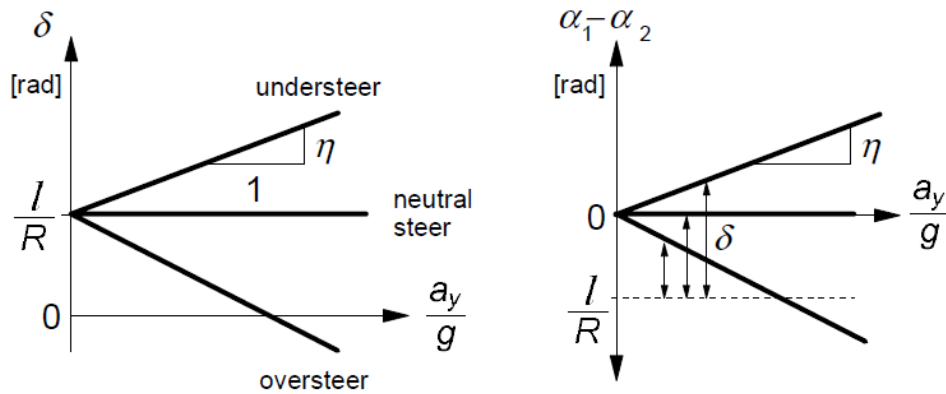


Figure 4.2: The handling characteristic graph of the vehicle describing the oversteer, neutralsteer and understeer tendency from: [10]. The $\alpha_1 = \alpha_f$ and $\alpha_2 = \alpha_r$ and $\delta = \delta_f$.

The LQR uses the references defined in the equations (4.6) and (4.8) that

are calculated from the steering angles δ_f and δ_r . However, the single track model theory can be used to calculate the δ_f and δ_r for given maneuver. The single track model in the maneuver with constant radius R is shown in the Figure [4.3]. The article [30] defines for the Figure [4.3] the relationship for steering angles:

$$\tan(\delta_f - \alpha_f) = \frac{L_f + R \sin(\beta)}{R \cos(\beta)}, \quad (4.18)$$

$$\tan(\delta_r - \alpha_r) = -\frac{L_r - R \sin(\beta)}{R \cos(\beta)}. \quad (4.19)$$

To mitigate the dependency on side slip angle β , the equations (4.18) and (4.19) are redefined as:

$$R \cos(\beta) = R_2 = \sqrt{R^2 - (L_f - L_r)^2}, \quad (4.20)$$

$$R \sin(\beta) = |L_f - L_r|, \quad (4.21)$$

$$\tan(\delta_f - \alpha_f) = \frac{L_f + |L_f - L_r|}{\sqrt{R^2 - (L_f - L_r)^2}}, \quad (4.22)$$

$$\tan(\delta_r - \alpha_r) = -\frac{L_r - |L_f - L_r|}{\sqrt{R^2 - (L_f - L_r)^2}}. \quad (4.23)$$

Solving for the δ_f and δ_r gives:

$$\delta_f = \arctan\left(\frac{L_f + |L_f - L_r|}{\sqrt{R^2 - (L_f - L_r)^2}}\right) + \alpha_f, \quad (4.24)$$

$$\delta_r = -\arctan\left(\frac{L_r - |L_f - L_r|}{\sqrt{R^2 - (L_f - L_r)^2}}\right) + \alpha_r. \quad (4.25)$$

Nevertheless, the equations are dependent on the tire slip angles. The vehicle in the steady state cornering with radius R has $a_y = a_c$ from equation (4.1) because $\dot{v}_y = 0$, see Figure [4.1]. Thus, the following holds true for the tire

slip angles:

$$a_c = \frac{V_x^2}{R}, \quad (4.26)$$

$$m_f = m \frac{L_r}{L_f + L_r}, \quad (4.27)$$

$$m_r = m \frac{L_f}{L_f + L_r}, \quad (4.28)$$

$$F_{yf} = m_f a_y = m \frac{L_r}{L_f + L_r} \frac{V_x^2}{R}, \quad (4.29)$$

$$F_{yr} = m_r a_y = m \frac{L_f}{L_f + L_r} \frac{V_x^2}{R}, \quad (4.30)$$

$$F_{yf} = C_{\alpha_f} \alpha_f, \quad (4.31)$$

$$F_{yr} = C_{\alpha_r} \alpha_r. \quad (4.32)$$

where the (4.31) and (4.32) are linearized lateral forces from the Pacejka Magic Formula as discussed in **Linearization of slip angle**. Solving the set of equations (4.29), (4.30), (4.31) and (4.32) for α_f and α_r yields

$$\alpha_f = \frac{m}{C_{\alpha_f}} \frac{L_r}{L_f + L_r} \frac{V_x^2}{R}, \quad (4.33)$$

$$\alpha_r = \frac{m}{C_{\alpha_r}} \frac{L_f}{L_f + L_r} \frac{V_x^2}{R}. \quad (4.34)$$

Finally, the front and rear steering angles for the maneuver with radius R and velocity V_x are:

$$\delta_f = \arctan \left(\frac{L_f + |L_f - L_r|}{\sqrt{R^2 - (L_f - L_r)^2}} \right) + \frac{m}{C_{\alpha_f}} \frac{L_r}{L_f + L_r} \frac{V_x^2}{R}, \quad (4.35)$$

$$\delta_r = -\arctan \left(\frac{L_r - |L_f - L_r|}{\sqrt{R^2 - (L_f - L_r)^2}} \right) + \frac{m}{C_{\alpha_r}} \frac{L_f}{L_f + L_r} \frac{V_x^2}{R}. \quad (4.36)$$

The equations (4.35) and (4.36) can be used to define the handling characteristic as in Figures [4.2]. The vehicle is tested for a given constant radius R while the car velocity increases, which builds up the centripetal acceleration a_c till the vehicle skids. The handling characteristic is created by plotting the achieved lateral acceleration against the $\Delta\alpha = \alpha_f - \alpha_r$ of the vehicle.

Note of thought, the equations (4.35) and (4.36) define both the steering angles in terms of one variable, the radius of the turn R . **This could be used**

to redefine the steering wheel angle command so that the driver chooses the radius of the turn instead of the steering angle for the wheels. That benefits the High-level controllers because their reference uses the steering angles as the input, and they can be defined by (4.35) and (4.36).

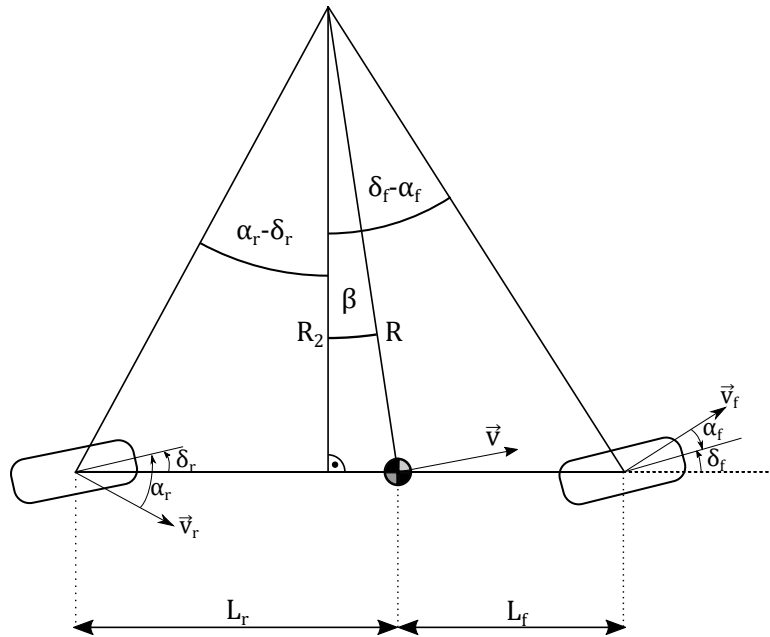


Figure 4.3: The single track model in the steady state cornering maneuver with the constant radius R .

4.3 Controller structure

The chosen controller is the double i -LQR (Linear–Quadratic–Integral Regulator). The LQR design creates state-feedback from the cost function parameters and theoretically guarantees infinity gain margin and phase margin $PM \geq 60^\circ$. The integral ensure zero steady-state error. The controller structure consists of two separate i -LQR’s, one for r_{ref} and one for β_{ref} or $\epsilon \dot{v}_{ref}$, see diagram [4.4]. To prevent the win-up of the integrator when the output value of the controller is saturated, the back-calculation method is employed, see Figure [4.6]. It would be possible to design only one i -LQR for both references. However, it was found that the state-feedback had worse performance. Additionally, the anti wind-up would be more complicated to implement, resulting in further reduction in the performance.

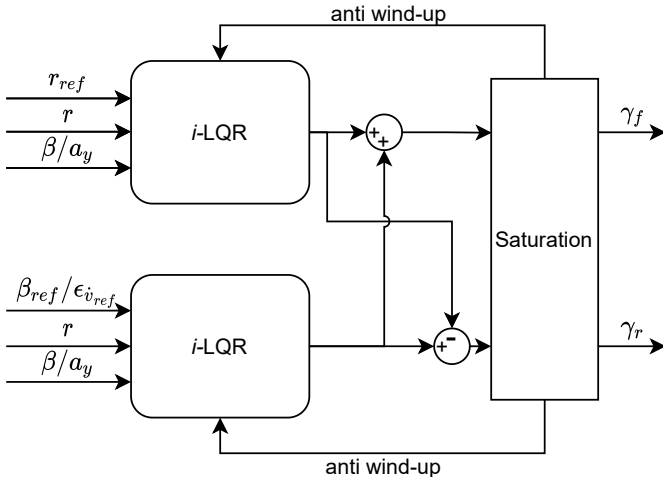


Figure 4.4: The diagram of the double *i*-LQR with r_{ref} and β_{ref} or $\epsilon\dot{v}_{ref}$ reference and state feedback.

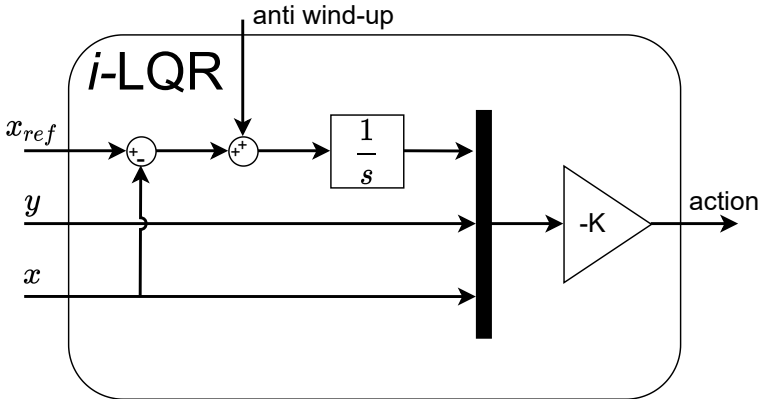


Figure 4.5: The generic *i*-LQR structure with inputs x_{ref}, y, x , action output and state feedback gain K . The anti wind-up from the Saturation diagram [4.6] is fed to the integrator to prevent wind-up.

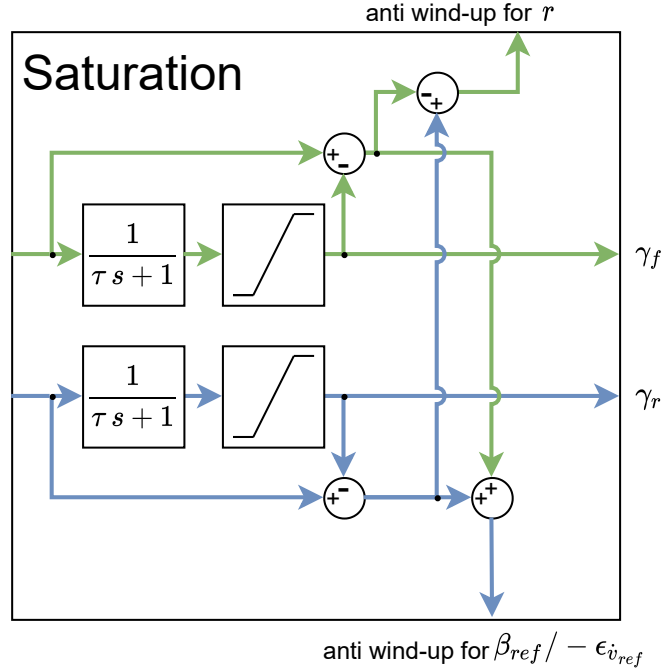


Figure 4.6: The saturation limitation as discussed in **Actuator range** with the low-pass filter to mode the actuator dynamics. The back-calculation method creates the anti wind-up signals that are fed to the LQR. The rate-limiter is omitted so that the step responses are simpler to read through. Note that the impact of the rate-limiter is captured mainly in the rate of change of the signal and not in the dynamics due to the anti wind-up. The $-\epsilon_{\dot{v}_{ref}}$ is negated at the output due to the different notation from (4.54).

4.3.1 LQR with sideslip angle

The i -LQR state-feedback gains are build with the $K = lqr(A, B, Q, R)$ Matlab function. The matrix A and B are taken from the single track state-space form in the (1.30) and augmented for the extra state from the LQR integrator. The input matrix B has only γ_f and γ_r because the δ_f and δ_r are not controlled:

$$B = \begin{bmatrix} \frac{C_{\gamma_f}}{m V_x} & \frac{C_{\gamma_r}}{m V_x} \\ \frac{L_f C_{\gamma_f}}{J} & -\frac{L_r C_{\gamma_r}}{J} \end{bmatrix} \cdot \begin{bmatrix} \gamma_f \\ \gamma_r \end{bmatrix}. \quad (4.37)$$

The A_{new} , B_{new} , Q , R matrices for the yaw rate r are:

$$A_{new} = \begin{bmatrix} 0 & 0 & -1 \\ 0 & & A \\ 0 & & \end{bmatrix}, \quad (4.38)$$

$$B_{new} = \begin{bmatrix} 0 \\ B \begin{bmatrix} 1 \\ -1 \end{bmatrix} \end{bmatrix}, \quad (4.39)$$

$$Q = \begin{bmatrix} 2 \cdot 10^5 & 0 & 0 \\ 0 & 1 & 0 \\ 0 & 0 & 10^3 \end{bmatrix}, \quad (4.40)$$

$$R = 1, \quad (4.41)$$

where the state-feedback gain is $K_r = [-316.2 \quad -1.4 \cdot 10^{-3} \quad 16.5]$ calculated from Matlab function.

The A_{new} , B_{new} , Q , R matrices for the side slip angle β are:

$$A_{new} = \begin{bmatrix} 0 & -1 & 0 \\ 0 & & A \\ 0 & & \end{bmatrix}, \quad (4.42)$$

$$B_{new} = \begin{bmatrix} 0 \\ B \begin{bmatrix} 1 \\ 1 \end{bmatrix} \end{bmatrix}, \quad (4.43)$$

$$Q = \begin{bmatrix} 4 \cdot 10^6 & 0 & 0 \\ 0 & 10^3 & 0 \\ 0 & 0 & 1 \end{bmatrix}, \quad (4.44)$$

$$R = 1, \quad (4.45)$$

where the state-feedback gain is $K_\beta = [1732.1 \quad -9.0 \quad -2.1]$. The step response of the single track system can be seen in Figure [4.7]. There is no overshoot for the yaw rate response so that the vehicle won't overreach the reference and turn too sharply. The settling time of $T_s = 0.5$ s is deemed suitable. The β overshoot can be neglected.

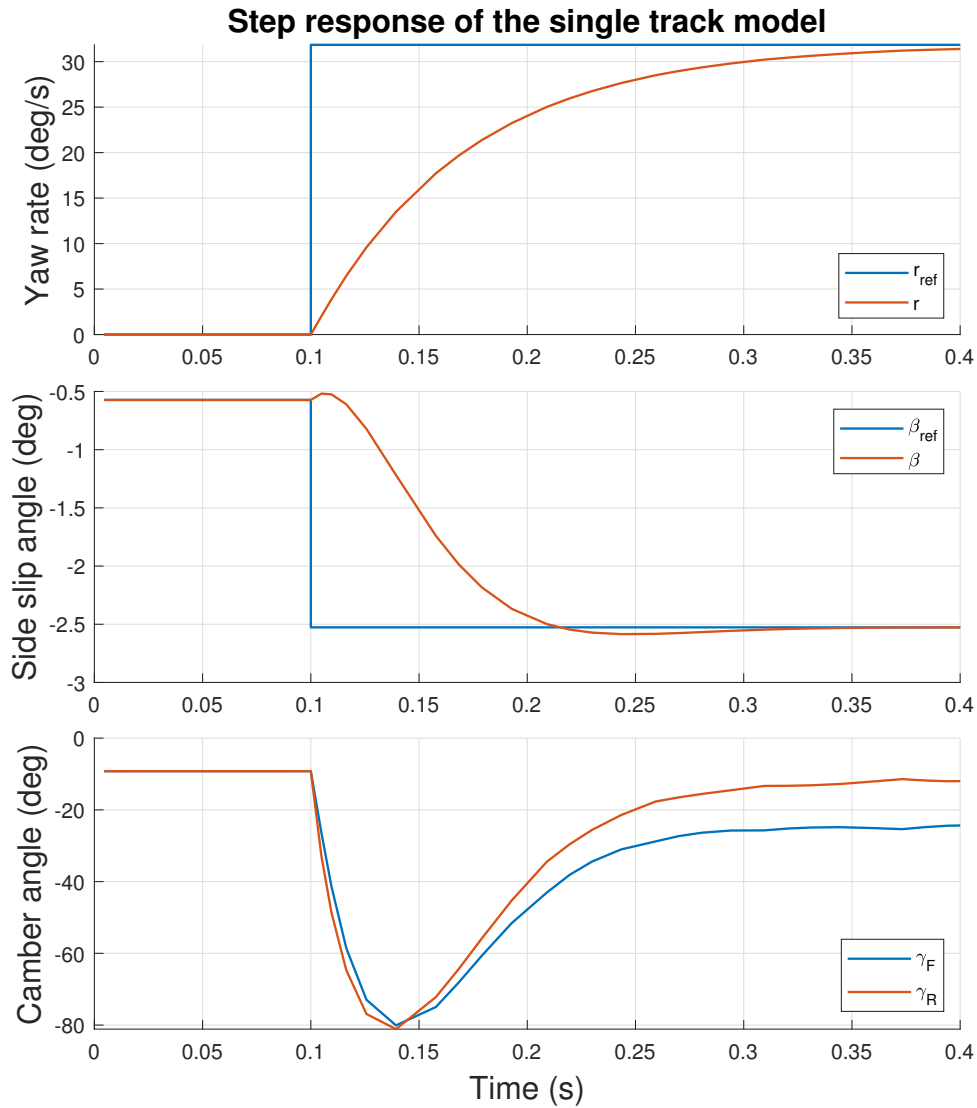


Figure 4.7: The step response of the single track with r and β i -LQR without saturation or low-pass limitations.

4.3.2 LQR with accelerometer

The i -LQR state-feedback gains are built with the $K = lqr(A, B, Q, R)$ Matlab function. However, if the β cannot be measured or precisely estimated, the controller cannot be created the same way as above. The vehicle with only yaw rate r controller would be unable to follow side-ways maneuvers like Double

Lane Change. That is why the accelerometer is used instead. It measures the lateral acceleration a_y of the vehicle where the a_c can be subtracted off to obtain \dot{v}_y by using equation (4.1):

$$a_c = \frac{V_x^2}{R} = V_x r, \quad (4.46)$$

$$\dot{v}_y = a_y - V_x r. \quad (4.47)$$

The \dot{v}_y can be used either to estimate β or it can be directly used to create the controller for the vehicle. The β estimation would lead to the controller stated above, and there are already many published studies about the β estimation. The LQR controller with side acceleration \dot{v}_y state requires a differential equation of \dot{v}_y . So, it has to be derived. The equation (4.11) is stripped of the steering angles as they are not used in the control law:

$$\dot{v}_y = -\frac{C_{\alpha_f} + C_{\alpha_r}}{m V_x} v_y + \left(\frac{L_r C_{\alpha_r} - L_f C_{\alpha_f}}{m V_x} - V_x \right) r + \frac{C_{\gamma_f}}{m} \gamma_f + \frac{C_{\gamma_r}}{m} \gamma_r. \quad (4.48)$$

The differentiation with time of (4.48) is:

$$\ddot{v}_y = -\frac{C_{\alpha_f} + C_{\alpha_r}}{m V_x} \dot{v}_y + \left(\frac{L_r C_{\alpha_r} - L_f C_{\alpha_f}}{m V_x} - V_x \right) \dot{r} + \frac{C_{\gamma_f}}{m} \dot{\gamma}_f + \frac{C_{\gamma_r}}{m} \dot{\gamma}_r. \quad (4.49)$$

Also, the \dot{r} and v_y are defined from the (1.29) and (4.11) respectively:

$$\dot{r} = \frac{L_r C_{\alpha_r} - L_f C_{\alpha_f}}{J V_x} v_y - \frac{L_f^2 C_{\alpha_f} + L_r^2 C_{\alpha_r}}{J v} r + \frac{L_f C_{\gamma_f}}{J} \gamma_f - \frac{L_r C_{\gamma_r}}{J} \gamma_r, \quad (4.50)$$

$$v_y = \frac{m V_x}{C_{\alpha_f} + C_{\alpha_r}} \left(-\dot{v}_y + \left(\frac{L_r C_{\alpha_r} - L_f C_{\alpha_f}}{m V_x} - V_x \right) r + \frac{C_{\gamma_f}}{m} \gamma_f + \frac{C_{\gamma_r}}{m} \gamma_r \right). \quad (4.51)$$

The v_y in equation (4.50) is defined with (4.51) to create the differential equation for \dot{r} . To avoid time differentiation of the input variables in equation (4.49), the new variable $\epsilon_{\dot{v}}$ is created:

$$\dot{v}_y = \epsilon_{\dot{v}} + \frac{C_{\gamma_f}}{m} \gamma_f + \frac{C_{\gamma_r}}{m} \gamma_r, \quad (4.52)$$

$$\ddot{v}_y = \dot{\epsilon}_{\dot{v}} + \frac{C_{\gamma_f}}{m} \dot{\gamma}_f + \frac{C_{\gamma_r}}{m} \dot{\gamma}_r. \quad (4.53)$$

Note that the $\epsilon_{\dot{v}}$ is the same as $\epsilon_{\dot{v}_r \epsilon_f}$ from equation (4.12) but δ_f and δ_r is put to zero for this derivation as stated above. After substitution of \dot{v}_y in (4.49) for $\epsilon_{\dot{v}}$, the final differential equations are:

$$\begin{aligned} \dot{\epsilon}_{\dot{v}} = & - \left(\frac{C_{\alpha_f} + C_{\alpha_r}}{V_x m} + \frac{m(C_{\alpha_f} L_f - C_{\alpha_r} L_r)^2 \left(V_x + \frac{C_{\alpha_f} L_f - C_{\alpha_r} L_r}{V_x m} \right)}{J(C_{\alpha_f} + C_{\alpha_r})} \right) \epsilon_{\dot{v}} \\ & + \frac{\left(V_x + \frac{C_{\alpha_f} L_f - C_{\alpha_r} L_r}{V_x m} \right) \left(\frac{C_{\alpha_f} L_f^2 + C_{\alpha_r} L_r^2}{J V_x} - \frac{m(C_{\alpha_f} L_f - C_{\alpha_r} L_r)^2 \left(V_x + \frac{C_{\alpha_f} L_f - C_{\alpha_r} L_r}{V_x m} \right)}{J(C_{\alpha_f} + C_{\alpha_r})} \right)}{V_x m} r \\ & + \left(-\frac{C_{\gamma_f}(C_{\alpha_f} + C_{\alpha_r})}{V_x m^2} - \frac{C_{\gamma_f} L_f \left(V_x + \frac{C_{\alpha_f} L_f - C_{\alpha_r} L_r}{V_x m} \right)}{J} \right) \gamma_f \\ & + \left(\frac{C_{\gamma_r}(C_{\alpha_f} + C_{\alpha_r})}{V_x m^2} - \frac{C_{\gamma_r} L_r \left(V_x + \frac{C_{\alpha_f} L_f - C_{\alpha_r} L_r}{V_x m} \right)}{J} \right) \gamma_r, \end{aligned} \quad (4.54)$$

$$\begin{aligned} \dot{r} = & \frac{(-L_r C_{\alpha_r} + L_f C_{\alpha_f})m}{J(C_{\alpha_f} + C_{\alpha_r})} \epsilon_{\dot{v}} + \frac{L_f C_{\gamma_f}}{J} \gamma_f - \frac{L_r C_{\gamma_r}}{J} \gamma_r \\ & - \left(\frac{L_f^2 C_{\alpha_f} + L_r^2 C_{\alpha_r}}{J v} + \frac{m(C_{\alpha_f} L_f - C_{\alpha_r} L_r) \left(V_x + \frac{C_{\alpha_f} L_f - C_{\alpha_r} L_r}{V_x m} \right)}{J(C_{\alpha_f} + C_{\alpha_r})} \right) r, \end{aligned} \quad (4.55)$$

$$\epsilon_{\dot{v}} = \dot{v}_y - \frac{C_{\gamma_f}}{m} \gamma_f - \frac{C_{\gamma_r}}{m} \gamma_r = a_y - V_x r - \frac{C_{\gamma_f}}{m} \gamma_f - \frac{C_{\gamma_r}}{m} \gamma_r. \quad (4.56)$$

Finally, the equation (4.55) and (4.54) define new state-space $A_{\epsilon_{\dot{v}}}, B_{\epsilon_{\dot{v}}}$:

$$\begin{bmatrix} \dot{\epsilon}_{\dot{v}} \\ \dot{r} \end{bmatrix} = A_{\epsilon_{\dot{v}}} \begin{bmatrix} \epsilon_{\dot{v}} \\ r \end{bmatrix} + B_{\epsilon_{\dot{v}}} \begin{bmatrix} \gamma_f \\ \gamma_r \end{bmatrix}. \quad (4.57)$$

The matrices for the i -LQR are build similarly to **LQR with sideslip angle**.

The A_{new} , B_{new} , Q , R matrices for the yaw rate r are:

$$A_{new} = \begin{bmatrix} 0 & 0 & -1 \\ 0 & A_{\epsilon_{\dot{v}}} & \\ 0 & & \end{bmatrix}, \quad (4.58)$$

$$B_{new} = \begin{bmatrix} 0 \\ B_{\epsilon_{\dot{v}}} \begin{bmatrix} 1 \\ -1 \end{bmatrix} \end{bmatrix}, \quad (4.59)$$

$$Q = \begin{bmatrix} 10^5 & 0 & 0 \\ 0 & 1 & 0 \\ 0 & 0 & 10^2 \end{bmatrix}, \quad (4.60)$$

$$R = 1, \quad (4.61)$$

where the state-feedback gain is $K_r = [-316.2 \quad -1.4 \cdot 10^{-1} \quad 16.5]$ found by Matlab function.

The A_{new} , B_{new} , Q , R matrices for acceleration $\epsilon_{\dot{v}}$ are:

$$A_{new} = \begin{bmatrix} 0 & -1 & 0 \\ 0 & A_{\epsilon_{\dot{v}}} & \\ 0 & & \end{bmatrix}, \quad (4.62)$$

$$B_{new} = \begin{bmatrix} 0 \\ B_{\epsilon_{\dot{v}}} \begin{bmatrix} 1 \\ 1 \end{bmatrix} \end{bmatrix}, \quad (4.63)$$

$$Q = \begin{bmatrix} 3 \cdot 10^6 & 0 & 0 \\ 0 & 40 & 0 \\ 0 & 0 & 10^3 \end{bmatrix}, \quad (4.64)$$

$$R = 1. \quad (4.65)$$

The state-feedback gain equates to $K_{\epsilon_{\dot{v}}} = [1732.1 \quad -9.0 \quad -2.1]$. The step response of the single track system can be seen in Figure [4.8]. There is no overshoot for the yaw rate response so that the vehicle won't overreach the reference and turn too sharply. The settling time of $T_s = 0.5$ s is deemed suitable. The $\epsilon_{\dot{v}}$ overshoot can be neglected.

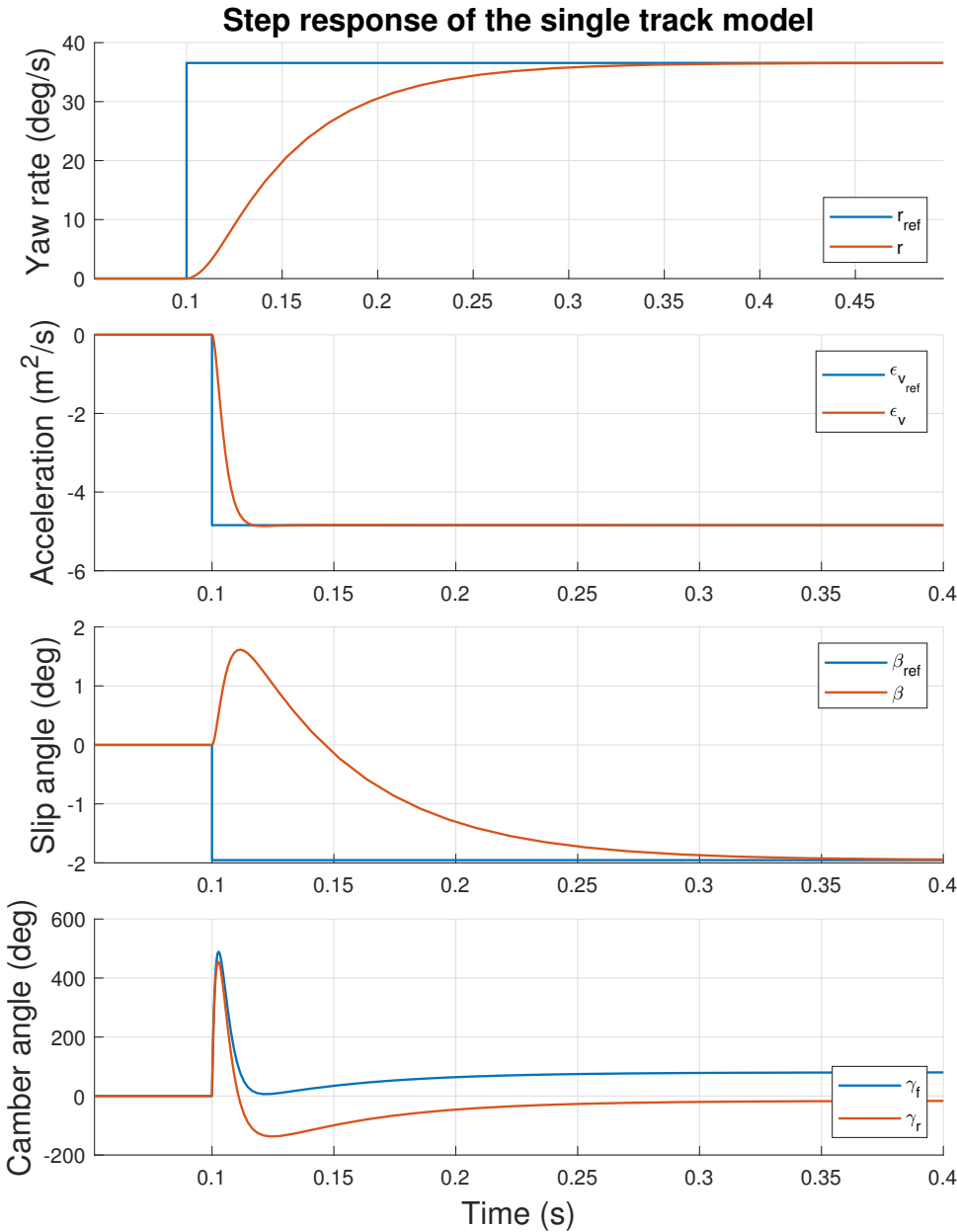


Figure 4.8: The step response of the single track with r and ϵ_v i -LQR without saturation or slew rate limitations.

4.4 Twin track model with the ACC

The Active Camber Control (ACC) is capable of enhancing the cornering ability of the car, see **Maximal lateral acceleration**. The energy-saving potential is explored in **Cornering resistance and energy-saving**, and the ACC can also be used to model match the twin track model to the single track, see **Model matching**. The twin track model in this section is parametrized with the table [2.1] but the CG is moved forward by 5 cm which changes the $L_f = 1.181$ m and $L_r = 1.281$ m variables. Thus, the vehicle is slightly understeering, which most of the vehicles are built to be in the car industry. Note that the purpose of this section is to show the benefits and capability of the ACC. The process can be generalized to any car. The demonstration will be performed with only the **LQR with sideslip angle** for simplicity.

4.4.1 Model matching

The reference created in **Reference signals** does not necessarily need to be with the same parameters that the vehicle has. The vehicles can be neutral, understeering, or oversteering, but these factors are inherently defined in the car. They can be changed only by direct alternations of the load etc. The ACC presents a different option. The reference can be generated for the vehicle with oversteering parameters even though the actual vehicle has understeering behavior. For example, the references can be calculated for the L_f and L_r that were chosen so that the CG is moved by 10 cm to the back even though the vehicle has CG at its center.

The handling characteristic that defines oversteer and understeer is shown in Figure [4.9]. It was created for the constant radius turn $R = 60$ m with equations (4.35) and (4.36). The region above 0 is defined as understeering and below 0 as oversteering. The black dashed lines define references with the increasing velocity created for different CG positions. Note that the references are created with the single track model, and thus the twin track vehicle follows them precisely only with ACC. The vehicle's actual twin track model is understeer and is highlighted with a solid blue line. The Figure [4.9] shows that even though the vehicle is understeering, it can be made oversteering. However, the vehicle performance is lowered, and the maximal lateral acceleration that the vehicle can withstand is smaller.

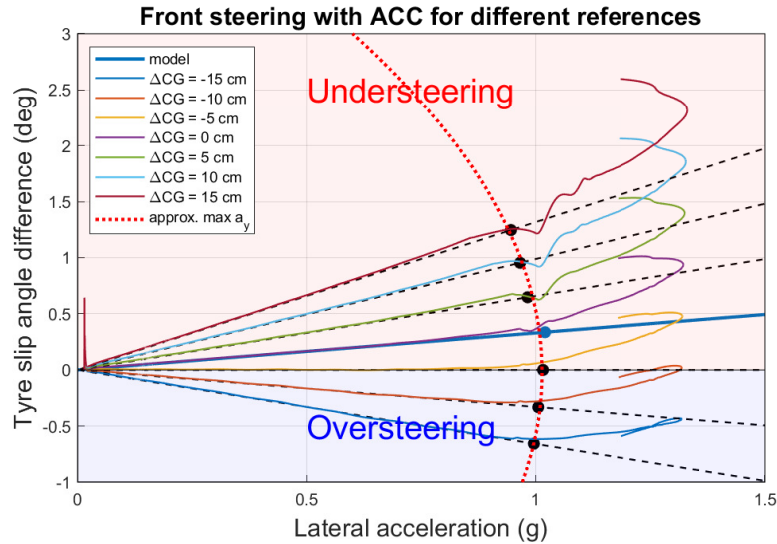


Figure 4.9: The model matching technique that can change vehicle behavior from understeer to oversteer in the steady state cornering with radius $R = 60$ m. The nominal twin track model is highlighted in blue. The other black dashed lines are references are created for different ΔCG . All responses are to the nominal twin track model.

Figure [4.10] shows handling characteristic for the understeering and oversteering twin track model vehicle with and without the ACC. The vehicle has only front steering ($\delta_r = 0$) and $\frac{\partial \delta_f}{\partial t} = 0$. The reference dashed lines in the top Figure [4.10] are not followed with zero error for the vehicle without ACC because the references are created from single track model, not the twin track. Whenever the vehicle moves away from the nominal radius of a turn by 4 m, it is regarded as the lost of control and marked. The vehicle with ACC performs better for both oversteering and understeering vehicles and has higher maximal lateral acceleration. The results for the 4WS vehicle are almost the same.

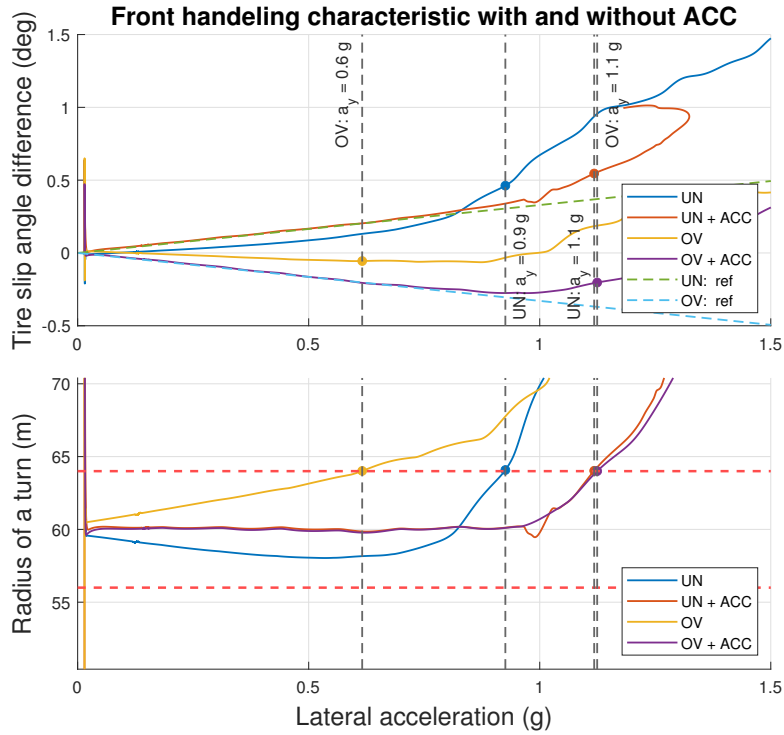


Figure 4.10: The handling characteristic for the constant radius of the turn $R = 60$ m for vehicle with only front wheel steering ($\delta_r = 0$) and $\frac{\partial \delta_f}{\partial t} = 0$. The velocity increases in time. The oversteering and understeering twin track model response are compared with and without ACC.

4.4.2 Maximal lateral acceleration

The maximal lateral acceleration of the vehicle is a well-known parameter that specifies the vehicle's cornering ability. The Figure [4.11] shows the maximal lateral acceleration between front steering vehicle ($\delta_r = 0$) with and without Active Camber Control (ACC). The vehicle with ACC reaches up to $a_y = 1.2$ g that is 25% higher than the vehicle without ACC.

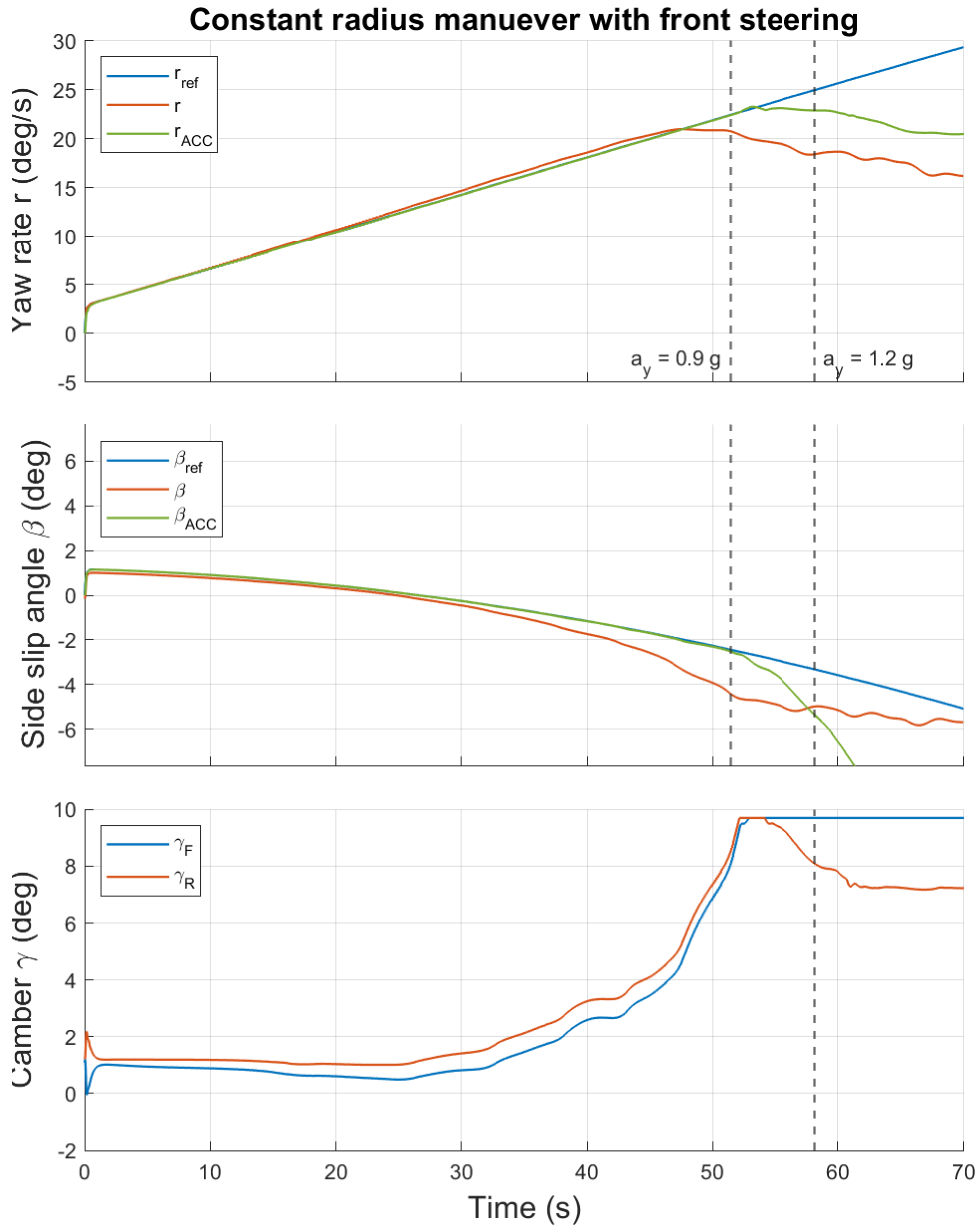


Figure 4.11: The constant radius of a turn maneuver $R = 60$ m with increasing velocity for only front steering vehicle ($\delta_r = 0$). The vehicle is the same as defined in the parameters but it is slightly understeering with CG shifted by 5 cm to the front from the center.

4.4.3 Cornering resistance and energy-saving

The vehicle with ACC has the potential to be more energy efficient during cornering because it uses less slip angle as discussed in **Cornering losses**. Figure [4.12] shows an example of a right turn of the vehicle with and without ACC. The bottom graph compares the cornering losses where the vehicle with ACC is considerably more efficient. Note that the vehicle without ACC does not follow the calculated reference precisely, and thus the value of the consumption might be inflated. However, the difference is negligible ($\approx 1^\circ$) so the Figure [4.12] can still serve as a proof of concept.

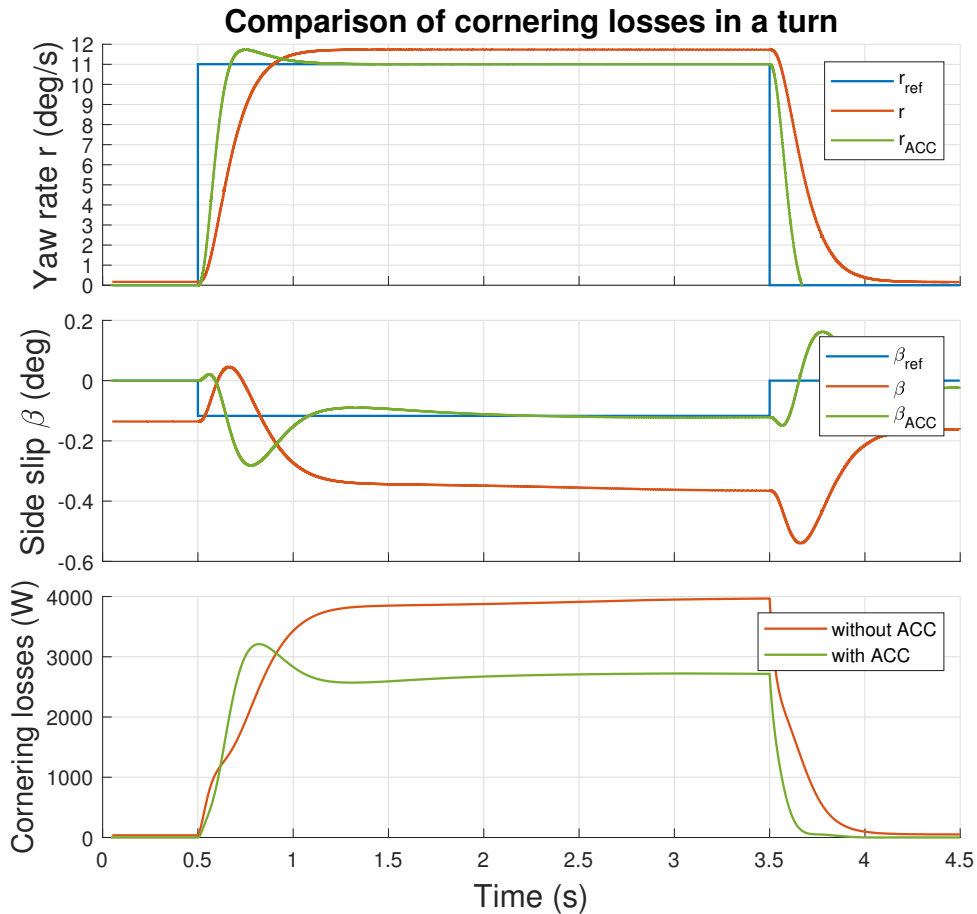


Figure 4.12: The example of the right turn with and without the ACC. The vehicle turns only with the front wheels $\delta_f = 5^\circ, \delta_r = 0^\circ$ and the velocity is $V_x = 54 \text{ km/s}$. The last graph compares the cornering losses. The vehicle with ACC is 45 % more efficient and consumes less energy through slip.

Chapter 5

Validation

The next chapter will focus on the validation procedures of the controllers derived above. The Low-level and High-level controllers are going to be tested separately. First the robustness of each controller will be validated in the **Robustness testing** section. Then, the Low-level reference following is tested in section **Low-level reference testing** and the results for the High-level controllers are shown in **High-level reference testing**.

5.1 Robustness testing

The robustness is tested using the \mathcal{H}_∞ -norm and robust control synthesis framework. First, the model is simulated across the set of parameters defined by the boundary conditions in the **Parameters and control requirements** and linearized. Secondly, the bode plot of the linearized systems is created, which defines an envelope of uncertainties. The envelope is used to define a multiplicative uncertainty of the nominal system $G_{nom}(s)$ as:

$$G(s) = (1 + W_m(s)\Delta(s))G_{nom}(s), \quad (5.1)$$

where $G_{nom}(s)$ is the nominal system for which the controller is defined, $\Delta(s)$ defines the uncertainty as any transfer function such that $\|\Delta\|_\infty \leq 1$ (always stable), the $W_m(s)$ is the weighting transfer function that scales the uncertainty across frequencies. The chosen structure for the $W_m(s)$ is from [31], page 302:

$$W_m(s) = \frac{\tau s + r_0}{\tau/r_\infty s + 1}, \quad (5.2)$$

where $1/\tau$ is frequency where the relative uncertainty reaches 100%, r_0 is the steady state uncertainty and r_∞ the uncertainty level at higher frequencies after $1/\tau$.

Next, the plant model $P(s)$ of the uncertain system $G(s)$ is build with the controller $C(s)$, see Figure [5.1]. The $G(s)$ defines the uncertainty system as discussed in equation (5.1). The u_Δ and y_Δ are the outputs and inputs of the $\Delta(s)$ to and from the $G_{nom}(s)$. The y are the measured system variables used by the controller $C(s)$ to calculate appropriate actions u . The w are the reference inputs, disturbances or noise, and the z are the weighted or normalized controlled outputs, and generally the z is selected so that $z \rightarrow 0$. The z is used to objectify the performance obligations of the plant model.

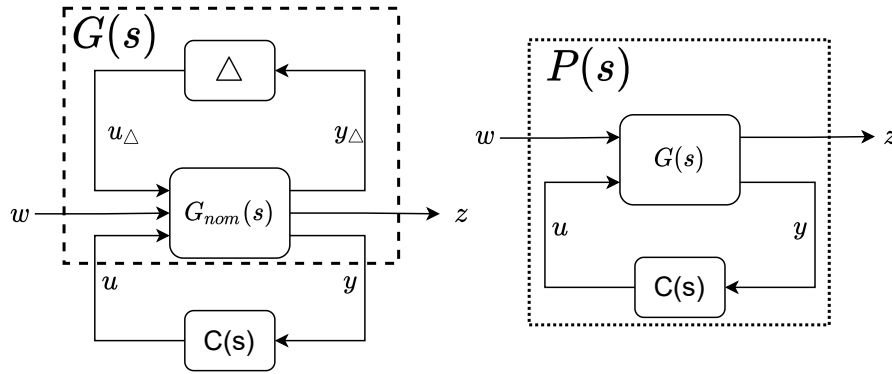


Figure 5.1: The general definition of the plant model $P(s)$.

To ensure that the plant behavior retains the set performance, a performance weight transfer function W_e is created as in [31], page 58:

$$W_e(s) = \frac{s/M + \omega_{BW}}{s + \omega_{BW} A}, \quad (5.3)$$

where ω_{BW} is the bandwidth frequency, A the steady state error and M the peak magnitude. The $W_e(s)$ weights and scales the controlled outputs z of the plant model $P(s)$.

Lastly, the \mathcal{H}_∞ -norm of the plant model $P(s)$ is calculated from w to the z . The $\|P(s)\|_\infty$ calculates the highest gain of the system as the supreme of the highest singular values $\bar{\sigma}$ from the whole frequency range $\omega \in \mathbb{R}$. It is formulated as:

$$\|P(s)\|_\infty = \sup_{\omega \in \mathbb{R}} \bar{\sigma}(P(j\omega)). \quad (5.4)$$

Whenever the $\|P(s)\|_\infty \leq 1$, the model is stable by the small gain theorem and retains the performance requirements set by $W_e(s)$. Note that the small gain theorem is a very strict requirement, and the system could be stable even if it would not be satisfied. The purpose is to show the system's core stability and robust performance.

5.1.1 Low-level controller

The nominal system $G_{nom}(s)$ is linearized from input d to output γ in the operation point:

$$\text{OP}_\gamma = 0, \quad (5.5)$$

$$\text{OP}_d = d_{max}/2. \quad (5.6)$$

The model parameters are defined in the boundary conditions as discussed in section **Parameters and control requirements** and table [2.1]. The parameter bounds for the Simscape model are:

1. Load: m (80 – 120)%.
2. Spring constant: k (90 – 110)%.
3. Damper coefficient: c (90 – 110)%.
4. Lower arm length: L_1 (80 – 100)%.

The set of linearized $G_{nom}(s)$ from the parameter bounds is shown in the bode plot in Figure [5.2].

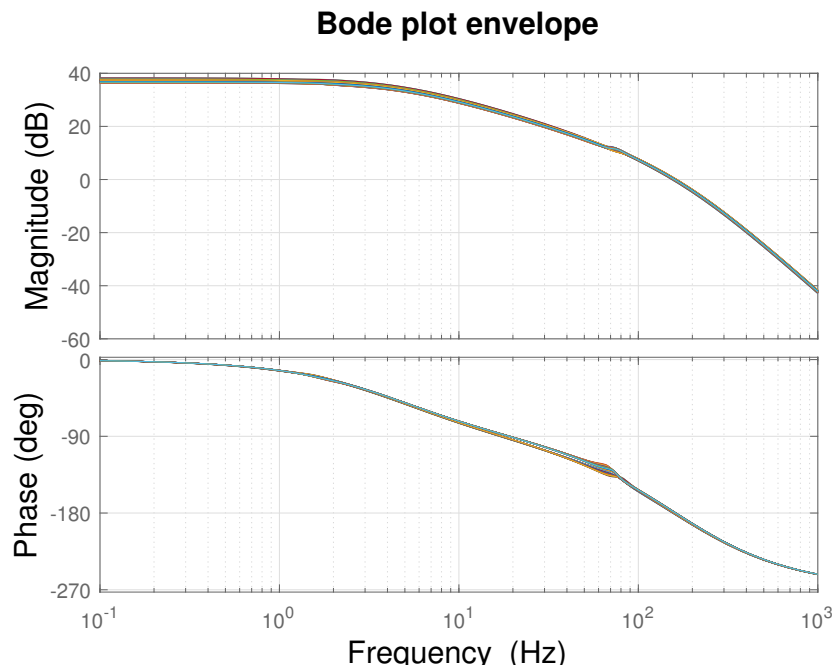


Figure 5.2: The bode plot envelope of the linearized set of the $G_{nom}(s)$ for the boundary conditions.

The bode plot envelope in Figure [5.2] can be used to define the weight transfer function of uncertainty $W_m(s)$ with parameters: $r_0 = 0.1$, $r_\infty = 0.6$ and $1/\tau = 200$ Hz. The estimated uncertainty envelope for the $G(s)$ is shown in Figure [5.3].

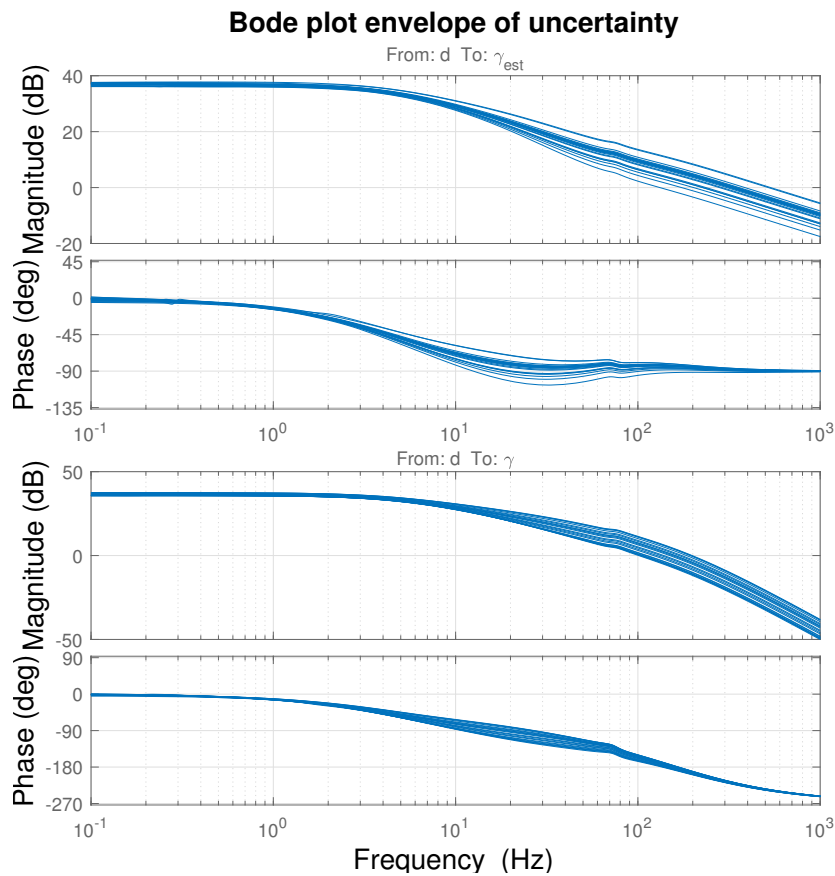


Figure 5.3: The bode plot envelope of uncertainties estimated from [5.2] that constitutes the $G(s)$ model.

The Low-level controller consists of non-linear mapping $F(u)$ and feedback PI controller. One way to think about $F(u)$ is that the $F(u)$ chooses an operating point for the system. It sets stroke length d such that the γ_{ref} is reached. Thus, $F(u)$ can be left out from the plant model because it holds no dynamics. The $G(s)$ model is linearized in the operating point! The plant can be seen in Figure [5.4]. The performance transfer function $W_e(s)$ is defined

with: $T_s = 1/29$ s, $OS = 1\%$, $M = 2$, $A = 0.05^\circ$ and the bandwidth by:

$$\zeta = \frac{-\ln(OS/100)}{\sqrt{\pi^2 + \ln^2(OS/100)}}, \quad (5.7)$$

$$\omega_{BW} = \frac{4}{T_s \zeta} \sqrt{(1 - 2\zeta^2) + \sqrt{4\zeta^4 - 4\zeta^2 + 2}} = 117.5 \text{ Hz}. \quad (5.8)$$

Note that the overshoot (OS) parameter does not check the actual overshoot of the response, but rather it chooses the bandwidth frequency. The overshoot limitation is captured by M , which defines peak gain in the bode plot. The settling time T_s is chosen to be the same as the time constant of the actuator.

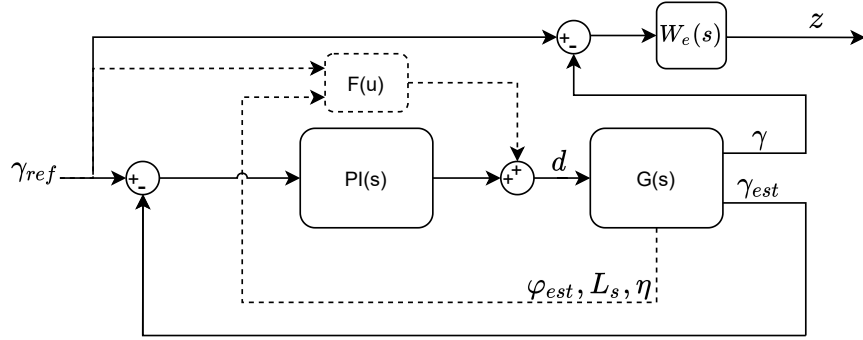


Figure 5.4: The Low-level controller plant model. The non-linear mapping $F(u)$ is left out.

The \mathcal{H}_∞ -norm of the Low-level controller with uncertainties defined by Figure [5.3] is

$$\|P(s)\|_\infty \leq 0.9627, \quad (5.9)$$

and the critical frequency is $f_c = 265.5$ Hz. The norm (5.9) is below 1 and thus the system is stable for all uncertainties and retains the performance defined by $W_e(s)$.

5.1.2 High-level controller

The twin track model is linearized from γ_f and γ_r to β , r and ϵ_v (calculated from (4.56)). The velocity tracking PI controller is created for τ_{ENG} input that tracks the parameter V_x so that the twin track model can be linearized at the given velocity. The PI controller is defined as:

$$PI_{V_x}(s) = \frac{100s + 20}{s} \quad (5.10)$$

The operation point (OP) is defined as:

$$\text{OP}_{\gamma_f} = 0 \text{ rad}, \quad (5.11)$$

$$\text{OP}_{\gamma_r} = 0 \text{ rad}, \quad (5.12)$$

$$\text{OP}_{V_x} = 15 \text{ m/s} = 54 \text{ km/h}, \quad (5.13)$$

$$\text{OP}_{\delta_f} = 0 \text{ rad}, \quad (5.14)$$

$$\text{OP}_{\delta_r} = 0 \text{ rad} \quad (5.15)$$

$$\text{OP}_{\tau_{BRK}} = 0 \text{ N m}. \quad (5.16)$$

The model parameters are defined in the boundary conditions as discussed in section **Parameters and control requirements** and table [2.1]. The parameter bounds for the twin track model are:

1. Load: m (80 – 120) %.
2. Road friction: $\mu = [0.3 \ 0.8 \ 1] = [\textit{snow wet dry}]$.
3. CG variation: $\Delta\text{CG} = \pm 15$ cm.
4. Velocity: $\langle 10, 150 \rangle$ km/h.

Nevertheless, the linearized nominal model $G_{nom}(s)$ contains also very slow dynamics modes (> 100 s). The purpose of High-level controller is to improve the response of the vehicle. The slow poles, that are dominant after 100 s, can be handled easily by the driver and are no concern for the robustness testing. Thus, the modes of the $G_{nom}(s)$ system are selected at frequencies $f = \langle 10^{-2}, \infty \rangle$ Hz.

The set of linearized $G_{nom}(s)$ from the parameter bounds is shown in the bode plot in Figure [5.5]. However, the magnitude of the uncertainty from the variation of the velocity is too high for the system to be robust, see Figure [5.5]. Nevertheless, the LQR gains can be scaled with the velocity which eliminates the velocity robustness requirement, see **Velocity dependent LQR**. Note that the velocity can still vary because the measurements may be imperfect, but these variations are already included in the bode plot envelope in Figure [5.6].

The uncertainty is estimated from Figure [5.2] with weight transfer function $W_m(s)$ with parameters: $r_0 = 0.4$, $r_\infty = 0.3$ and $1/\tau = 10$ Hz. The estimated uncertainty envelope of the $G(s)$ is shown in Figure [5.7].

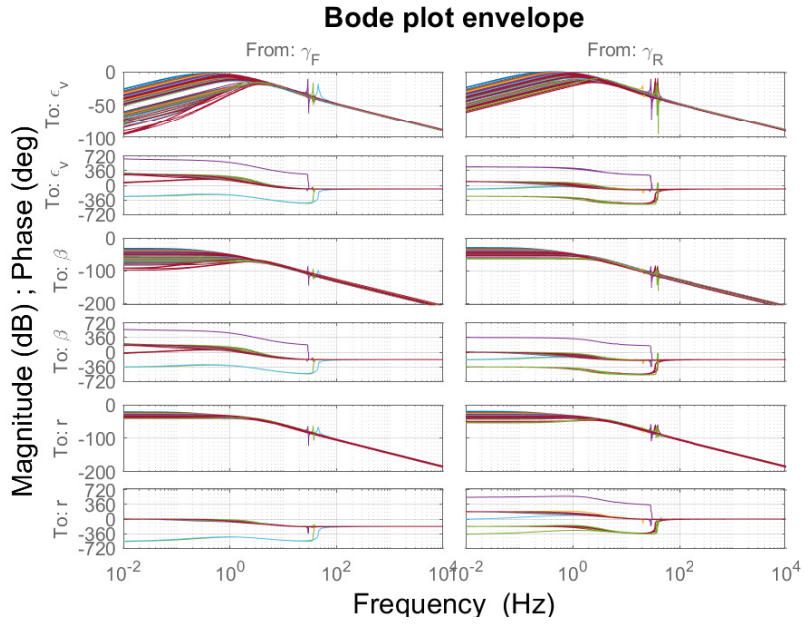


Figure 5.5: The bode plot envelope for the boundary conditions.

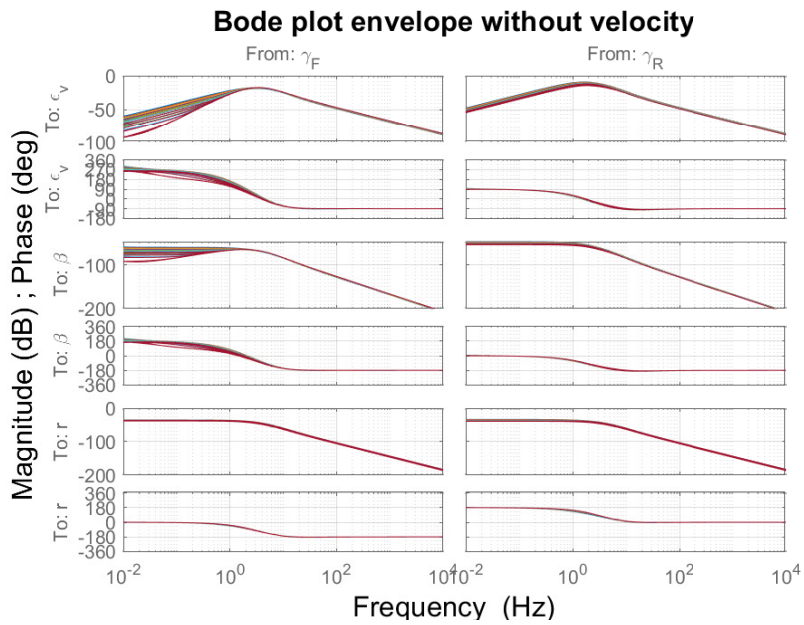


Figure 5.6: The bode plot envelope for the boundary conditions excluding velocity.

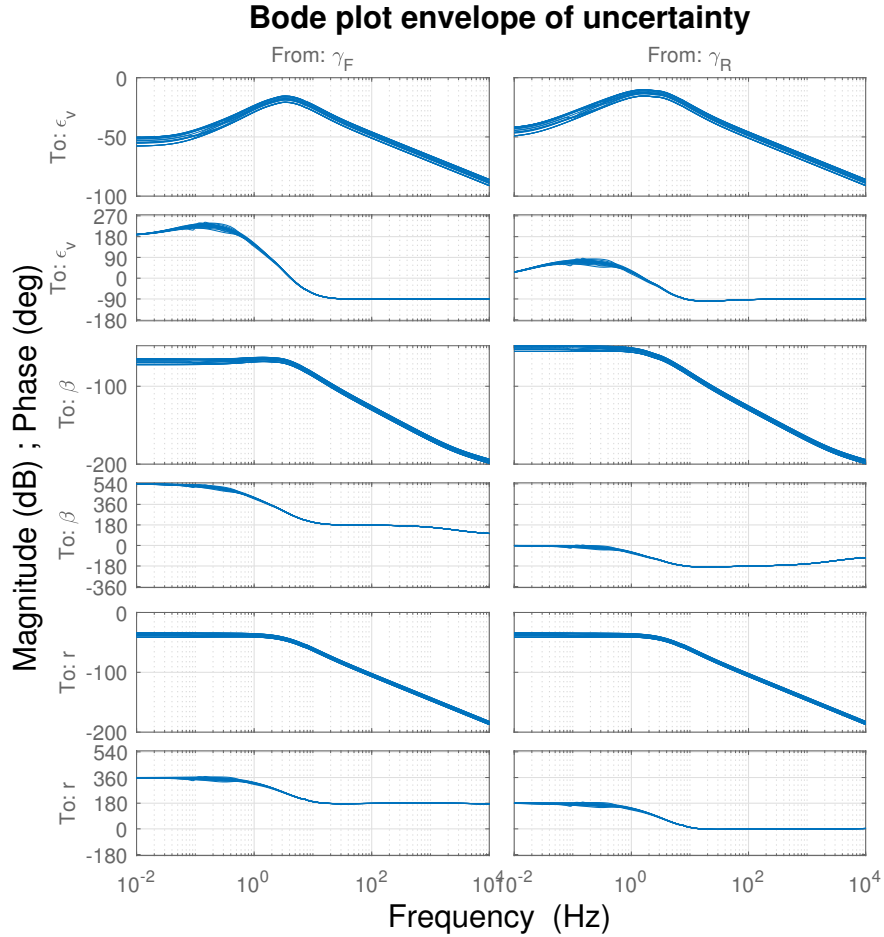


Figure 5.7: The bode plot envelope of uncertainties estimated from [5.2] that constitutes the $G(s)$ model.

■ LQR with β

The plant can be seen in Figure [5.8]. The performance transfer functions are defined with: $T_s = 1$ s, $OS = 10^{-6}$ %, $A = 0.1^\circ$, the bandwidth $\omega_{BW} = 2.7$ Hz calculated by equations (5.7) and (5.8) and the peak magnitude $M = 3$ for $W_{e_r}(s)$ and $M = 5$ for $W_{e_\beta}(s)$:

$$W_{e_r}(s) = \frac{s/M + \omega_{BW}}{s + \omega_{BW} A} = \frac{s/3 + 2.7}{s + 2.7 (0.1 \frac{\pi}{180})}, \quad (5.17)$$

$$W_{e_\beta}(s) = \frac{s/M + \omega_{BW}}{s + \omega_{BW} A} = \frac{s/5 + 2.7}{s + 2.7 (0.1 \frac{\pi}{180})}. \quad (5.18)$$

Note that the overshoot (OS) parameter does not check the actual overshoot of the response, but rather it chooses the bandwidth frequency. The overshoot limitation is captured by M , which defines peak gain in the bode plot. The settling time T_s is chosen to be at 1 s so that the plant guarantees it across the whole uncertainty range.

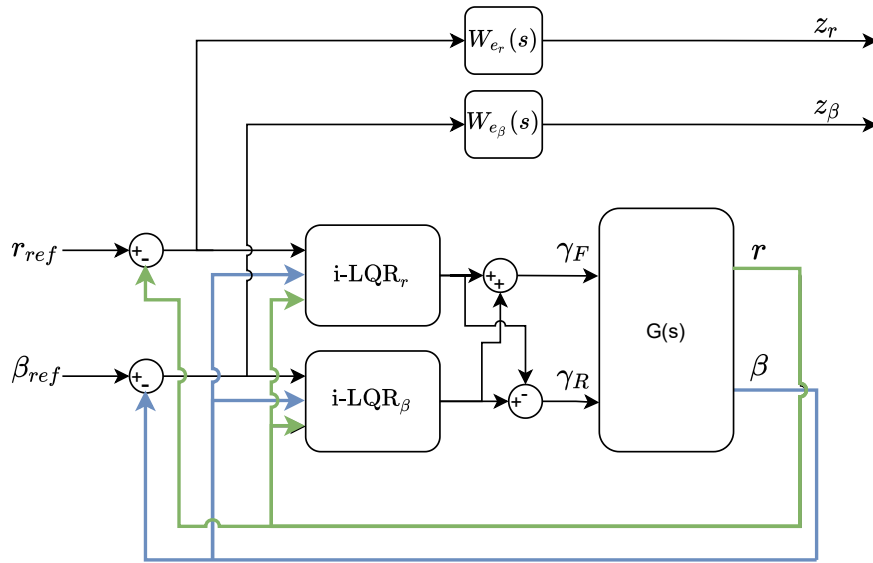


Figure 5.8: The High-level controller plant model with LQR using β .

The \mathcal{H}_∞ -norm of the High-level controller with β and uncertainties defined by Figure [5.7] is

$$\|P(s)\|_\infty \leq 0.9939, \quad (5.19)$$

and the critical frequency is $f_c = 0.3$ Hz. The norm (5.19) is below 1 and thus the system is stable for all uncertainties and retains the performance defined by the performance functions $W_{e_r}(s)$ and $W_{e_\beta}(s)$.

■ LQR with a_y

The plant can be seen in Figure [5.9]. The performance transfer functions are defined in (5.17) and (5.18) ($W_{e_{\epsilon_v}}(s) = W_{e_\beta}(s)$) but the magnitude peak is $M = 5.4$ in $W_{e_\beta}(s)$.

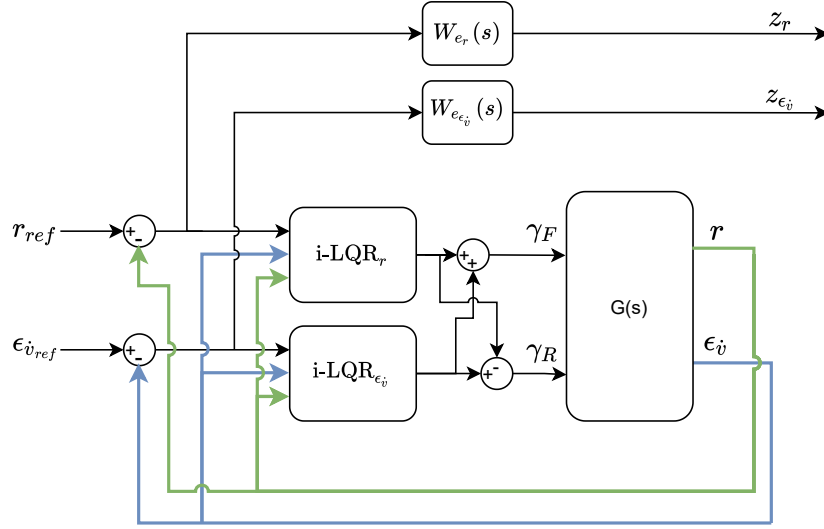


Figure 5.9: The High-level controller plant model with LQR using $\epsilon_{\dot{v}}$.

The \mathcal{H}_∞ -norm of the High-level controller with $\epsilon_{\dot{v}}$ and uncertainties defined by Figure [5.7] is

$$\|P(s)\|_\infty \leq 0.9948, \quad (5.20)$$

and the critical frequency is $f_c = 105.3$ Hz. The norm (5.20) is below 1 and thus the system is stable for all uncertainties and retains the performance defined by the performance functions $W_{e_r}(s)$ and $W_{e_{\epsilon_{\dot{v}}}}(s)$. To retain the same uncertainty resistance as **LQR with** β , the performance function of the $\epsilon_{\dot{v}}$ has to permit higher magnitude peaks.

■ Disturbance in the camber angle γ

The Low-level controller is responsible for maintaining the given γ_{ref} . However, whenever the configuration of the suspension is changed, for example, by ΔL_1 , the estimated camber angle γ_{est} will not be the same as the real γ and thus, the steady-state error will not be a zero. This can be captured as disturbance d_F and d_R in the camber angle inputs to the twin track model. The plant can be seen in Figure [5.10]. The controller follows reference $r_{ref} = 0$ and $\beta_{ref} = 0$. The disturbances in the γ_f and γ_r are defined as d_F and d_R respectively. The performance transfer functions are defined in (5.17) and (5.18).

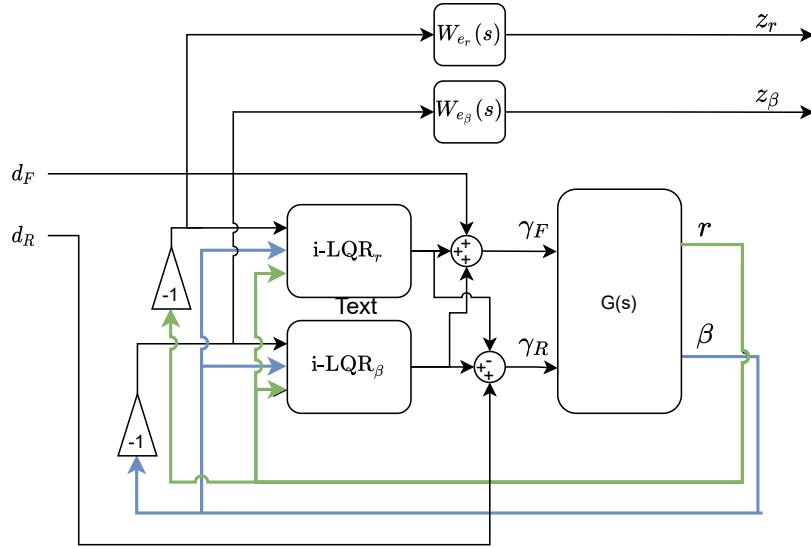


Figure 5.10: The High-level controller plant model with LQR using β for disturbance in γ_f and γ_r .

The \mathcal{H}_∞ -norm of the High-level controller with β and uncertainties defined by Figure [5.7] is

$$\|P(s)\|_\infty \leq 0.0395, \quad (5.21)$$

and the critical frequency is $f_c = 10.2$ Hz. The norm (5.21) is below 1 and thus the system is stable for all uncertainties and retains the performance defined by the performance functions $W_{e_r}(s)$ and $W_{e_\beta}(s)$. The norm value is very close to zero which gives almost complete immunity to the disturbances. The same resistance has the LQR with a_y , see **Camber angle disturbance**.

5.2 Low-level reference testing

The Simscape model is tested separately for the nonlinear mapping with and without the PI controller. They are both tested with the ramp of lateral force up to $F_{y_{axle}} = 6000$ N on the vehicle axle, and the camber is simultaneously excited with the step reference of $\gamma = \pm 4^\circ$ (left wheel and right wheel are tilted to the right). The F_y simulates the vehicle going through the corner, and the step reference the camber angles defined by the High-Level controller. The actuator dynamics are modeled with the rate limiter, transfer function, and saturation as shown in the respected controller diagrams in [3.13] and [3.23].

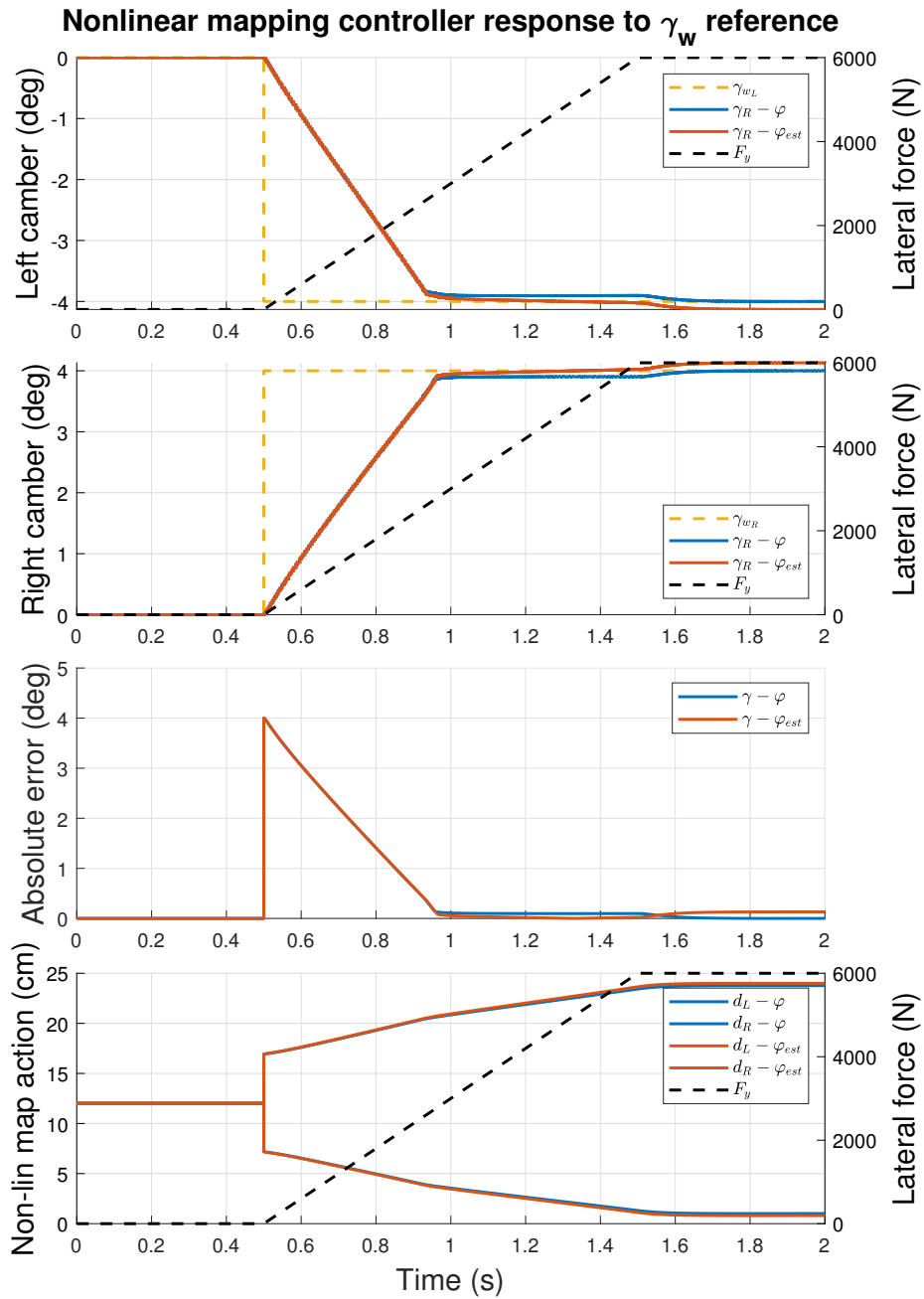


Figure 5.11: The step response of the nonlinear mapping controller using the real body roll angle and the estimated variant. The rate limiter has $\mu_{rate} = 18.5 \text{ cm s}^{-1}$ and the low-pass filter $\tau = 1/29$ second.

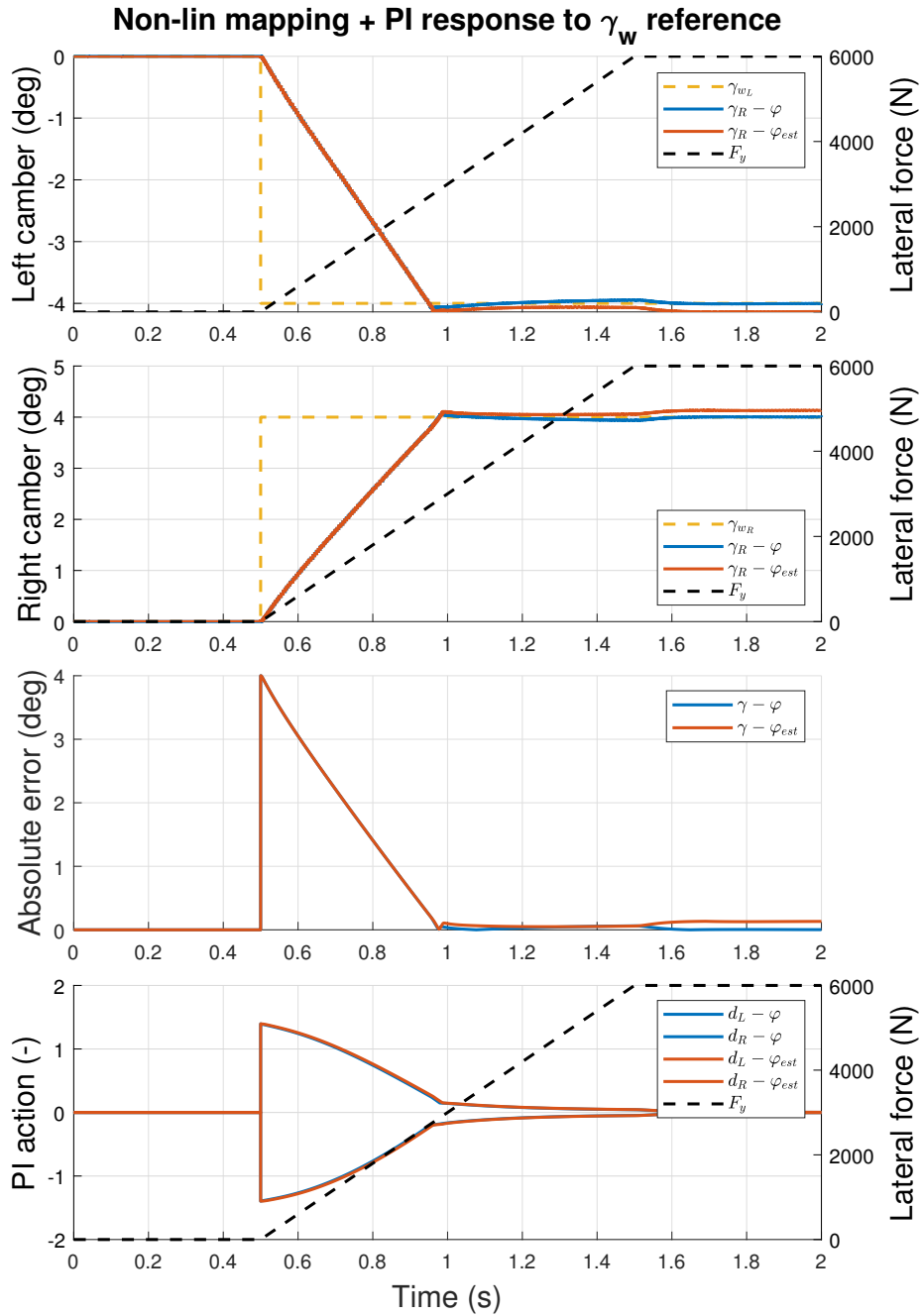


Figure 5.12: The step response of the close loop with the nonlinear mapping and PI controller using the real body roll angle and the estimated variant. The rate limiter has $\mu_{rate} = 18.5 \text{ cm s}^{-1}$ and the low-pass filter $\tau = 1/29$ second.

Both responses have steady-state error for the estimated roll angle that is caused by the inaccuracy of the linear regression of the camber-compensated estimator for the roll angle, see Figure [3.17]. The PI controller action goes down to zero when approaching steady-state in Figure [5.12]. This is expected behavior, given that the nonlinear mapping controller can find the exact value of the stroke length needed for the referenced camber angle. The feedback controller can lower the settling time because it increases the magnitude of the controller action. It is also robust to uncertainties in the η measurements because it does not use them. Note that the feedback controller can also be used without the nonlinear mapping controller if the η is unavailable.

5.2.1 Load variation effects

The **Robustness testing** proved the robustness of the control law to the load variation. This section will provide visualization of this effect, see Figure [5.13]. Most of the conventional vehicles use passive camber that helps to increase the cornering ability of the car. However, it decreases the contact patch area for the longitudinal maneuver like braking. The advantage of the ACC to passive approach is clearly seen in Figure [5.13]. The Low-level controller of the ACC is able to hold the 0 camber angle as instructed, which increases the contact patch area and available force to the maximum and decreases the braking distance, see **Friction circle development with camber**.

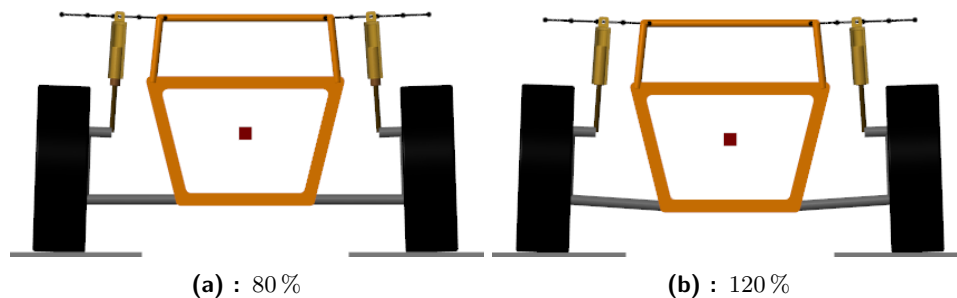


Figure 5.13: Load variation of the Simscape model with passive camber angle 2° .

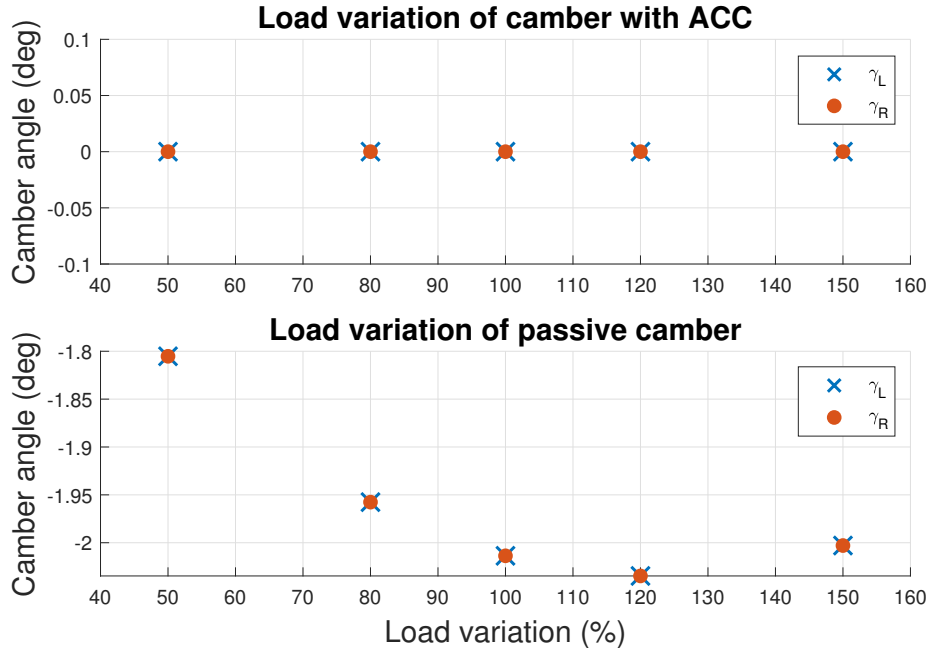


Figure 5.14: The comparison of passive camber angle with $\gamma = 2^\circ$ and Active Camber Control against the load variation of the axle.

5.3 High-level reference testing

The vehicle system is tested in multiple categories for both High-level controllers. The LQR with β is labeled with b and the LQR with a_y as a in the legend. The no subscript corresponds to the twin track response without the ACC. The dynamics of the actuator are only captured by transfer function with time constant $\tau = 1/29$ s and the saturation $\langle -9.7^\circ, 9.7^\circ \rangle$. The rate limiter is left out so that the response plots are simpler to read. Note that the rate limiter would have minimal influence on the response dynamics because both controllers use the back-calculation method for the anti wind-up.

The vehicle parameters are defined in the table [2.1]. However, the vehicle CG position is moved to the front by 10 cm so that the car is understeering, which changes L_f and L_r parameters. Most of the vehicles are understeering by construction, and the CG off-center creates a linkage between the sideslip angle and the yaw rate dynamics, which would not be in the neutral car. Note that the understeering and oversteering vehicles have passive side slip angle β value, which cannot be regulated with the LQR with a_y and the camber sign notation is defined differently, see **Design**.

5.3.1 External disturbance

The vehicle is tested with the duplet disturbance in the $M_{z\text{-ext}}$ and $F_{y\text{-ext}}$, see Figure [5.15]. The $M_{z\text{-ext}}$ is used to create yaw rate disturbance r_d with equation

$$M_{z\text{-ext}} = 10 r_d I_{zz}, \quad (5.22)$$

and the $F_{y\text{-ext}}$ creates the side slip angle disturbance β_d as:

$$F_{y\text{-ext}} = 10 \tan(\beta_d) V m, \quad (5.23)$$

where $I_{zz} = J$, m are defined in table [2.1] and the $V = 15$ m/s.

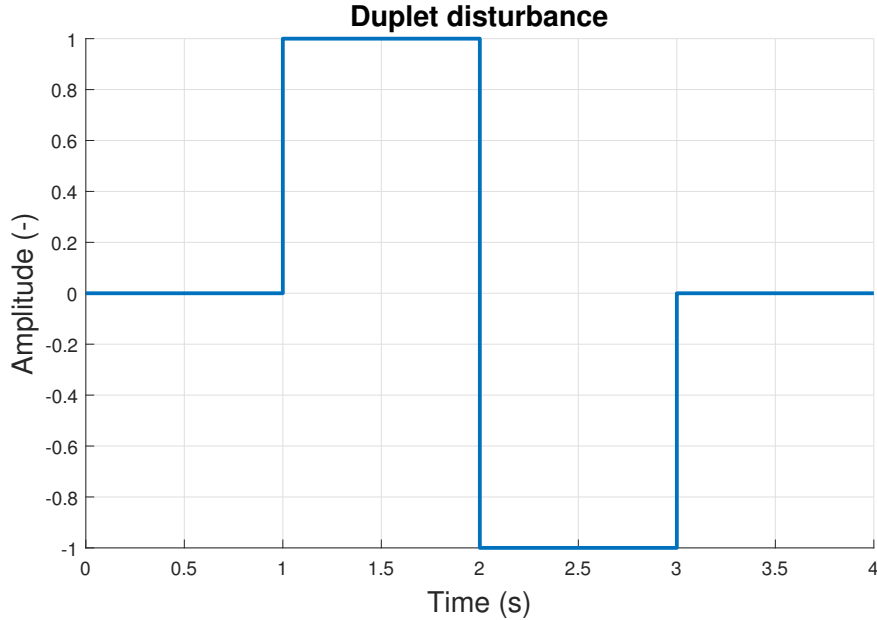


Figure 5.15: The duplet disturbance signal for the yaw rate and side slip angle.

The vehicle speed is kept constant at constant V_x with the simple PI controller in (5.10) and the reference is set by $\delta_f = \delta_r = 0$ as $\beta_{ref} = \epsilon \dot{v}_{ref} = r_{ref} = 0$.

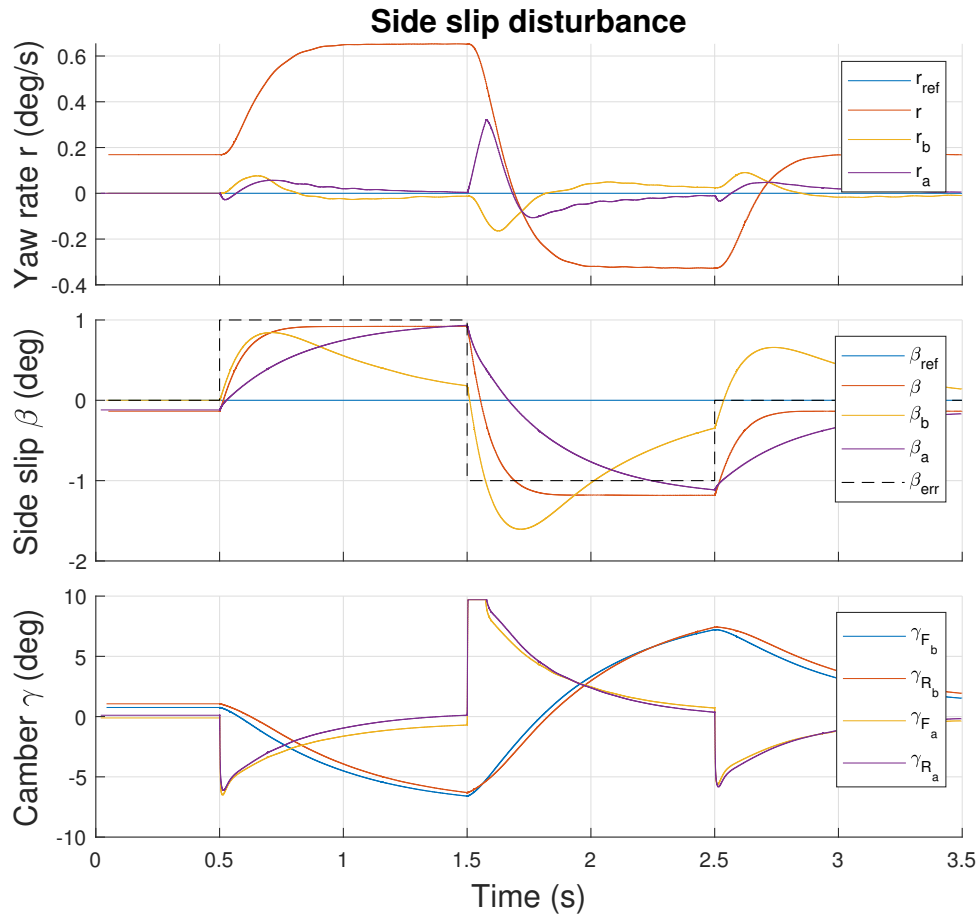


Figure 5.16: The side slip angle disturbance with duplet with amplitude $\beta_d = 2^\circ$.

The yaw rate disturbance response is very similar for both controllers except the camber angles, which seem different, but remember that the LQR with β also compensates the passive β angle, and the camber angles are shifted. On the other hand, the sideslip angle disturbance is very different. The LQR with a_y slows down the rise time of the disturbance significantly, while the LQR with β focuses on the steady-state value and minimizes the error.

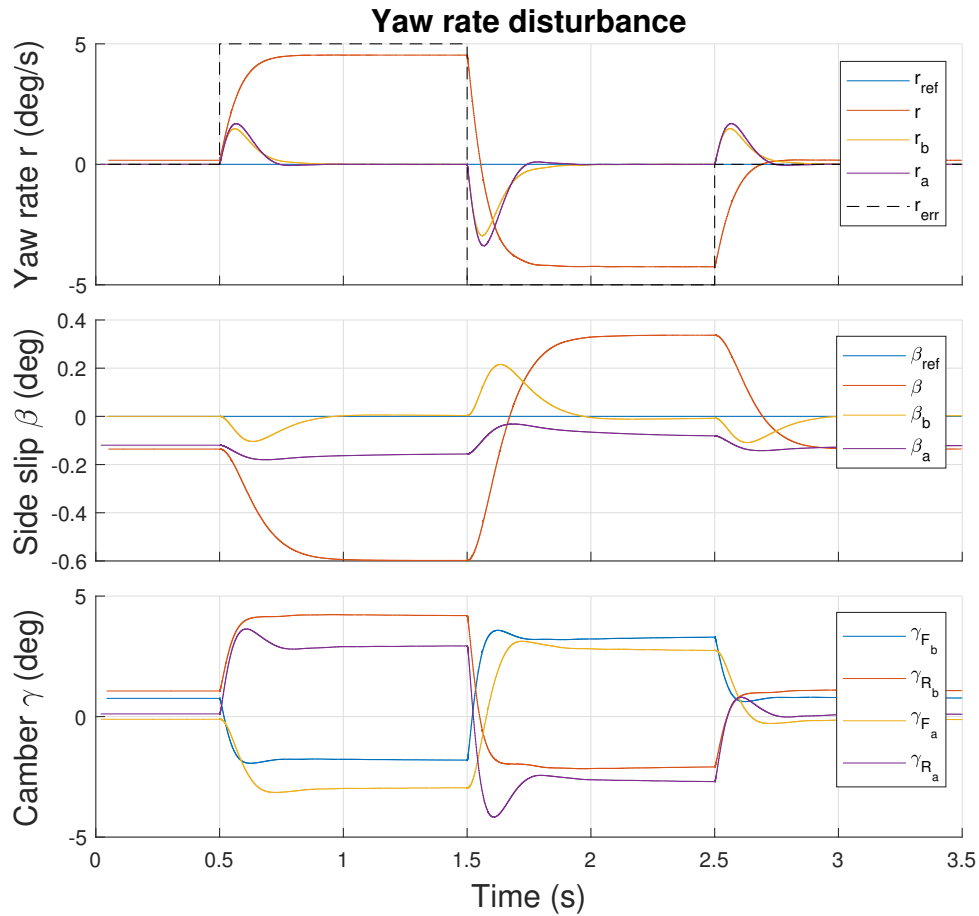


Figure 5.17: The yaw rate disturbance with duplet with amplitude $r_d = 5^\circ$.

5.3.2 Step response

The vehicle step response to the input command of $\delta_f = 2^\circ$ and $\delta_r = \pm 2^\circ$ for the side slip angle and yaw rate respectively is captured in Figures [5.18] and [5.19]. The speed is kept constant at V_x with simple PI controller in (5.10).

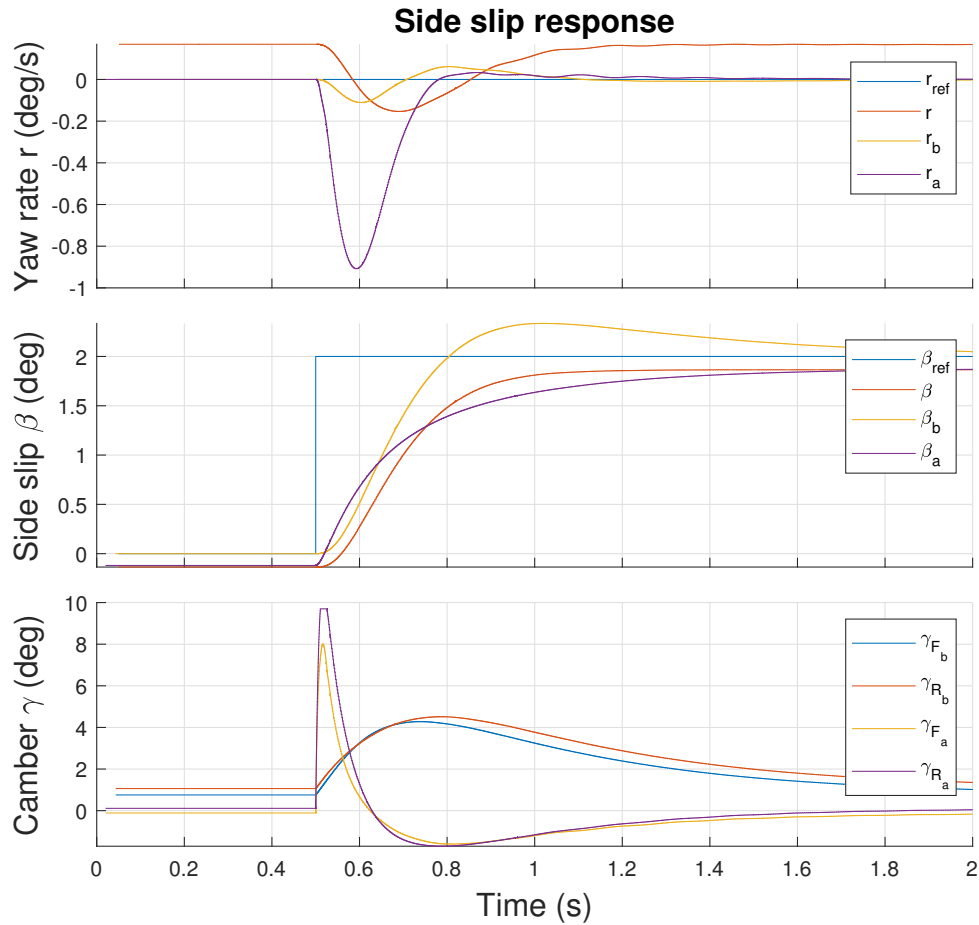


Figure 5.18: The step response to the input command $\delta_f = \delta_r = 2^\circ$.

The step response is very similar for both controllers' yaw rates, but the LQR with β has a shorter settling time. The same goes for the sideslip angle response, but the LQR with a_y has a faster rise time because it uses acceleration. Nevertheless, when the acceleration diminishes, the camber angles drop down and even go in the opposite direction. Also, the LQR with a_y cannot follow the β_{ref} with zero steady-state error, but, on the other hand, the LQR with β does.

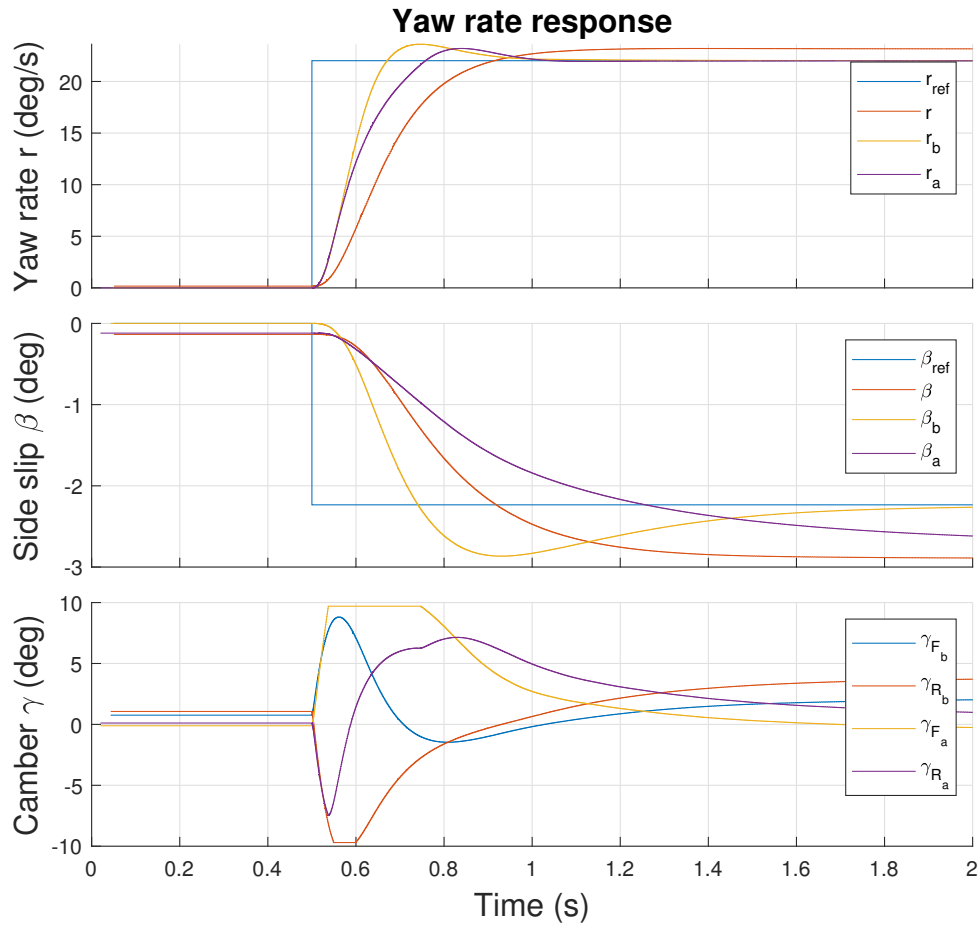


Figure 5.19: The step response to the input command $\delta_f = 2^\circ$ and $\delta_r = -2^\circ$.

5.3.3 Steering disturbance

The steering disturbances simulates the jamming of the steering or the damage to the steering knuckle for the front and rear separately, see Figure [5.20] and [5.21]. The speed is kept constant at constant V_x with simple PI controller in (5.10) and the input command is $\delta_f = \delta_r = 0^\circ$.

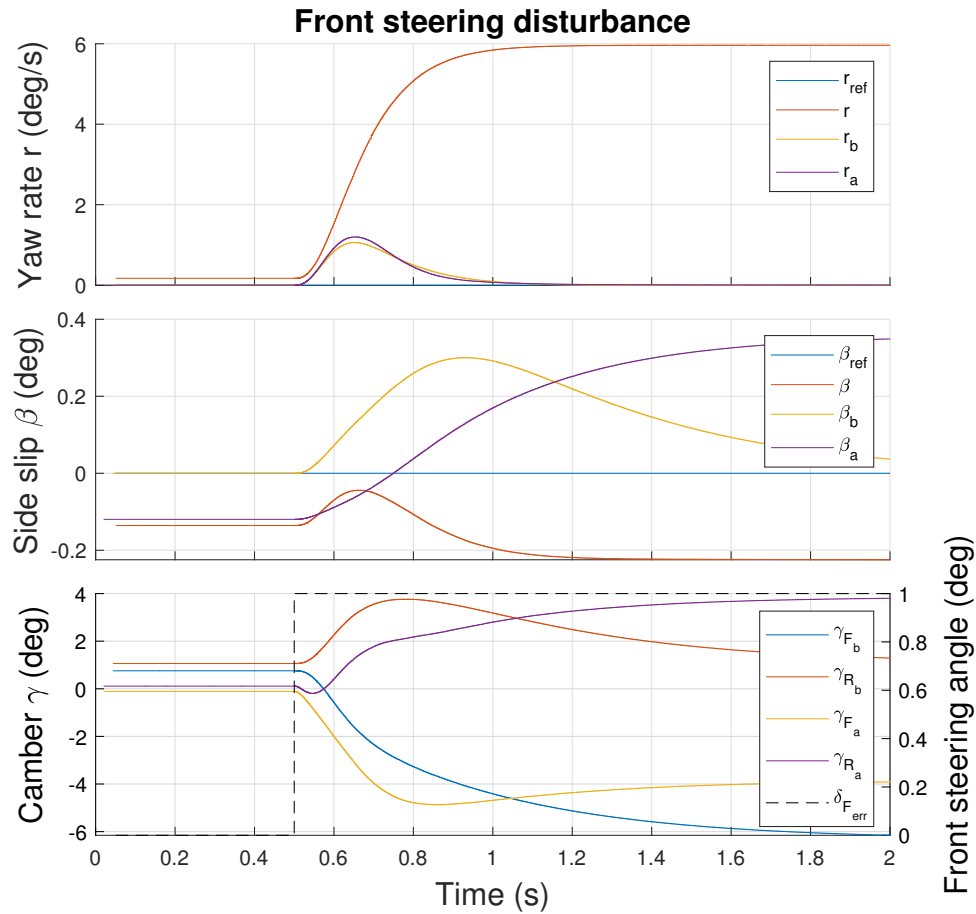


Figure 5.20: The front steering disturbance response with $\delta_{f_{err}} = 1^\circ$.

Both controllers prioritize yaw rate reduction. However, the LQR with β can restore the vehicle behavior and minimize the side slip angle disturbance value. The LQR with a_y cannot because it uses only the accelerometer, and the steady-state error is non-zero.

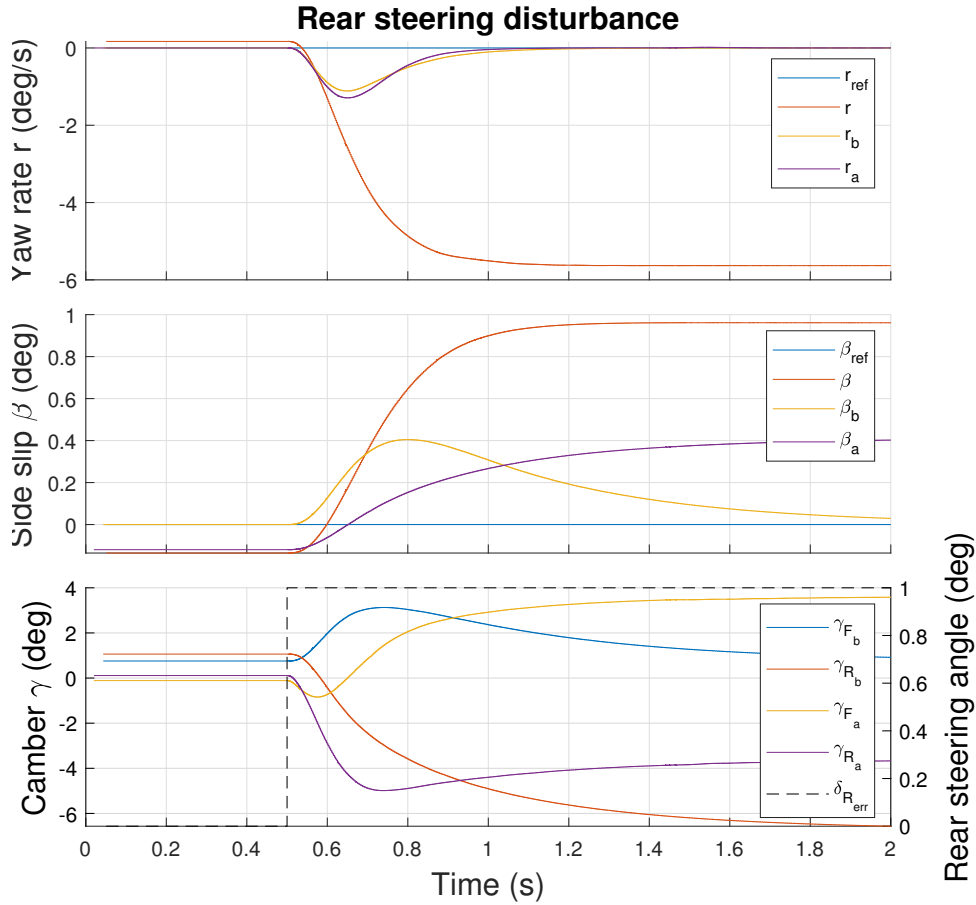


Figure 5.21: The rear steering disturbance response with $\delta_{r_{err}} = 1^\circ$.

5.3.4 Camber angle disturbance

The Low-level controller might have steady state error due to the configuration changes in the suspension like ΔL_1 . The response of the High-level controllers to the front camber angle disturbance is captured in Figure [5.22]. The vehicle speed is kept constant at constant V_x with simple PI controller in (5.10) and the reference is set by $\delta_f = \delta_r = 0$ as $\beta_{ref} = \epsilon \dot{v}_{ref} = r_{ref} = 0$.

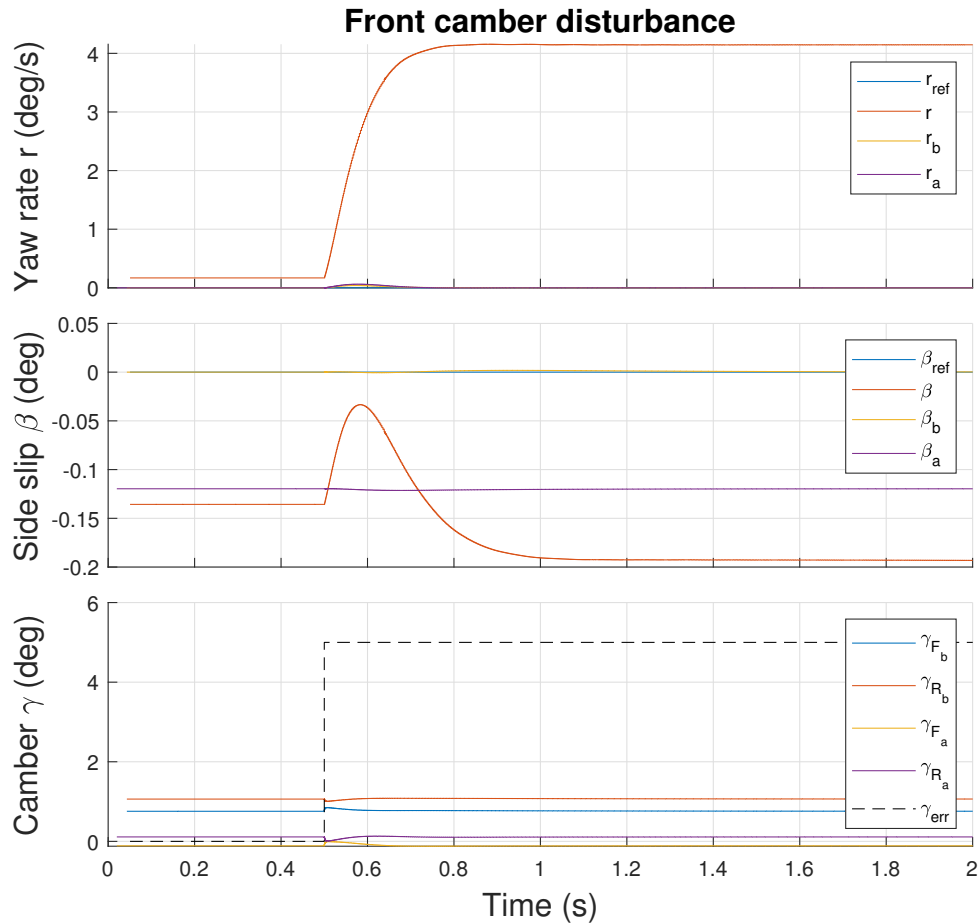


Figure 5.22: The response of the system to the front camber angle disturbance $\gamma_{fa} = 5^\circ$.

Based on the Figure [5.22], both High-level controllers are able to withstand the disturbance which corresponds to the findings in the **Disturbance in the camber angle γ** .



Chapter 6

Conclusion

The thesis presents an Active Camber Control that can be implemented in conventional cars without specialized sensors or equipment. It operates without the driver's intervention and awareness and enhances the cornering stability, maneuverability, active safety, and overall performance of the vehicle. The ACC is divided into Low-level and High-level controllers. The Low-level controller is responsible for realizing the referenced camber angles. It can fully estimate and control the camber angle throughout different suspension configurations and disturbances. The High-level controller manages the camber angles so that the reference calculated from the driver input is met. There are presented two types of the double i -LQR High-level controllers. The first one uses the sideslip angle and the yaw rate states. The second uses the yaw rate and the lateral acceleration instead, aiming to circumvent the sideslip angle because it is difficult to measure directly. The High-level controller is able to increase the maximal lateral acceleration of the vehicle by 25%. The cornering losses are also decreased as expected because the ACC uses smaller tire slip angles to achieve the same lateral forces. The natural benefit of the camber control is that the vehicles with the ACC can reach higher longitudinal forces because the wheels use more efficiently the contact patch by keeping the camber angle at 0 degrees thorough-out the different load variations on the axles. Also, the vehicle with ACC does not need the negative passive camber, which lowers the effective contact patch area because it can change it actively. Additionally, the LQR with the lateral acceleration can considerably dampen the disturbances like a wind gust.

The **chapter 2** defines the problem of the camber actuation and **analysis of camber kinematics and its influence on vehicle dynamics**. It first defines the camber angle and its dependency on other suspension parameters. Then, it establishes the models used to predict the force development from the camber angle and compares them to the models of the tire slip angles

that are used in the conventional chassis. The camber angle models are then linearized to be used in the single and twin track model theory. Next, the camber actuation requirements are postulated. They define the set of boundary conditions the vehicle will be operating in. Finally, the requirements are transformed into the model specifications, and the camber actuation arrangement is laid out.

The **chapter 3** sets up the **analyze of mechatronic system of camber actuation** and the Low-level controller. The camber actuation is analyzed in terms of the range, response time, and force requirements. They constitute the resultant actuator specifications that are compared to the commercially available variant. The Low-level controller is specified in the framework of the kinematic geometry model of the McPherson suspension. The body roll is estimated in this framework as the difference between the left and right length of the spring-dampers and camber angles. Then, the geometry model with the estimated body roll is used to estimate the camber angle of the wheel. The kinematic problem of the presented geometry model can be solved algebraically, and it is constituted in the nonlinear mapping. To increase the robustness and performance of the nonlinear mapping controller, a PI controller is introduced into the close loop of the system. The estimation of the camber angle is further evaluated for the influence of the steering angles, and the particular equations describing the effects are presented.

The **chapter 4** concludes the **development of the chassis control algorithm for camber active system** where the High-level controllers are defined. The reference signals for both controllers are derived first. Then, the double i -LQR structure is presented separately for the LQR with the sideslip angle and the LQR with the lateral acceleration. The sideslip angle cannot be directly measured, and its estimation is imprecise. Thus, it is not a suitable state variable. That is why a second LQR that uses lateral acceleration measurement instead of sideslip angle is developed. The twin track model is used to confirm the authenticity of the active camber control where the maximal lateral acceleration of the vehicle is increased by 25% with ACC. The ACC can also be used to model match the twin track vehicle to other models with different oversteering and understeering dynamics.

The **chapter 5** is dedicated to the **validation of the developed algorithms**. The Simscape model for the Low-level and twin track model for the High-level controller are linearized across the set of the boundary conditions, which constitutes the envelope of uncertainties that the controllers can be subjected to. The small gain theorem is used to confirm the performance and stability retention of the close loop systems. The second part focuses on the reference tracking of the controllers. The Low-level controller is subjected

simultaneously to the side force and step reference, and the disturbance rejection to load variation is also tested. The High-level controller is tested in multiple fields. The disturbances tests are created with the duplet signal, chosen intentionally to test the dynamical responses. The LQR controller with the sideslip angle can withstand the disturbances. However, the LQR with the lateral acceleration only dampens the disturbance and has non-zero steady-state error, which can be beneficial because it prioritizes the stabilization of the vehicle to the steady-state value, which the driver can correct. The tests also involve the step responses to the driver input step reference. The controllers fair almost the same for the yaw rate. However, the LQR with acceleration has a non-zero steady-state sideslip angle error, and its camber actuation magnitude might be too excessive. The last tests involve the steering angle disturbances where both controllers lower the disturbance effects. However, the LQR with the acceleration has non-zero steady-state sideslip angle errors. The disturbance of the front camber angle is completely reduced.

All of the Master thesis assignment topics are satisfied and addressed in the chapters above.

■ 6.1 Future work

Future work will focus on developing a more concise High-level controller like MPC and validating the simulation results of the proposed algorithms in the real world, which was not possible due to the COVID-19 pandemic yet.

Appendix A

Nomenclature

Table A.1: CTU demonstrator vehicle nomenclature list. The nominal units are used in all equations and derivations.

Symbol Abbreviation	Nominal unit	Definition
SA	-	steering axis
CG	-	center of gravity
ACC	-	Active Camber Control
4WS	-	4-wheel steering
DLC	-	Double Lane Change maneuver
KPI	-	king-pin inclination
IR	-	installation ratio
OS	-	overshoot
OP	-	operating point
<i>CL</i>	-	complementary filter
L_1	m	length of the lower control arm
L_2	m	length of king-pin + ball joint
L_w	m	wheel mount in the king-pin measured from the ball joint
L_s	m	length of the McPherson strut
d	m	stroke length of the actuator

Symbol Abbreviation	Nominal unit	Definition
σ_{shf}	rad	angle of the McPherson strut from the king-pin plane
σ_{SA}	rad	angle of the SA from the king-pin plane
η	rad	angle of lower control arm to the vehicle wheelbase
θ	rad	angle of lower control arm to the horizontal ground
ϕ_f	rad	caster angle at the front suspension
ϕ_r	rad	caster angle at the rear suspension
k_f	N/m	front spring constant
k_r	N/m	rear spring constant
L_{sn}	m	spring natural length
c	N/m/s	damping coefficient
m	kg	vehicle mass
R_o	m	unloaded tire radius
R_i	m	rim radius
T_w	m	tire width
L_f	m	longitudinal distance of CG from the front axle
L_r	m	longitudinal distance of CG from the rear axle
w_f	m	lateral distance of CG from the vehicle side at the front axle
w_r	m	lateral distance of CG from the vehicle side at the rear axle
h_{CG}	m	height of vehicle CG
P_M	W	motor power on each wheel
T_{max}	N m	maximal torque of the motor
G_r	-	gear ratio
τ	s	motor time constant
I_{xx}	kg m ²	moment of inertia around CG X axis

Symbol Abbreviation	Nominal unit	Definition
I_{yy}	kg m ²	moment of inertia around CG Y axis
I_{zz}	kg m ²	moment of inertia around CG Z axis
J	kg m ²	moment of inertia around CG Z axis
C_{α_f}	N/rad	front cornering stiffness for one wheel
C_{α_r}	N/rad	rear cornering stiffness for one wheel
C_{γ_f}	N/rad	front camber cornering stiffness for one wheel
C_{γ_r}	N/rad	rear camber cornering stiffness for one wheel
δ_f	rad	front steering angle
δ_r	rad	rear steering angle
γ_f	rad	front camber angle
γ_r	rad	rear camber angle
α_f	rad	front slip angle
α_r	rad	rear slip angle
β	rad	side slip angle
V_x	m/s	constant longitudinal velocity
v	m/s	velocity
v_x	m/s	longitudinal velocity in X direction
v_y	m/s	lateral velocity in Y direction
a_x	m/s ²	longitudinal acceleration in X direction
a_y	m/s ²	lateral acceleration in Y direction
a_c	m/s ²	centripetal acceleration
g	m/s ²	gravitational acceleration
F_x	N	longitudinal force in X direction
F_y	N	lateral force in Y direction
F_z	N	vertical force in Z direction
F_t	N m	camber thrust force

Symbol Abbreviation	Nominal unit	Definition
M_x	N m	torque around X axis
M_y	N m	torque around Y axis
M_z	N m	torque around Z axis
φ	rad	roll angle
ψ	rad	yaw angle
$\dot{\varphi}$	rad/s	roll rate
r	rad/s	yaw rate
R	m	radius of a turn
K_φ	-	Roll estimation gain
K_r	-	LQR state-feedback gain for yaw rate
K_β	-	LQR state-feedback gain for side slip angle
K_{ϵ_i}	-	LQR state-feedback gain for yaw rate ϵ_i

Appendix B

Calculation of the installation ratio IR

The installation ratio is the ratio between the distance a and b , see Figure [B.1]. The McPherson suspension defines the distance a between the lower arm mounting point and the constant patch center of the wheel. The distance b is between the lower arm mounting point and the intersection of the spring-damper axis and the distance a line. The installation ratio is:

$$\text{IR} = \frac{b}{a} = 0.62. \quad (\text{B.1})$$

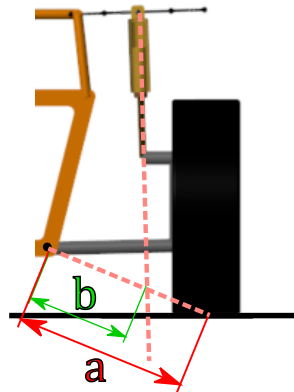


Figure B.1: The calculation of the IR for the McPherson suspension.

The installation ratio for the double wishbone suspension is calculated in the same way but generally the spring-damper is mounted directly to the lower arm and thus the a distances are to the wheel center and not to the center of the contact patch.

Appendix C

Derivation of McPherson suspension parameters

This section tackles the derivation of the L_x , L_2 and Ω_C McPherson parameters from the given parameter set of the suspension dimensions. Most of the suspension dimension parameters are always measured in the SA. The practical set of the parameters is shown in table [C.1]. The parameters are also depicted in the Figure [C.1].

Table C.1: The practical set of McPherson suspension parameters

Symbol	Value	Units	Definition
L_1	38	cm	length of the lower control arm
L_w	11.5	cm	wheel mount for the king-pin - measured from king-pin mounting point to the lower arm
σ_{shf}	2	<i>deg</i>	angle of the McPherson strut to the king-pin base
L_{shf}	9	cm	distance of the McPherson strut closest point to the king-pin projected onto the lower arm
$d_0 = L_{sSA}$	45	cm	McPherson strut length in the SA axis
$d_1 = L_{2SA}$	26.5	cm	king-pin length in the SA axis

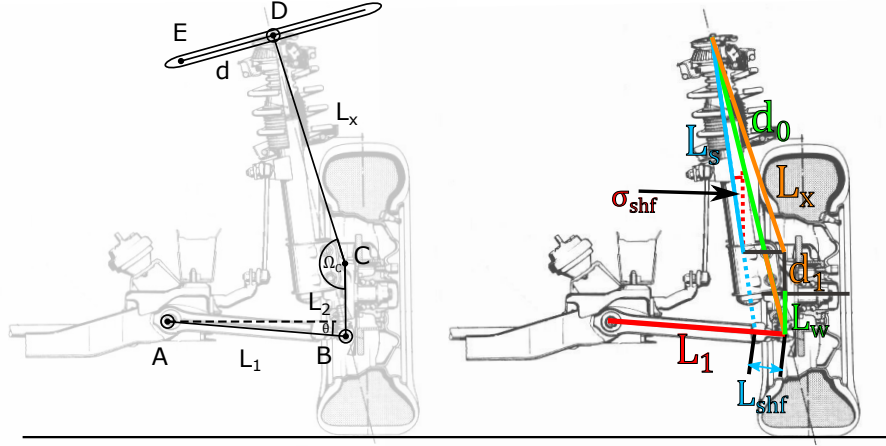


Figure C.1: The diagram of the McPherson parameters from table [C.1].

First, the angle of the SA has to be established so that the L_2 can be defined. The left Figure [C.2] shows the triangle used for the derivation of the equation (C.3). The $\angle B_1C_1A_1$ is obtained with the sine rule and the $\angle A_1B_1C_1$ has to sum up to 180° :

$$\angle C_1A_1B_1 = \arcsin \left(\frac{L_{shf}}{d_0 + d_1} \sin \left(\frac{\pi}{2} + \sigma_{shf} \right) \right), \quad (C.1)$$

$$\sigma_{SA} = \frac{\pi}{2} - \left[\pi - \left(\frac{\pi}{2} + \sigma_{shf} \right) - \angle C_1A_1B_1 \right], \quad (C.2)$$

$$\sigma_{SA} = \sigma_{shf} + \angle C_1A_1B_1. \quad (C.3)$$

With equation (C.3), the L_2 is calculated as follows

$$L_2 = d_1 \cos(\sigma_{SA}). \quad (C.4)$$

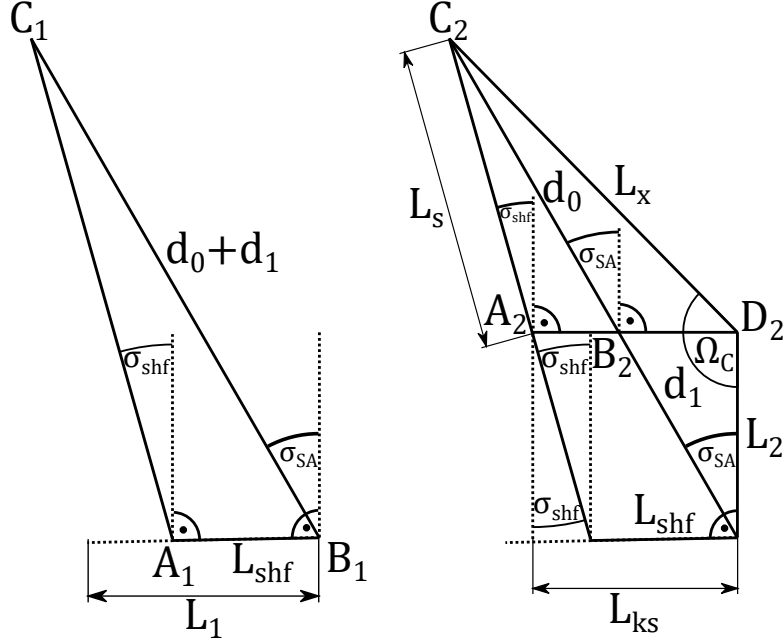


Figure C.2: The triangles from Figure [C.1] used for the derivation of parameters.

Next, the L_x and Ω_C is derived. The length of the shift L_{ks} of the mounting point of the McPherson strut from the king-pin can be calculated from the right triangle in Figure [C.2] with:

$$L_{ks} = L_2 \tan(\sigma_{shf}) + L_{shf}. \quad (C.5)$$

Also, the current length of the McPherson strut L_s is obtained from $\triangle A_2 B_2 C_2$ with cosine rule in right Figure [C.2] as:

$$L_s = \sqrt{d_0^2 + (L_{ks} - d_1 \sin(\sigma_{SA}))^2 - 2 d_0 (L_{ks} - d_1 \sin(\sigma_{SA})) \cos\left(\frac{\pi}{2} - \sigma_{SA}\right)}. \quad (C.6)$$

The L_x is derived in the same way as the L_s by cosine formula from $\triangle A_2 D_2 C_2$:

$$L_x = \sqrt{L_s^2 + L_{ks}^2 - 2 L_{ks} L_s \cos\left(\frac{\pi}{2} + \sigma_{shf}\right)}. \quad (C.7)$$

Finally, the Ω_C is defined with the sine rule from $\triangle A_2 D_2 C_2$:

$$\Omega_C = \frac{\pi}{2} + \arcsin\left(\frac{L_s}{L_x} \sin\left(\frac{\pi}{2} + \sigma_{shf}\right)\right). \quad (C.8)$$

Note that both the Ω_C and the L_x depends on the length of the McPherson strut L_s which is the only parameter that is constantly varying.

Appendix D

Derivation of the McPherson geometry model for the left side

The left side McPherson geometry model is derived in the same manner as the right side. Thus, many of the equations from the right side will be utilized here without explanation so it is recommended for the reader to go through the right side derivations first. The left side affects equations in the three sections shown below that are purposely named the same as for the right side.

D.1 Forward kinematics

The forward kinematics diagram depicted in Figure [3.11] is vertically mirrored for the left side. The points A and E are known by default where A is assumed as the center of the coordinate system. Thus, the point E has to be rotated by roll angle φ around point A as shown in equations (3.23) and (3.24). Also, the point B is defined as in (3.25). However, note that the θ is defined from the right to the left, see Figure [D.1]. Thus, it should be:

$$\theta = \pi - \theta_m, \quad (\text{D.1})$$

where θ_m is the theta measured for the left side. Based on the Figure [D.1], the forward kinematics for the camber angle γ can be calculated as:

$$\gamma = \Lambda_{BE} + \Gamma_B + \Omega_B - \frac{\pi}{2}, \quad (\text{D.2})$$

where Λ_{BE} , Γ_B , Ω_B , $|\text{BD}|$ and $|\text{EB}|$ are calculated with the formulas in (3.27), (3.28), (3.29), (3.30) and (3.31) respectively.

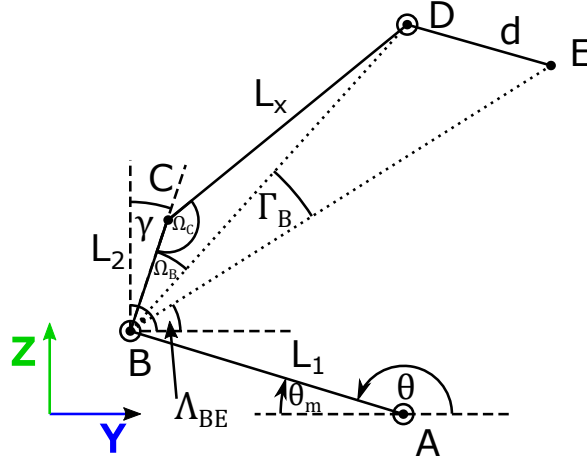


Figure D.1: Forward kinematics for camber angle γ for the left side geometry model of the McPherson suspension.

D.2 Control law: Nonlinear mapping

The equation (D.2) is used to derive the control law for the left side. The γ can be denoted as γ_w and d is the unknown:

$$\gamma_w = \Lambda_{BE} + \Gamma_B(d) + \Omega_B - \frac{\pi}{2}, \quad (\text{D.3})$$

and by solving for d :

$$\Gamma_B(d) = \gamma_w - \Lambda_{BE} - \Omega_B + \frac{\pi}{2}, \quad (\text{D.4})$$

$$\frac{|\text{BE}|^2 + |\text{BD}|^2 - d^2}{2|\text{BE}||\text{BD}|} = \cos\left(\gamma_w - \Lambda_{BE} - \Omega_B + \frac{\pi}{2}\right), \quad (\text{D.5})$$

$$|\text{BE}|^2 + |\text{BD}|^2 - d^2 = 2|\text{BE}||\text{BD}| \cos\left(\gamma_w - \Lambda_{BE} - \Omega_B + \frac{\pi}{2}\right), \quad (\text{D.6})$$

$$d = \sqrt{|\text{BE}|^2 + 2|\text{BE}||\text{BD}| \sin(\gamma_w - \Lambda_{BE} - \Omega_B) + |\text{BD}|^2}, \quad (\text{D.7})$$

where due to the nature of the model, the d can be only positive. The θ_m , φ and L_s are formulated in the same manner as in the ride side.

D.3 Unknown θ angle

The Figure [D.2] shows the diagram of the McPherson suspension model where the θ is derived for the left side. The $|BD|$ and $|AE|$ is found by (3.30) and (3.42) respectively and the $\kappa = \pi - \sigma_{shf}$ because the McPherson strut is constructed to have 90 degrees angle to the mounted surface at the nominal camber. The κ is constant because the rail is assumed not curved. However, if the rail would be curved, the κ would be function of the stroke length d . Thus, the point D can be found with:

$$D = \begin{bmatrix} d \cos(\kappa + \varphi) \\ d \sin(\kappa + \varphi) \end{bmatrix} + \begin{bmatrix} E_y \\ E_z \end{bmatrix}, \quad (D.8)$$

where the φ has to be included to account for the body roll. The θ is thus defined with:

$$\Lambda_{AE} = \arctan 2(E_z - A_z, E_y - A_y), \quad (D.9)$$

$$\theta = \Gamma_A + \Lambda_{AE}, \quad (D.10)$$

where Γ_A is defined in (3.46).

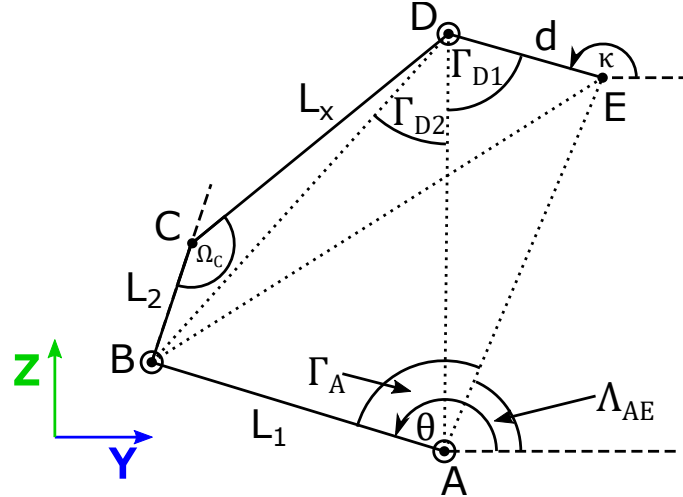


Figure D.2: The derivation of the θ angle for the left side geometry model of the McPherson suspension.

Appendix E

Derivation of the KPI and caster influence on camber angle

The [11] presents a homogeneous transformation that can be used to predict the camber angle from the KPI and caster angle when the wheel is steered. This chapter will produce the same derivation with the framework developed in this thesis.

Three Z-up coordinate systems are defined: C wheel-body coordinate frame, the W wheel coordinate frame and the T tire coordinate frame. The C frame is attached to the vehicle body and rests on the vertical plane to the ground. It is unaffected by the wheel motion. The W is defined as the center wheel as shown in Figure [E.1] and is subjected to all of the rotation and translations of the wheel. When the wheel is not steered, the C and W are equivalent. The T is defined as the center of the contact patch. It only follows the steering rotation of the wheel. All frame are independent of the wheel spin rotation. The rotational matrix expressing the axis-angle rotation from W to C frame is called Rodriguez matrix:

$${}^C R_W = \begin{bmatrix} u_1^2 (1 - \cos(\delta)) + \cos(\delta) & u_1 u_2 (1 - \cos(\delta)) - u_3 \sin(\delta) & u_1 u_3 (1 - \cos(\delta)) + u_2 \sin(\delta) \\ u_1 u_2 (1 - \cos(\delta)) + u_3 \sin(\delta) & u_2^2 (1 - \cos(\delta)) + \cos(\delta) & u_2 u_3 (1 - \cos(\delta)) - u_1 \sin(\delta) \\ u_1 u_3 (1 - \cos(\delta)) - u_2 \sin(\delta) & u_2 u_3 (1 - \cos(\delta)) + u_1 \sin(\delta) & u_3^2 (1 - \cos(\delta)) + \cos(\delta) \end{bmatrix}, \quad (\text{E.1})$$

where

$$u = \begin{bmatrix} u_1 \\ u_2 \\ u_3 \end{bmatrix}, \quad (\text{E.2})$$

is the direction unit vector and it relates to the steering axis SA.

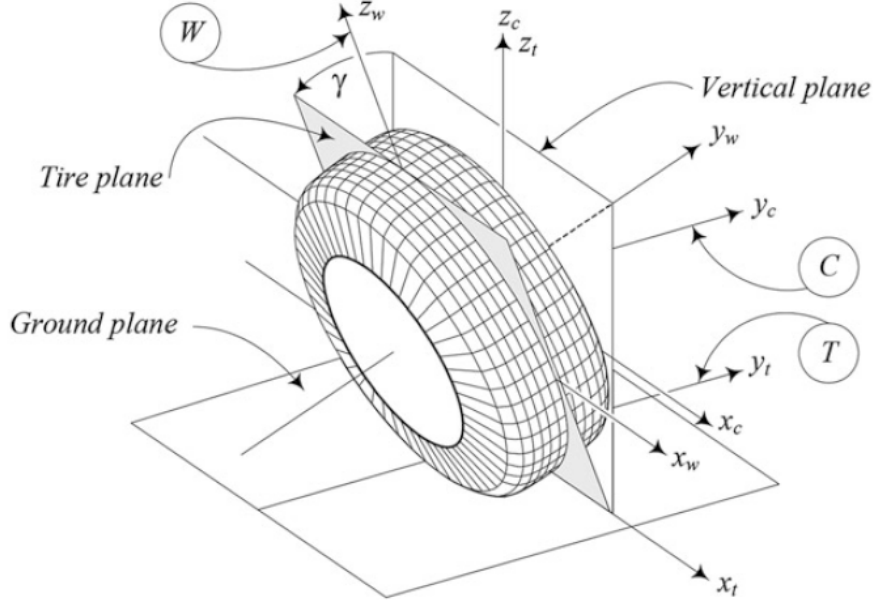


Figure E.1: The definition of the coordinate systems of the wheel: C wheel-body coordinate frame, the W wheel coordinate frame and the T tire coordinate frame. Picture from: [11]

The steering axis can be thought as an intersection of two planes: the caster angle and KPI plane. The caster plane is rotated by KPI angle from the wheel-body YZ -plane (C frame) and the KPI plane by caster angle ϕ from the wheel-body XZ -plane. The normal unit vectors of these planes in the C frame can be defined as:

$$n_I = \begin{bmatrix} \cos(\phi) & 0 & \sin(\phi) \\ 0 & 1 & 0 \\ -\sin(\phi) & 0 & \cos(\phi) \end{bmatrix} \cdot \begin{bmatrix} -1 \\ 0 \\ 0 \end{bmatrix} = \begin{bmatrix} -\cos(\phi) \\ 0 \\ \sin(\phi) \end{bmatrix}, \quad (\text{E.3})$$

$$n_c = \begin{bmatrix} 1 & 0 & 0 \\ 0 & \cos(\text{KPI}) & -\sin(\text{KPI}) \\ 0 & \sin(\text{KPI}) & \cos(\text{KPI}) \end{bmatrix} \cdot \begin{bmatrix} 0 \\ 1 \\ 0 \end{bmatrix} = \begin{bmatrix} 0 \\ \cos(\text{KPI}) \\ \sin(\text{KPI}) \end{bmatrix}, \quad (\text{E.4})$$

which specify the unit vector of the steering axis as:

$$C_u = \frac{n_c \times n_I}{|n_c \times n_I|} = \frac{1}{\sqrt{1 - \sin(\phi)^2 \sin(\text{KPI})^2}} \begin{bmatrix} \sin(\phi) \cos(\text{KPI}) \\ -\sin(\text{KPI}) \cos(\phi) \\ \cos(\phi) \cos(\text{KPI}) \end{bmatrix}. \quad (\text{E.5})$$

The axis has to be defined by a point. The d_P is the point on the steering

axis

$$d_P = \begin{bmatrix} s_a \\ s_b \\ -R_o \end{bmatrix}, \quad (\text{E.6})$$

chosen as the intersection of the steering axis and the ground where R_o is the wheel radius and s_a and s_b the longitudinal and lateral displacement of the center of the contact patch to the intersection point. To also define the translation, the homogeneous transformation matrix ${}^C T_W$ is used which combines both the rotation and the translation. However, the rotation is not around the frame center but around the point d_P . Thus, the transformation between the C and W frames is:

$${}^C r = {}^C T_W {}^W r = \begin{bmatrix} {}^C R_W & d_P - {}^C R_W d_P \\ 0 & 1 \end{bmatrix} {}^W r, \quad (\text{E.7})$$

where the ${}^C r$ and ${}^W r$ are homogeneous position vectors in the particular frame.

If the angle between the Z axis of the C frame and the Y axis of the W frame is called ρ , the camber angle is defined as:

$$\gamma = \frac{\pi}{2} - \rho. \quad (\text{E.8})$$

Denote the unit vector for Z axis of the C as \hat{K} and the unit vector for the Y axis of the W as \hat{j} . Then, the angle ρ is characterized by the dot-product formula for two vectors as:

$$\rho = \arccos \left(\frac{{}^C \hat{j} \cdot {}^C \hat{K}}{|{}^C \hat{j}| |{}^C \hat{K}|} \right), \quad (\text{E.9})$$

where

$${}^C \hat{K} = \begin{bmatrix} 0 \\ 0 \\ 1 \\ 0 \end{bmatrix}, \quad (\text{E.10})$$

$${}^C \hat{j} = {}^C T_W {}^W \hat{j} = \begin{bmatrix} {}^C R_W & d_P - {}^C R_W d_P \\ 0 & 1 \end{bmatrix} \begin{bmatrix} 0 \\ 1 \\ 0 \\ 0 \end{bmatrix}. \quad (\text{E.11})$$

By substituting for ρ in (E.8), the following is derived:

$$\gamma = \frac{\pi}{2} - \arccos \left[\frac{\cos(\text{KPI}) \sin(\phi)}{\sqrt{1 - \sin(\phi)^2} \sin(\text{KPI})^2} \sin(\delta) - \frac{\cos(\text{KPI}) \cos(\phi)^2 \sin(\text{KPI})}{\sin(\text{KPI})^2 \sin(\text{KPI})^2 - 1} (\cos(\delta) - 1) \right], \quad (\text{E.12})$$

which is the same solution as derived in [11]. Note that the solution is independent of the displacements from the point P and the $\gamma = \frac{\pi}{2}$ when $\delta = 0$. Moreover, the influence of the ϕ and KPI is additive to the value of γ . Thus, it can be easily incorporated to the existing estimation in (3.26). The notation used for the derivation of this formula is different than the one used in this thesis. This thesis defines the caster angle as positive when the [11] as negative. Additionally, the [11] defines $\text{KPI} < 0$ for the left wheel and $\text{KPI} > 0$ for the right wheel and the $\delta < 0$ for the right turns and $\delta > 0$ for the left turns. This thesis defines the $\text{KPI} > 0$ always positive and the right turns as $\delta > 0$ and the left $\delta < 0$, see the Z-down coordinate frame defined in the **Twin track**.

Appendix F

Velocity dependent LQR

The vehicle dynamics are too dependent on the car speed as discussed in **Robustness testing**. The state-feedback gains K_r , K_β and $K_{\epsilon\dot{v}}$ can be scaled with the vehicle velocity by the nonlinear function that can be stored in the memory, see Figures [F.1] and [F.2]. The gains can be found with interpolation methods between the points.

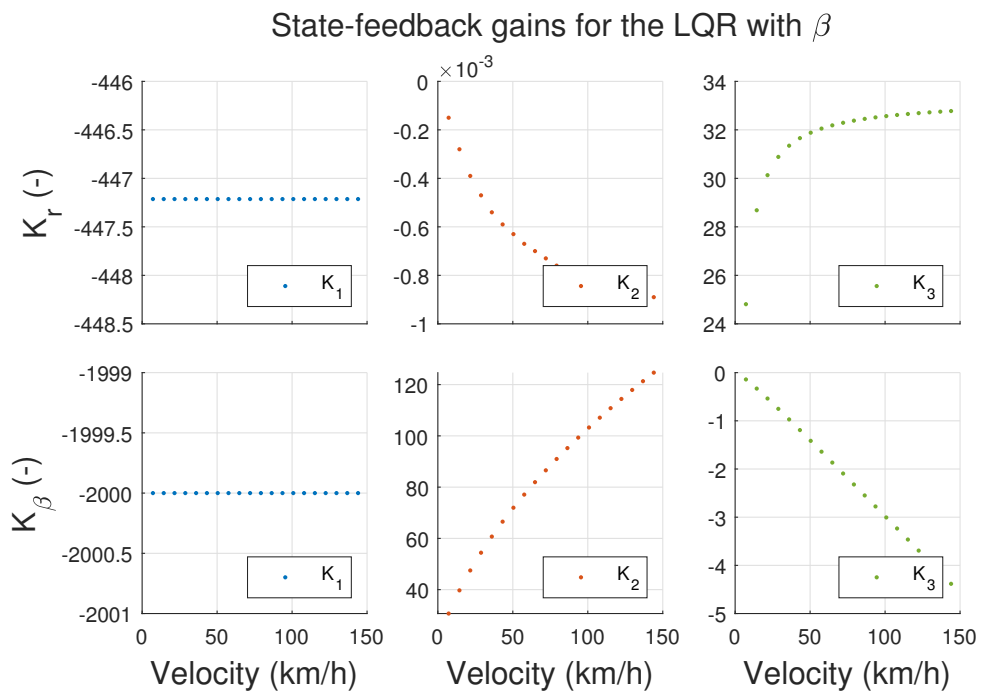


Figure F.1: The state-feedback gains dependence on the velocity for the LQR with β .

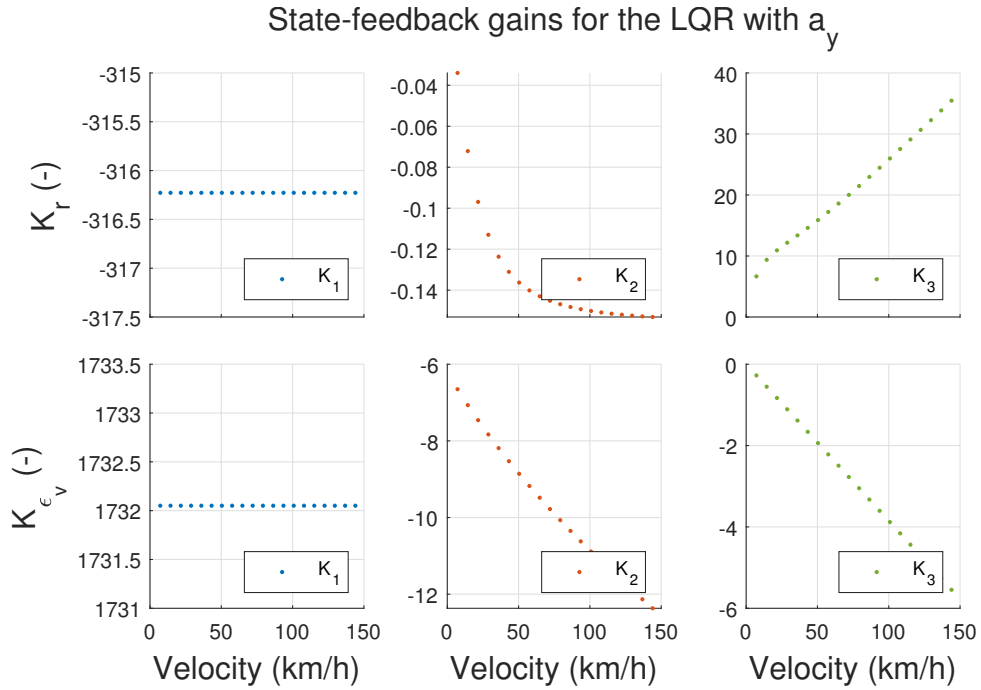


Figure F.2: The state-feedback gains dependence on the velocity for the LQR with a_y .

Note that storing process can be optimized depending on the application. For example, the nonlinear functions can be approximated with piece-wise polynomials that will reduce the amount of parameters stored etc.

Appendix G

Double wishbone suspension

G.1 Simscape model

The same approach for the McPherson can be used for the double wishbone suspension as well. This chapter will provide basis for the double wishbone suspension that can be used to develop similar control law as for McPherson. First, the geometry model is defined first in **Double wishbone geometry model** and then solved for the camber angle of the actuator in **Forward kinematics**. Lastly, the control law is presented in **Control law: nonlinear mapping**.

G.1.1 Double wishbone geometry model

The double wishbone suspension as defined in **Double wishbone** is composed from two links, the spring-damper and the king-pin, as shown in Figure [G.1]. The suspension can be modeled with 5 points (A, B, C, D, D_2).

The point A is at the revolute joint of the lower control arm mounting point. It is assumed that its position is constant and does not change. Next is the point B which is at the ball joint between the lower arm and the king-pin. The angle θ is defined as the angle of the lower control arm to the ground. The lower arm length is L_1 and the king-pin with the ball joint is L_2 where both are constants. The point P is the revolute joint that connects the spring-damper and the lower arm. The $|AP|$ length is known. The king-pin is assumed to be vertically aligned with the wheel as any misalignment is constant and can be subtracted out and compensated. Thus, the camber angle of the wheel is the same as the angle of the king-pin from the perpendicular plane to the ground, see right Figure [G.1]. The point C is the highest point of the king-pin and it is angled from B by camber γ as shown. The L_s is

the spring-damper length and the point D_2 is the revolute joint that mounts the spring-damper to the sprung mass. The point D is at the revolute joint of the double wishbone mounting point of the upper link. The point D and D_2 is assumed constant but it rotates around the point A by roll angle φ . The d defines the length of the upper link and it is directly controlled by the actuator.

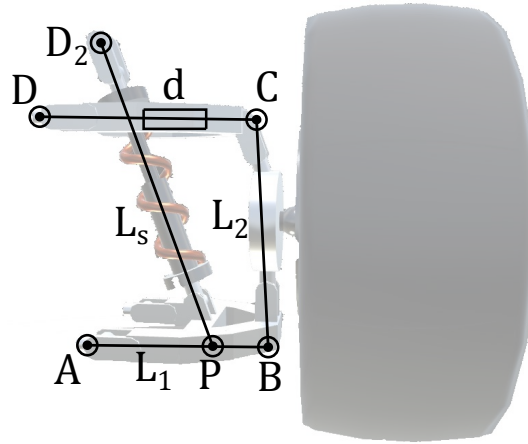


Figure G.1: Double wishbone suspension modeled as 5 points (background picture from: [12])

■ G.1.2 Forward kinematics

The geometric model in Figure [3.10] defines the camber angle γ purely from the suspension structure. To ease the calculation effort, notice that the triangle $\triangle ADD_2$ is constant because the lengths of the sides do not change and thus the Γ_2 angle is also constant. That is why, the point D and D_2 can be merged and the new spring-damper L_x and Γ_A angle is defined, see right Figure [G.2]:

$$\Gamma_A = \arccos \left(\frac{|AP|^2 + |AD_2|^2 - L_s^2}{2|AP||AD_2|} \right) + \Gamma_2. \quad (\text{G.1})$$

To calculate camber for particular suspension parameters, the forward kinematics must be solved. The forward kinematics diagram is depicted in right Figure [G.2]. The points A and D are known where A is assumed as the center of the coordinate system. Thus, the point D has to be rotated by roll

angle φ around the point A :

$$A = \begin{bmatrix} A_y \\ A_z \end{bmatrix} = \begin{bmatrix} 0 \\ 0 \end{bmatrix}, \quad (\text{G.2})$$

$$D = \begin{bmatrix} \cos(\varphi) & -\sin(\varphi) \\ \sin(\varphi) & \cos(\varphi) \end{bmatrix} \cdot \begin{bmatrix} D_y \\ D_z \end{bmatrix}, \quad (\text{G.3})$$

and the angle θ and the point B can be found from triangle $\triangle APD$:

$$\theta = \Lambda_{AD} - \Gamma_A, \quad (\text{G.4})$$

$$B = \begin{bmatrix} L_1 \cos(\theta) \\ L_1 \sin(\theta) \end{bmatrix}. \quad (\text{G.5})$$

Finally, the forward kinematics for the camber angle γ from Figure [G.3] can be calculated as:

$$\gamma = -\Lambda_{BD} + \Gamma_B + \frac{\pi}{2}, \quad (\text{G.6})$$

where

$$\Lambda_{BD} = \arctan 2(D_z - B_z, D_y - B_y), \quad (\text{G.7})$$

$$\Gamma_B = \arccos \left(\frac{L_2^2 + |\text{BD}|^2 - d^2}{2 L_2 |\text{BD}|} \right), \quad (\text{G.8})$$

$$|\text{BD}| = \sqrt{(D_y - B_y)^2 + (D_z - B_z)^2}. \quad (\text{G.9})$$

Note that the double wishbone geometry model can define θ independent of the upper link arm length d .

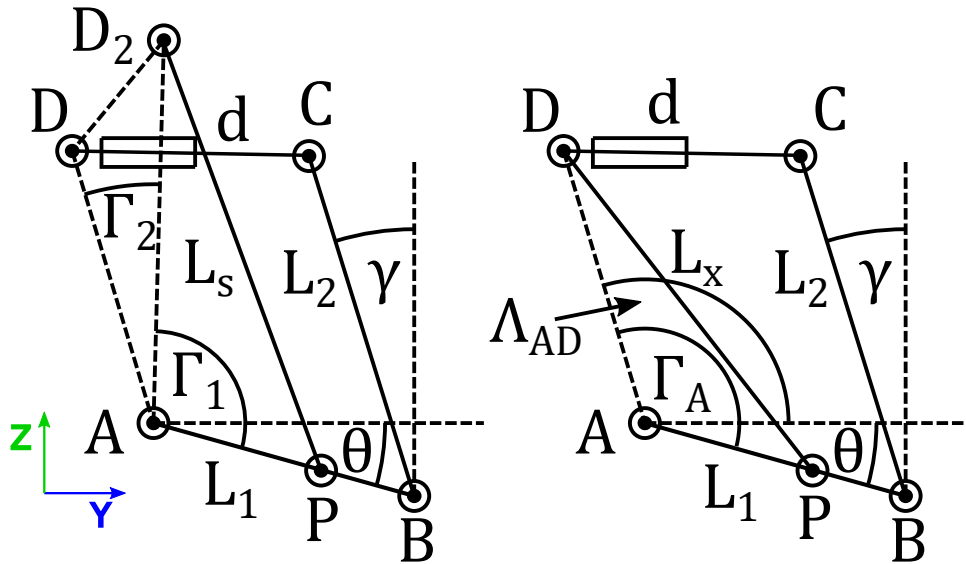


Figure G.2: Forward kinematics for θ angle of model in Figure [G.1].

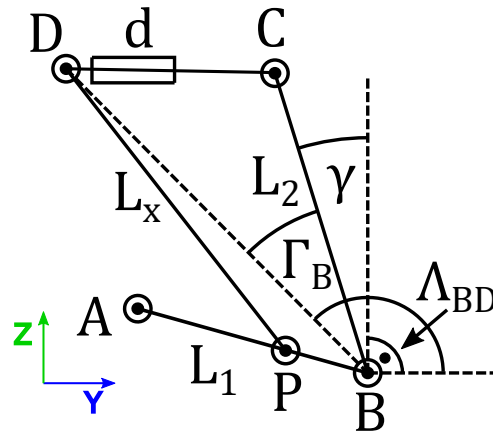


Figure G.3: Forward kinematics for camber angle γ angle of model in Figure [G.1].

■ G.1.3 Control law: nonlinear mapping

The control law defines input to the actuator so that the reference is met. The actuator is defined as a prismatic joint that controls the length of the upper arm of the double wishbone suspension. The input to the actuator is d and the reference is the camber angle γ_w we want to have.

The equation (G.6) can be used to derive such a law. The γ can be denoted as γ_w and the d is the unknown:

$$\gamma_w = -\Lambda_{BD} + \Gamma_B(d) + \frac{\pi}{2}, \quad (\text{G.10})$$

and by solving for d the following expression is found:

$$\Gamma_B(d) = \Lambda_{BD} + \gamma_w - \frac{\pi}{2}, \quad (\text{G.11})$$

$$\frac{L_2^2 + |\text{BD}|^2 - d^2}{2 L_2 |\text{BD}|} = \cos \left(\Lambda_{BD} + \gamma_w - \frac{\pi}{2} \right), \quad (\text{G.12})$$

$$L_2^2 + |\text{BD}|^2 - d^2 = 2 L_2 |\text{BD}| \cos \left(\Lambda_{BD} + \gamma_w - \frac{\pi}{2} \right), \quad (\text{G.13})$$

$$d = \sqrt{|\text{BE}|^2 + 2 |\text{BE}| |\text{BD}| \sin (-\Lambda_{BD} - \gamma_w) + |\text{BD}|^2}, \quad (\text{G.14})$$

where due to the nature of the model, the d can be only positive. The solution is actually algebraic and gives precise d distance for reaching the given camber angle γ_w . The equation does not need the θ measurement can define camber angle purely from spring-damper length L_s and body roll φ .



Appendix H

Bibliography

- [1] H. Habibi and K. Heidari Shirazi, “Application of virtual reality in improvement and optimization of bump steering response of Mcpherson suspension mechanism,” *International Review of Mechanical Engineering*, vol. 2, pp. 149–158, 2008.
- [2] S. Li, “Camber effect study on combined tire forces,” Master’s thesis, KTH, Vehicle Dynamics, 2013.
- [3] D. Roethof, T. Sezer, M. Arat, and B. Shyrokau, “Influence of Active Camber Control on Steering Feel,” *SAE International Journal of Passenger Cars - Mechanical Systems*, vol. 9, pp. 124–134, 2016.
- [4] MATLAB, *version 9.10.0.1739362 (R2021a) Update 5*. Natick, Massachusetts: The MathWorks Inc., 2021.
- [5] Honed Developments, “Camber gain.” [Online]. Available: <https://www.facebook.com/honeddevelopments/photos/pcb.2419827751677012/2419827621677025/>
- [6] S. M. Laws, “AN ACTIVE CAMBER CONCEPT FOR EXTREME MANEUVERABILITY: MECHATRONIC SUSPENSION DESIGN, TIRE MODELING, AND PROTOTYPE DEVELOPMENT,” 2010. [Online]. Available: <http://purl.stanford.edu/hg888rd4402>
- [7] D. Ye, J. Tan, Y. Liang, and Q. Feng, “Experimental Study on Influence of Temperature to Control Performance for Viscoelastic Materials Pounding Tuned Mass Damper,” *Frontiers in Materials*, vol. 8, p. 197, 2021. [Online]. Available: <https://www.frontiersin.org/article/10.3389/fmats.2021.676405>

- [8] S. Cotton and P. R. Slater, “Electric vehicle batteries: what will they look like in the future?” aug 2021. [Online]. Available: <https://theconversation.com/electric-vehicle-batteries-what-will-they-look-like-in-the-future-164263>
- [9] “Actuators - Xemo,” 2018. [Online]. Available: <http://www.xemo.io/edu/robot/actuators/>
- [10] H. B. Pacejka, “Chapter 1 - Tire Characteristics and Vehicle Handling and Stability,” in *Tire and Vehicle Dynamics (Third Edition)*, third edit ed., H. B. Pacejka, Ed. Oxford: Butterworth-Heinemann, 2012, pp. 1–58. [Online]. Available: <https://www.sciencedirect.com/science/article/pii/B9780080970165000012>
- [11] D. Vo, H. Marzbani, M. Fard, and R. Jazar, *Caster–Camber Relationship in Vehicles*, 2016, pp. 63–89.
- [12] “SimplePlanes | Double wishbone suspension.” [Online]. Available: <https://www.simpleplanes.com/a/Hc43Ea/Double-wishbone-suspension>
- [13] “50+ Car Accident Statistics (Sept. 2021) Auto Accident Deaths,” sep 2021. [Online]. Available: <https://www.thewanderingrv.com/car-accident-statistics/>
- [14] A. S. Avantage VAG, “Facebook,” feb 2020. [Online]. Available: https://www.facebook.com/AVANTAGE.VAG/photos/a.572240592842099/2885630208169781/?type=3&eid=ARAAC6ZBDE8xnryCrCNBjEErKIP{__}vzIx4nWvrR-zIWF5ybKL95fFrW4n3aP0fTqKDtE1ItpNmxVHny{__}A
- [15] H. der Auweraer, T. Tamarozzi, E. Risaliti, M. Sarrazin, J. Croes, B. Forrier, F. Naets, and W. Desmet, “VIRTUAL SENSING BASED ON DESIGN ENGINEERING SIMULATION MODELS,” 2017.
- [16] C. Kavitha, S. A. Shankar, B. Ashok, S. D. Ashok, H. Ahmed, and M. U. Kaisan, “Adaptive suspension strategy for a double wishbone suspension through camber and toe optimization,” *Engineering Science and Technology, an International Journal*, vol. 21, no. 1, pp. 149–158, feb 2018.
- [17] W. Zhang, L. Drugge, M. Nybacka, and Z. Wang, “Active camber for enhancing path following and yaw stability of over-actuated autonomous electric vehicles,” *Vehicle System Dynamics*, vol. 59, pp. 1–22, 2020.

- [18] J. Jerrelind, P. Allen, P. Gruber, M. Berg, and L. Drugge, “Contributions of vehicle dynamics to the energy efficient operation of road and rail vehicles,” *Vehicle System Dynamics*, vol. 59, no. 7, pp. 1114–1147, 2021. [Online]. Available: <https://doi.org/10.1080/00423114.2021.1913194>
- [19] P. Sun, A. Stensson Trigell, L. Drugge, J. Jerrelind, and M. Jonasson, “Exploring the Potential of Camber Control to Improve Vehicles’ Energy Efficiency during Cornering,” *Energies*, vol. 11, no. 4, 2018. [Online]. Available: <https://www.mdpi.com/1996-1073/11/4/724>
- [20] J. Belák, “Advanced steering concept for overactuated vehicle,” Bachelor, CTU, 2020. [Online]. Available: <https://dspace.cvut.cz/handle/10467/87767>
- [21] H. B. Pacejka, “Chapter 4 - Semi-Empirical Tire Models,” in *Tire and Vehicle Dynamics (Third Edition)*, third edit ed., H. B. Pacejka, Ed. Oxford: Butterworth-Heinemann, 2012, pp. 149–209. [Online]. Available: <https://www.sciencedirect.com/science/article/pii/B9780080970165000048>
- [22] J. Minarik, “Yaw Stabilization of 4 Wheel Steering Cars,” Bachelor, CTU, 2019. [Online]. Available: <https://dspace.cvut.cz/handle/10467/83045>
- [23] B.-C. Chen and F.-C. Hsieh, “Sideslip angle estimation using extended Kalman filter,” *Vehicle System Dynamics - VEH SYST DYN*, vol. 46, pp. 353–364, 2008.
- [24] H. F. Grip, L. Imsland, T. A. Johansen, J. C. Kalkkuhl, and A. Suissa, “IEEE CONTROL SYSTEMS MAGAZINE 1 Vehicle Sideslip Estimation Design, implementation, and experimental validation.”
- [25] B. Oliveira, “Vehile Dynamics - theory and calculation.pdf.”
- [26] P. Raksincharoensak, S. Daisuke, and M. Lidberg, “Direct Yaw Moment Control for Enhancing Handling Quality of Lightweight Electric Vehicles with Large Load-To-Curb Weight Ratio,” *Applied Sciences*, vol. 9, p. 1151, 2019.
- [27] A. Suresh Athrey, “Design and Analysis of an Electric Over-Actuated Vehicle Suspension,” Ph.D. dissertation, KTH, 2020. [Online]. Available: <http://kth.diva-portal.org/smash/record.jsf?pid=diva2{%}3A1469342{%}&dswid=-9379>

- [28] M. Doumiati, A. Victorino, A. Charara, and D. Lechner, “Lateral load transfer and normal forces estimation for vehicle safety: experimental test,” *Vehicle System Dynamics*, vol. 47, no. 12, pp. 1511–1533, 2009. [Online]. Available: <https://doi.org/10.1080/00423110802673091>
- [29] R. Rajamani, *Electronic Stability Control*. Boston, MA: Springer US, 2012, pp. 201–240. [Online]. Available: <https://doi.org/10.1007/978-1-4614-1433-9{ }8>
- [30] K. Spentzas, I. Alkhalil, and M. Deric, “Kinematics of four-wheel-steering vehicles,” *Forschung im Ingenieurwesen*, vol. 66, pp. 211–216, 2001.
- [31] S. Skogestad and I. Postlethwaite, *Multivariable Feedback Control: Analysis and Design*, 2005, vol. 2.